

Synthesis of Superhydrophobic Nanocomposite Coatings Using Electrodeposition

by

Daniel John Iacovetta

A thesis submitted in conformity with the requirements
for the degree of Master's of Applied Science
Department of Materials Science and Engineering
University of Toronto

© Copyright by Daniel John Iacovetta 2014

Synthesis of Superhydrophobic Nanocomposite Coatings Using Electrodeposition

Daniel John Iacovetta

Master's of Applied Science

Department of Materials Science and Engineering
University of Toronto

2014

Abstract

The focus of the current research is to produce a metal matrix composite material that possesses a superhydrophobic surface using electrodeposition. The objective is to create a multifunctional coating that is able to provide high strength as well as high water repellency using nanocrystalline nickel and polytetrafluoroethylene (PTFE) particles. The co-deposition process was first studied. It was determined that the amount of PTFE co-deposited is highly dependent on the concentration of PTFE particles in the electroplating bath. The wetting angle of the surface greatly increased when the PTFE content increases. Next the electroplating procedure of pure nickel is altered to produce a nanocrystalline material, resulting in a large increase in the hardness of the nickel coatings. The two techniques are combined to produce a nanocrystalline Nickel-PTFE composite. Under optimum conditions, the composite coating displayed a highly water repellent surface and improved mechanical properties.

Acknowledgments

I would like to greatly thank Professor Uwe Erb for providing a great deal of guidance and support throughout my research. Under his supervision I was able to gain a vast amount of knowledge and experience that will benefit me the rest of my life. I would like to thank all of the members of the Nanomaterials Research Group for all of the generous help provided and the many insightful discussions. I would also like to give thanks to my committee members Dr. Chandra Veer Singh and Dr. Benjamin D. Hatton.

Thank you to the National Science and Engineering Research Council (NSERC) for providing the funding to make this research possible.

Thank you to Sal Boccia for training and assistance of the operation of the electron microscopes. I would also like to acknowledge the very helpful administrative and technical support staff in the department of Materials Science and Engineering for their assistance throughout the years.

Finally I want to give thanks to my always loving and supporting parents Bruno and Fran Iacovetta and my wonderful sisters Sonya and Lauren. I also am greatly appreciative of the constant support from my amazing girlfriend Jordy Feldberg, and all of my friends.

Table of Contents

Abstract	ii
Acknowledgments	iii
Table of Contents	iv
List of Tables	vii
List of Figures	viii
List of Acronyms	xii
List of Variables	xiii
Chapter 1 Introduction	1
1.1 Development of Artificial Superhydrophobic Surfaces.....	2
1.2 Objectives and Structure of Thesis	10
Chapter 2 Background Information	13
2.1 Superhydrophobic Surfaces	13
2.1.1 Wetting of Smooth Surfaces	13
2.1.2 Wetting of Non-Ideal Surfaces	14
2.2 Synthesis of Composite Coatings using Electrodeposition	20
2.2.1 Mechanism for Co-deposition.....	20
2.2.2 Effect of Surfactant on Co-deposition Process	24
2.2.3 Effect of Particles on Coating Properties.....	29
2.3 Nanocrystalline Metals	35
2.3.1 Synthesis of Nanocrystalline Nickel using Electrodeposition	37
2.3.2 Grain Size Effect on Hardness and Yield Strength.....	41

Chapter 3 Experimental Procedures	44
3.1 Particle Characterization.....	44
3.1.1 Scanning Electron Microscopy.....	46
3.1.2 Ultrasound-Based Methods.....	46
3.2 Synthesis of Composite.....	49
3.3 Electrodeposit Characterization.....	51
3.3.1 SEM and Image Analysis.....	51
3.3.2 Energy Dispersive X-Ray Spectroscopy.....	52
3.3.3 Contact Angle Measurements.....	53
3.3.4 X-Ray Diffraction.....	54
3.3.5 Vicker’s Microhardness.....	56
3.3.6 Surface Profilometry.....	57
Chapter 4 Co-Deposition of Ni-PTFE Composite	58
4.1 Particle Characterization.....	59
4.1.1 Particle Size.....	59
4.1.2 Zeta Potential.....	63
4.2 Effect of Particle Concentration on Co-deposition.....	66
4.3 Effect of PTFE on Wetting Properties.....	71
Chapter 5 Grain Refinement of Nickel Coatings	76
5.1 SEM Images.....	76
5.2 XRD Results.....	78
5.2.1 Grain Size.....	78
5.2.2 Texture.....	80
5.3 Hardness Testing.....	82
5.4 Wetting Properties.....	83

Chapter 6 Nanocrystalline Nickel – PTFE Composite	86
6.1 XRD Patterns	86
6.1.1 Grain Size.....	87
6.1.2 Texture	88
6.2 Hardness.....	89
6.3 Wetting Properties	94
6.4 Surface Profilometry.....	95
Chapter 7 Conclusions.....	101
Chapter 8 Future Work.....	104
References	106
Appendix 1 – Determining Coating Composition	114
Appendix 2 – Additional SEM Images.....	117
Appendix 3 – Additional Information on Acoustic Particle Size Measurements	123
Appendix 4 – Additional Information on Zeta Potential Measurements	127
Appendix 5 – Sample Calculations for Intensity of XRD Peaks for Nickel with Random Orientation.....	129
Appendix 6 – Further Surface Roughness Images.....	131

List of Tables

Table 2.1: Dependence of grain size on various properties [Erb 2010].....	37
Table 3.1: Typical properties for Fluon 1710 PTFE micropowder	45
Table 3.2: Electroplating bath composition and parameters.....	51
Table 4.1: Zeta potential at different ion concentrations	63
Table 4.2: PTFE content in deposit with varying PTFE concentration in plating bath	70
Table 4.3: Wetting properties of Ni-PTFE coatings	73
Table 5.1: Grain size with saccharin addition.....	78
Table 5.2: Calculated intensity of diffraction peaks for random nickel	81
Table 5.3: Orientation Index with varying saccharin concentration.....	81
Table 5.4: Microhardness values for samples produced with varying saccharin concentration...	82
Table 5.5: Contact angle of water on nickel samples with the addition of saccharin.....	83
Table 6.1: Grain size measured using the Scherrer formula for Ni-PTFE samples with varying saccharin concentration.....	88
Table 6.2: Orientation Index for Ni-PTFE samples with varying saccharin concentration.....	89
Table 6.3: Hardness values for Ni-PTFE composite coatings with varying saccharin content	90
Table 6.4: Comparison between measured hardness values for Ni-PTFE composite and predicted hardness using Equation (6-1)	92
Table 6.5: Summary of PTFE content and contact angle for samples containing 0-5 g/L of saccharin.	95
Table A4.1: Dielectric permittivity values used to calculate zeta potential	128
Table A5.1: Summary of values used to calculate I in Equation (A5-3).....	130

List of Figures

Figure 1.1: SEM images of leaf surfaces with hierarchial roughness that display superhydrophobic behaviour [Bhushan and Jung 2006].....	3
Figure 1.2: Typical methods to fabricate micro/nanoroughened surfaces. [Bhushan and Jung 2011]	4
Figure 1.3: Patterned SU-8 surfaces, circular pillars of various heights and diameters in square patterns [Shirtcliffe et al. 2004]	5
Figure 1.4: SEM images of dual-size-rough surface. (a) 1 μm silica spheres electrostatic-deposited on 8 μm silica sphere template. (b) 100 nm silica spheres electrostatic adsorbed on 8 μm silica sphere template. (c) micron sphere array assembled by 300 nm silica spheres. (d) an enlarged view of (c). Scale bars are 5 μm in a, b and d, and 50 μm in c. [Sun et al. 2007]	6
Figure 1.5: Contact angles on silicon surfaces with different surface texturing after PFOS treatment. For a silicon pyramid surface that possesses a hierarchical structure, a superhydrophobic surface with minimum hysteresis results after PFOS treatment. Nanostructures have been formed by Au-assisted etching of silicon surfaces in HF/H ₂ O ₂ for 60 s with a Au layer of 5 nm on the silicon (111) surface. [Xiu et al. 2007].....	7
Figure 1.6: Outline of the structure of the thesis	12
Figure 2.1: Water droplet on a flat solid surface, showing the static contact angle θ_0 , and the surface tensions at each interface γ_{SL} (solid-liquid), γ_{LV} (liquid-vapour), and γ_{SV} (solid-vapour). 14	14
Figure 2.2: Wetting on solid surfaces: (a) complete non-wetting, (b) superhydrophobic (c) hydrophobic, (d) hydrophilic (e) and complete wetting [Victor 2012]	15
Figure 2.3: The amplification effect of roughness factor R_f in the Wenzel equation [Jung and Bhushan 2006].	17
Figure 2.4: Visual representation of the different wetting states	18
Figure 2.5: Gugliemli’s proposed two step process for particle incorporation [Guglemlı 1972]. 21	21
Figure 2.6: Electric double layer around charged particle in solution. The zeta potential is defined at the outer boundary of the diffuse layer (slipping plane) [Duhkin and Goetz 2010]....	27
Figure 2.7: Amount of co-deposited PTFE with different surfactants. CTAB is a cationic surfactant, PVP is non-ionic and SDS is anionic surfactant [Mafi and and Dehghanian 2011]... 28	28
Figure 2.8: Effect of cationic surfactant concentration in co-deposition of SiC particles [Kilic et al. 2013]	29

Figure 2.9: SEM images of copper-microcapsule composite showing surface and cross-section [Xu et al. 2011].	33
Figure 2.10: SEM image of Ni-PTFE coating containing 47.4 vol% PTFE displaying superhydrophobicity [Wang et al. 2004].	35
Figure 2.11: Volume fraction of intercrystalline regions as a function of grain size [Palumbo et al. 1990]	36
Figure 2.12: Effect of saccharin addition to electroplating bath on the grain size of nickel [El-Sherik and Erb 1995].	40
Figure 2.13: Hall-Petch plot for Vickers hardness of electrodeposited nanocrystalline nickel [El-Sherik et al. 1992]	42
Figure 3.1: Structural formula for PTFE [Callister 2008]	45
Figure 3.2: DT-1200 close up image of sample chamber.	47
Figure 3.3: Structural formula for CTAB	49
Figure 3.4: Schematic diagram showing the electrodeposition setup used.	51
Figure 3.5: Example of contact angle measurement using ImageJ.	54
Figure 4.1: PTFE particles at A) x1,500 B) x10,000, large single particle C) x20,000, agglomeration of submicron particles D) x50,000 submicron particles	60
Figure 4.2: Particle size distributions for A) submicron particles (as seen in Figure 4.1 D) and B) micrometer scale particles and agglomerates (as seen in Figure 4.1 A and B)	60
Figure 4.3: Particle size distribution of PTFE particles in solution of DI water and surfactant CTAB. Three results of the same solution are provided to demonstrate repeatability. A) Cumulative PSD on a volume basis B) density PSD	61
Figure 4.4: SEM images of composite coating containing 69 vol% PTFE using backscattered electrons. A) x500 magnification showing uneven distribution of micron scale particles B) x2,500 magnification showing submicron particles evenly distributed between larger particles C) x5,000 magnification	67
Figure 4.5: Cross section images of Ni-PTFE coating containing 61 vol% PTFE, dark areas show areas where PTFE particles have been embedded in coating. A) x2,500 magnification, the white line in highlights the interface between coating and copper substrate B) x10,000 magnification	68
Figure 4.6: High magnification image of nickel matrix with embedded PTFE particles exposed on the surface	68

Figure 4.7: PTFE incorporation in coatings versus PTFE concentration in the plating bath. Results of both image analysis and EDX are provided.....	70
Figure 4.8: Contact angles for composite coatings with different PTFE content. A) 0vol% PTFE B) 41 vol% PTFE C) 45 vol% PTFE D) 58 vol% PTFE E) 69 vol% PTFE	72
Figure 4.9: Contact angle with varying amount of PTFE. PTFE incorporation determined through EDX.....	73
Figure 4.10: Profilometry line scans illustrating added roughness to the surface during co-deposition with PTFE particles.....	74
Figure 5.1: SEM images of pure nickel coatings x5,000 magnification A) no additives B) 0.1 g/L CTAB C) 0.1 g/L CTAB + 0.1 g/L saccharin.....	77
Figure 5.2: X-ray diffraction patterns for pure nickel coatings plated using different saccharin concentrations. All samples also contain 0.1 g/L CTAB.....	79
Figure 5.3: Contact angle as a function of saccharin concentration in the bath	84
Figure 6.1: X-ray diffraction patterns of Ni-PTFE coatings plated using different saccharin concentrations	87
Figure 6.2: Comparison between measured hardness values for Ni-PTFE composite and predicted hardness using Equation (6-1).....	93
Figure 6.3: SEM images at x20,000 magnification A) 0 g/L saccharin B) 0.1 g/L saccharin C) 1 g/L saccharin D) 3 g/L saccharin E) 5 g/L saccharin.....	96
Figure 6.4: 2D colour plots of surfaces with colour representing height of the surface. A,B,C,D,E represent samples with 0, 0.1, 1, 3, 5 g/L saccharin respectively.	97
Figure 6.5: Line scans of surfaces taken at $y=400\ \mu\text{m}$ in Figure 6.4. A,B,C,D,E represent samples with 0, 0.1, 1, 3, 5 g/L saccharin respectively.....	99
Figure A1.1: Example of Ni-PTFE sample analyzed using image analysis showing an area fraction of 61.2% PTFE.	114
Figure A1.2: EDX spectrum obtained over area shown in image A taken at x500 mag.	115
Figure A2.1: SEM images for Ni-PTFE sample with 40 vol% PTFE. A-D are secondary electron images and E-F are backscattered electron images A) x500 B) x1,000 C) x5,000 D) x10,000 E)x500 F)x2,500	117
Figure A2.2: SEM images for Ni-PTFE sample with 45 vol% PTFE. A-D are secondary electron images and E-F are backscattered electron images A) x500 B) x1,000 C) x5,000 D) x10,000 E)x500 F)x2,500	118

Figure A2.3: SEM images for Ni-PTFE sample with 58 vol% PTFE. A-D are secondary electron images and E-F are backscattered electron images A) x500 B) x1,000 C) x5,000 D) x10,000 E)x500 F)x2,500 119

Figure A2.4: SEM images for Ni-PTFE sample with 69 vol% PTFE. A-D are secondary electron images and E-F are backscattered electron images A) x500 B) x1,000 C) x5,000 D) x10,000 E)x500 F)x2,500 120

Figure A2.5: SEM images for Ni-PTFE sample with 58 vol% PTFE. A-D are secondary electron images and E-F are backscattered electron images A) x500 B) x1,000 C) x5,000 D) x10,000 E)x500 F)x2,500 121

Figure A2.6: x500 magnification image of fracture surface of a Ni-PTFE sample containing approximately 70 vol% PTFE [Klingler 2014]..... 122

Figure A2.7: Fracture surface of a Ni-PTFE sample containing approximately 70 vol% PTFE A) x2,500 B) x5,000 magnification [Klingler 2014]. 122

Figure A6.1: Results for 3D surface profilometry with varying saccharin concentration A) 0 g/L B) 0.1 g/L C) 1 g/L D) 3 g/L E) 5 g/L. Heights in micrometers..... 131

Figure A6.2: Secondary electron SEM images at x500 magnification of Ni-PTFE samples containing varying saccharin concentration A) 0 g/L B) 0.1 g/L C) 1 g/L D) 3 g/L E) 5 g/L.... 132

List of Acronyms

ASTM	American Society for Testing and Materials
CNT	Carbon nanotubes
CTAB	Cetyltrimethylammonium bromide
CVD	Chemical vapour deposition
CVI	Colloidal vibration current
DC	Direct current
EDX	Energy dispersive X-ray spectroscopy
FCC	Face-centered cubic
PSD	Particle size distribution
PTFE	Polytetrafluoroethylene
SEM	Scanning electron microscopy
TEM	Transmission electron microscope
XRD	X-ray diffraction

List of Variables

a	Lattice parameter
B	Broadening of diffraction line
B_M	Measured broadening of diffraction line
B_S	Broadening of diffraction line for standard
C	Concentration of suspended particles in electrolyte
C_b	Concentration of metal ions in bulk electrolyte
D	Diffusion coefficient
d	Grain size
d_{hkl}	Interplanar spacing
dV_p/dt	Rate of strong adsorption of particles onto cathode surface
f	Atomic scattering factor; Ultrasound frequency
F	Faraday constant; Structure factor
f_{Ni}	Volume fraction of nickel
f_{Ni}	Volume fraction of PTFE
H	Hardness
H_0	Hardness value for material with very large grain size
H_C	Hardness value for composite
hkl	Miller indices
H_{Ni}	Hardness value for nickel
H_{PTFE}	Hardness value for PTFE
H_V	Vickers hardness

i_{hkl}	Intensity of diffraction peak
I_{hkl}	Orientation index
I_{in}	Input intensity of ultrasonic wave
I_L	Limiting current density
I_{out}	Output intensity of ultrasonic wave
I_{peak}	Peak current density
L	Gap length
n	Order of diffraction
p	Multiplicity factor
r_c	Critical radius for crystal nucleation
R_f	Roughness factor
z	Number of electrons in reduction reaction
α	Attenuation coefficient
γ_{LV}	Surface tension of liquid-vapour interface
γ_{SL}	Surface tension of solid-liquid interface
γ_{SV}	Surface tension of solid-vapour interface
δ	Diffusion layer thickness
η	Overpotential
ϑ	Strong adsorption coverage of particles on cathode
θ_0	Static Young's contact angle
θ_B	Bragg angle
θ_{CB}	Cassie-Baxter contact angle
θ_W	Wenzel contact angle

λ	Wavelength of X-ray
σ	Loose adsorption coverage of particles on cathode
σ_{UTS}	Ultimate tensile strength
σ_y	Yield strength
σ_{y0}	Yield strength for material with very large grain size

Chapter 1

Introduction

1 Introduction

Nature has proven to be an excellent source of inspiration for scientists and researchers in the development of structures and surfaces that display unique functional properties. A variety of very successful and widely used materials have been developed by replicating naturally developed structures which are part of a growing field known as biomimicry. One of the most famous examples is Velcro. The invention of Velcro was inspired by the familiar unpleasant experience of having burrs getting deeply tangled into clothes, hair or a pet's fur. Microscopic investigations of burrs reveal that the surface of a burr contains hundreds of micro hooks that are very effective at clinging to fibrous material.

There are many other examples found in all types of living creatures including the natural surface structure of shark skin, which allows sharks to move effortless and efficiently through water. Investigation of the structure has allowed for the replication of these surfaces that have shown to greatly reduce drag [Bechert et al. 2000]. Another great example is the imitation of the moth eye structure. The moth has the advantageous ability to see in the darkness of night due to highly anti-reflective properties developed in the corneal nipple structure of the moth eye. This structure has been studied and replicated showing potential in many applications including solar cells [Wilson and Hutley 1982].

One natural surface that has received significant attention in recent years is the Lotus leaf, which displays remarkable water repellency. Water droplets on the surface of the leaf form nearly perfect spheres and easily roll off the leaf taking dirt with them, which allows for the leaf to be self cleaning. This amazing phenomenon has since been observed on many different surfaces in nature including several types of leaves, the legs of water striders, as well as butterfly wings. This highly water repellent surface type is commonly referred to as a superhydrophobic surface [Bhushan and Jung 2006].

Superhydrophobic surfaces have many inherent properties that are extremely beneficial for a variety of applications. The self-cleaning ability noted on the Lotus leaf has practical applications for exteriors and windows of houses and cars. This technology has been implemented as a paint, named StoCoat LotusanTM by Sto corporation, a company based in Germany. In addition, superhydrophobic surfaces have also been shown to prevent the adhesion of bacteria on the surface and thus can be used to create anti-fouling coatings for use in underwater settings [Nosonovsky and Bhushan 2009]. Superhydrophobic surfaces have been investigated for use as anti-icing surfaces [Cao et al. 2009]. A potential application for non-icing surfaces would be on the exterior of airplane components to prevent the potentially dangerous build-up of ice that can occur during travel.

1.1 Development of Artificial Superhydrophobic Surfaces

Many thorough studies have been conducted on a variety of superhydrophobic surfaces found throughout nature. The study of these natural surfaces, including detailed characterization

of surface morphology, has allowed researchers to determine the surface structures responsible for imparting this unique surface property. As shown in Figure 1.1, SEM investigations have shown that leaf surfaces displaying superhydrophobicity have common surface characteristics which consist of micro and nano scale roughness features. The dual scale roughness takes on a hierarchical structure as nanoscale wax crystals protrude out of microscale bumps. It was determined that a combination of the dual scale hierarchical roughness along with the hydrophobic composition of the wax coating produces the superhydrophobic effect [Bhushan and Jung 2006].

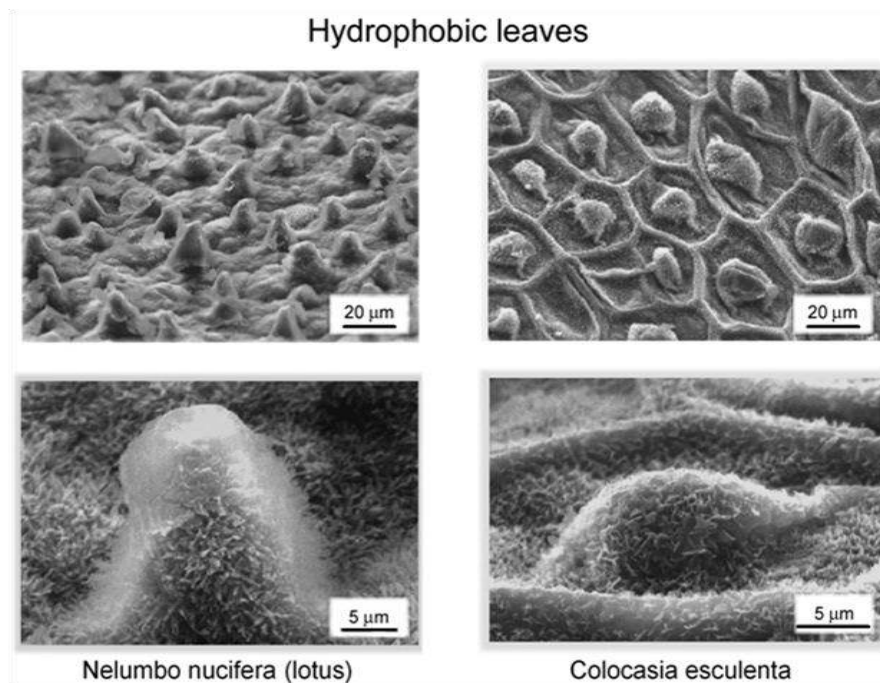


Figure 1.1: SEM images of leaf surfaces with hierarchical roughness that display superhydrophobic behaviour [Bhushan and Jung 2006]

Because of the many potential applications of superhydrophobic surfaces, there has recently been many attempts towards developing methods to replicate the structure of these

surfaces. A variety of techniques have been successfully employed to create superhydrophobic surfaces, shown in Figure 1.2, and include lithography, templating, self assembly, chemical vapour deposition (CVD), etching and plasma etching, and electrodeposition [Bhushan and Jung 2011].

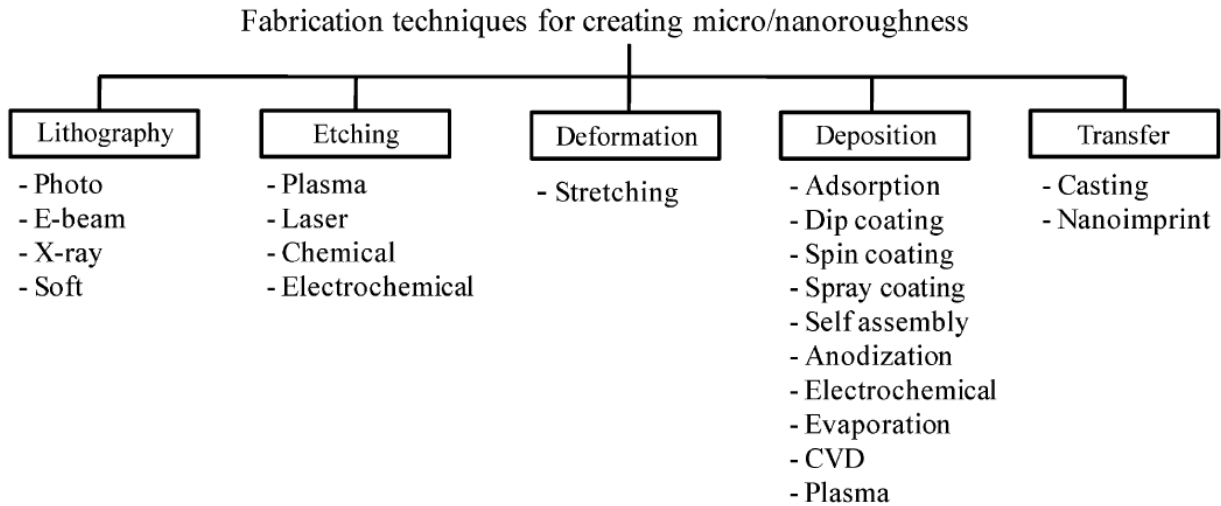


Figure 1.2: Typical methods to fabricate micro/nanoroughened surfaces. [Bhushan and Jung 2011]

One of the most successful methods used to create a superhydrophobic surface is lithography. Lithography techniques allow for very close control over the creation of fine micro/nano structures. This method is extremely useful for producing superhydrophobic surfaces that allow for in depth study of the science involved in creating stable superhydrophobic states.

Shirtcliffe et al. used photolithography to create an array of pillars on a photoresist material, SU-8 shown in Figure 1.3 [Shirtcliffe et al. 2004]. The material was treated with a fluorocarbon solution to make the material hydrophobic. The wetting angle was measured at

different pillar heights as well as different pillar diameters. Contact angles of up to 155° were achieved.

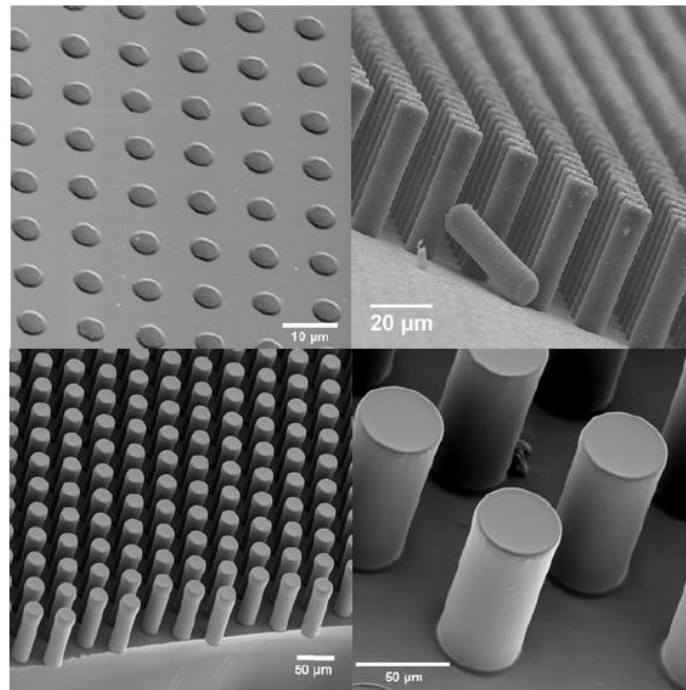


Figure 1.3: Patterned SU-8 surfaces, circular pillars of various heights and diameters in square patterns [Shirtcliffe et al. 2004]

While this technique allows for the most control over the structure of the surface, it is also a very expensive technique that cannot easily be scaled up for commercial purposes. Therefore, lithography techniques are best served when used in a laboratory setting.

Sun et al. used a bottom up approach to create a dual scale hierarchical structure. Two techniques were used to assemble silica spheres of two different sizes [Sun et al. 2007]. In one method, a single layer of monodispersed, micron-sized particles were adhered to a glass substrate. Submicron silica were deposited onto the micron spheres through electrostatic adsorption. The second method involved creating a template of the micron-sized silica particles

using polydimethylsiloxane (PDMS). The negative of this template was filled with a solution of submicron silica particles dispersed in ethanol. When the ethanol fully evaporated, the PDMS was removed and the resulting structure consisted of micron sized spheres made up of self assembled sub-micron silica particles. Images of the results of both methods are shown in Figure 1.4. The two surfaces were modified using a low surface energy coating, fluoroalkylsilane (FAS), to achieve superhydrophobicity.

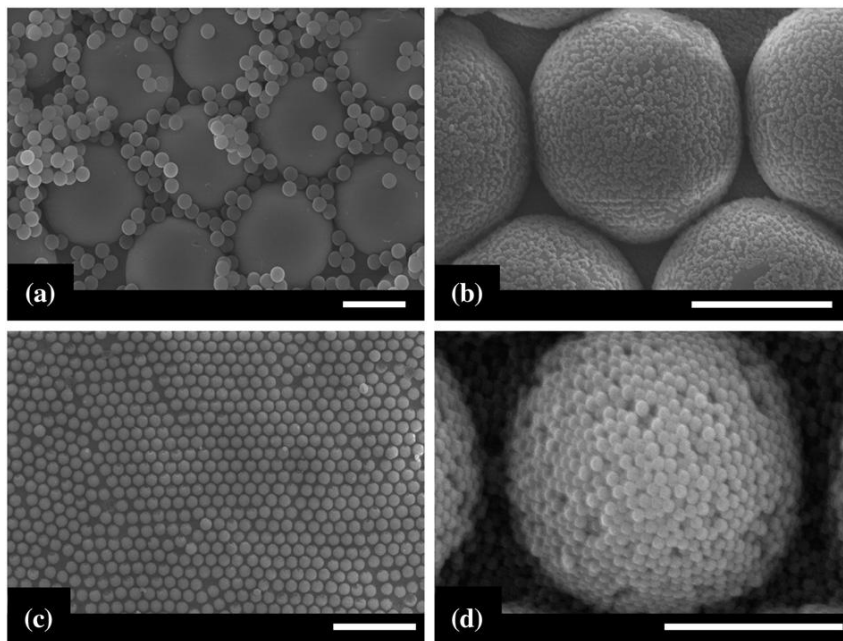


Figure 1.4: SEM images of dual-size-rough surface. (a) 1 μm silica spheres electrostatic-deposited on 8 μm silica sphere template. (b) 100 nm silica spheres electrostatic adsorbed on 8 μm silica sphere template. (c) micron sphere array assembled by 300 nm silica spheres. (d) an enlarged view of (c). Scale bars are 5 μm in a, b and d, and 50 μm in c. [Sun et al. 2007]

Xiu et al. created superhydrophobic surfaces by etching (100) silicon wafers using a KOH solution [Xiu et al. 2007]. The etching process produced pyramidal structures, which were then modified further to produce nanoscale features on the pyramids. To add nano-scale

roughness, a 5 nm thick, discontinuous gold film was deposited on the sample using e-beam evaporation, followed by further metal-assisted etching and finally removal of the gold film. Finally fluorination of the surface was done using a fluoroalkylsilane (perfluorooctyl trichlorosilane, PFOS) solution to create a low surface energy, superhydrophobic coating. The use of dual scale hierarchical structure was found to be extremely important in achieving superhydrophobicity. Figure 1.5 shows the contact angles achieved using the hierarchical structure compared to roughness at only one scale length.

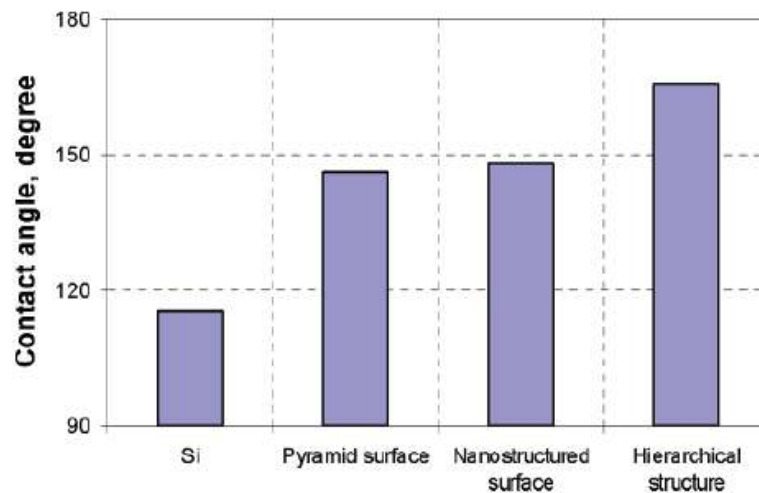


Figure 1.5: Contact angles on silicon surfaces with different surface texturing after PFOS treatment. For a silicon pyramid surface that possesses a hierarchical structure, a superhydrophobic surface with minimum hysteresis results after PFOS treatment. Nanostructures have been formed by Au-assisted etching of silicon surfaces in HF/H₂O₂ for 60 s with a Au layer of 5 nm on the silicon (111) surface. [Xiu et al. 2007]

Victor et al. developed a template method to produce low cost superhydrophobic polymer surfaces. To produce the template, a sheet of nanocrystalline nickel was textured by sand blasting followed by an etching process. The combination of the two surface treatments produced a dual scale, hierarchical roughness, which resembled the negative of the surface of

superhydrophobic leaves such as the quaking aspen leaf. The nickel template was then pressed into three different polymers (polypropylene (PP), polyethylene (PE), and polytetrafluoroethylene (PTFE)) at elevated temperatures which transferred the pattern to the surface. All three polymers displayed superhydrophobic behaviour after the pressing procedure, with PTFE showing the best results with a contact angle of 159° and a tilt angle below 5° [Victor et al. 2012].

An advancement of superhydrophobic surfaces is the creation of omniphobic surfaces which repel both water and non-polar liquids. Wong et al. took inspiration from the *Nepenthes* pitcher plant which locks in an intermediate liquid which allows the surface of the plant to repel almost all other liquids [Wong et al. 2011]. The material used for the omniphobic surface consists of a porous solid substrate which is impregnated by a low surface tension liquid. The resulting material has a surface composed of a thin layer of low surface energy liquid that repels all other liquids that are placed on the surface. Very low contact angle hysteresis ($<2.5^\circ$) was measured for a variety of liquids, including complex organics such as crude oil and blood. The liquid surface is very smooth and lacks defects which will cause pinning of droplets. Additional benefits include functionality in higher pressure and self-healing capability [Wong et al. 2011].

The examples outlined above show many different techniques towards producing superhydrophobic surfaces. Two concerns for the commercial production of superhydrophobic surfaces are the ability to scale up in a cost effective manner, and the flexibility of material selection. Techniques such as lithography and CVD are very expensive and are not easily scalable. Many techniques were developed for polymer substrates or require the use of a chemically surface layer modification to achieve superhydrophobicity. In contrast, there have

been few studies on the creation of superhydrophobic surfaces using a metal without the use of an additional surface coating.

There has been some success in creating superhydrophobic metal surfaces by carefully structuring the metal surface to mimic the Lotus leaf. Two examples of this approach used a two step electrodeposition processes. Hang et al. created a superhydrophobic nickel surface by electrodepositing nickel to produce micro cones. An additive, ethylenediamine dihydrochloride, was used to modify the crystal growth, producing the conical structure. This was followed by a subsequent electrodeposition step using different plating parameters to create nano cones on top of the micro cones, replicating the very high roughness, hierarchical structure observed on the surface of superhydrophobic leaves. This hierarchical structure produced a wetting angle of 154° [Hang et al. 2010]. Tian et al. used a slightly different approach where electrodeposition of nickel was used to produce an array of nanocones which was then followed by electroless deposition of nickel hemispherical caps [Tian et al. 2012]. The wetting angle of the nickel nanocone array improved from 135° to 153.6° with the addition of the electroless deposition step.

Producing a very rough structure on a metal surface is able to produce a superhydrophobic surface by trapping a significant amount of air in between the metal surface and the liquid, creating a metal-air-water composite interface. For these materials, since the underlying metal is hydrophilic in nature, wear or damage to the sharp surface features will allow water to penetrate to the metal surface which may reduce the contact and tilt angle after extended use in application.

1.2 Objectives and Structure of Thesis

The objective of this thesis is to develop a commercially viable method of preparing a superhydrophobic surface using a metal matrix composite. To accomplish this goal the surface energy of a metal surface will be altered through the addition of polymer particles. The materials of choice for the composite are a nanocrystalline nickel matrix and polytetrafluoroethylene (PTFE) particles. The use of a composite material will exploit the many advantageous properties of nanocrystalline coatings, in particular high strength and hardness, while the very low surface energy of PTFE can be used to alter the surface chemistry as well as the surface roughness. Electrodeposition is a well established, commercially viable technique that has proven to be an effective method to produce i) fully dense nanocrystalline coatings [Haasz et al. 1995] and ii) composite coatings using a wide variety of secondary particles [Roos et al. 1990]. These two electrodeposition techniques are to be combined to produce a nanocrystalline Ni-PTFE composite. The final goal is to develop a multifunctional coating that can be used in applications where there is a need for enhanced strength as well as non-wetting properties.

There are several inherent advantages that an electrodeposited Ni-PTFE superhydrophobic coating has over existing superhydrophobic materials. As previously described advantages include the simplicity and low cost as well as the use of high strength metal matrix. The electrodeposition technique provides another unique advantage as the process can be applied to complex shapes. An example of where this is advantageous is the application of the coating to the inside surface of a pipe. This would be extremely difficult, if not impossible, with many of the line of sight techniques previously used. A second unique advantage to this material is the potential for long lasting superhydrophobicity. PTFE particles can be evenly

distributed throughout the thickness of the coating, which means as the surface wears away new PTFE particles are being continuously exposed maintaining the water repellency. The use of Ni-PTFE composite coatings will have a variety of other beneficial properties aside from superhydrophobicity including a low friction surface and good corrosion resistance.

The structure of the thesis is as follows. Chapter 2 will cover the relevant background information as well as recent developments found in the literature. The background of superhydrophobic surfaces, electrodeposition of composite materials as well as the electrodeposition of nanocrystalline metals will be discussed.

Chapter 3 will present the experimental procedures used to i) make the composite material and ii) characterize their structure and wetting properties.

Chapters 4 through 6 will cover the results and discussions. The research presented is broken down into four distinct areas of study, as illustrated in Figure 1.6. Chapter 4 covers the first two areas. The first area of study will focus on the co-deposition of the PTFE particles in a nickel matrix with emphasis on controlling the concentration of PTFE in the composite coating. The next step is to understand how changes in the amount of PTFE affect the wetting properties of the coating. In this section the composition of the coating is optimized to obtain the highest contact angle possible.

In Chapter 5 the focus of the project is shifted to the metal matrix. Measurements of hardness of pure nickel deposits produced from plating solutions containing saccharin additions are compared to grain size to investigate the improvement in mechanical properties obtained through grain size refinement. Finally in Chapter 6, the results from Chapters 4 and 5 are

brought together. Nickel electrodeposition was done with the addition of both PTFE and saccharin in the plating bath to produce a nanocrystalline Nickel-PTFE composite. Samples are characterized using scanning electron microscopy (SEM), grain size measurements, hardness testing, contact angle measurements, and surface profilometry.

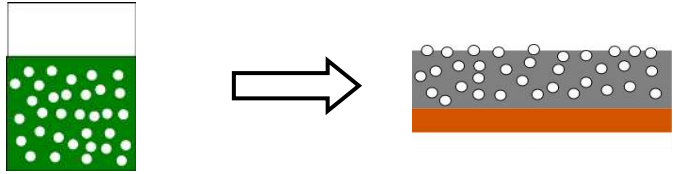
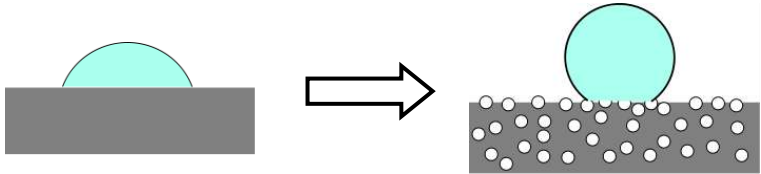
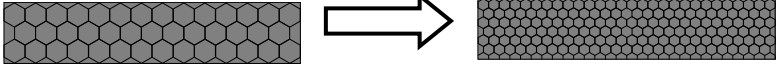
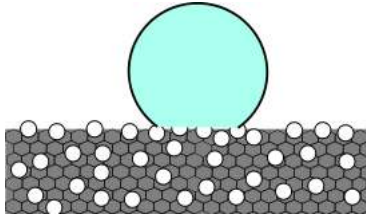
Chapter 4	Electrodeposition of Ni-PTFE Composite	
	Effect of PTFE on Wetting Properties	
Chapter 5	Grain Size Refinement of Nickel	
Chapter 6	Nanocrystalline Ni-PTFE Composite Coating	

Figure 1.6: Outline of the structure of the thesis

Chapter 2

Background Information

2 Background Information

2.1 Superhydrophobic Surfaces

2.1.1 Wetting of Smooth Surfaces

The interaction between a sessile (at rest) liquid droplet and a perfectly smooth solid surface is described by Young's equation,

$$\gamma_{LV} \cos \theta_0 = \gamma_{SV} + \gamma_{SL} \quad (2-1)$$

where θ_0 is the static contact angle and γ_{SL} , γ_{SV} , γ_{LV} are the surface tensions of the solid-liquid, solid-vapour, and liquid-vapour interfaces respectively. This interaction is governed by a balance of the surface tensions of the three interfaces involved in the system. The magnitude of these parameters dictates the angle that the liquid droplet will form with the flat solid surface, known as the contact angle, shown in Figure 2.1.

Contact angles of a liquid on a solid surface can theoretically range from 0° - 180° , as shown in Figure 2.2. A contact angle of 0° refers to complete wetting where the liquid spreads out flat

across the surface (Figure 2.2 e), and a 180° contact angle means that the liquid will form a complete sphere on top of the surface minimizing the solid-liquid interface (Figure 2.2 a),.

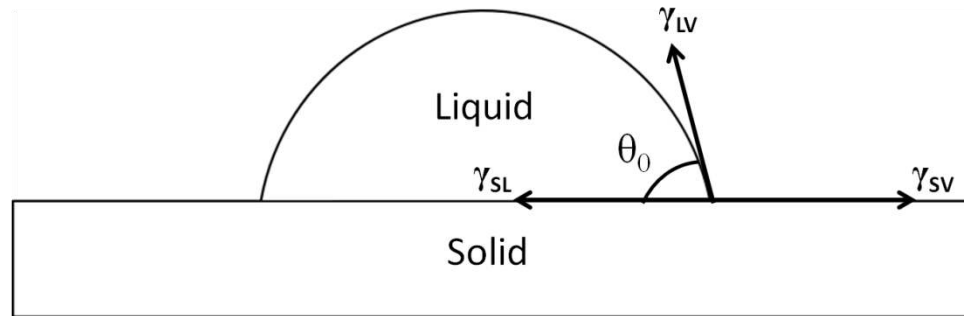


Figure 2.1: Water droplet on a flat solid surface, showing the static contact angle θ_0 , and the surface tensions at each interface γ_{SL} (solid-liquid), γ_{LV} (liquid-vapour), and γ_{SV} (solid-vapour).

In the case of water droplets, a solid surface can be described as either hydrophobic or hydrophilic based on the contact angle formed by the water droplet. A surface is considered hydrophobic when $\theta_0 \geq 90^\circ$ and hydrophilic when $\theta_0 < 90^\circ$. Flat homogeneous surfaces usually have a θ_0 no greater than 120° ; however, significantly higher contact angles can be achieved with changes to the surface roughness, which will be discussed further in section 2.1.2. When the contact angle of a surface is equal to or greater than 150° , the surface is very resistant to wetting and is classified as superhydrophobic [Bhushan and Jung 2006], shown in Figure 2.2 (b).

2.1.2 Wetting of Non-Ideal Surfaces

To describe the wetting behaviour of real surfaces, several modifications to Young's equation have been made. Young's equation applies only to perfectly flat, chemically

homogeneous surfaces. In reality many surfaces will have substantial surface roughness, areas of different chemical composition, or a combination of both.

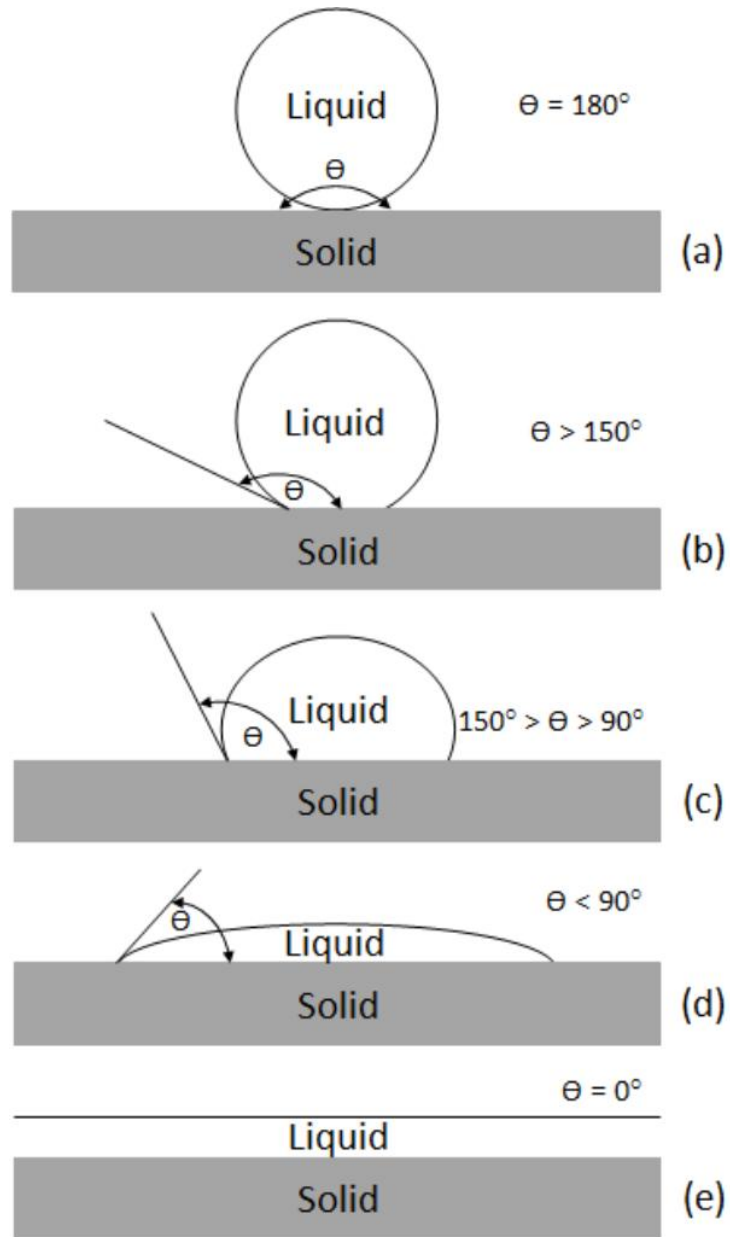


Figure 2.2: Wetting on solid surfaces: (a) complete non-wetting, (b) superhydrophobic (c) hydrophobic, (d) hydrophilic (e) and complete wetting [Victor 2012]

Some of the first research into the wetting of rough surfaces was presented by Wenzel in 1936. In this work it was determined that the contact angle of a surface will be significantly altered when roughness is present on the surface. Wenzel explains that for a water droplet on a solid surface, an increase in surface roughness will result in an increase in the surface area of the solid in contact with water. This will alter the surface energy of the solid-liquid interface causing the contact angle of the droplet to change [Wenzel 1936]. Wenzel modeled this wetting behaviour using the following equation,

$$\cos\theta_W = R_f \cos\theta_0 \quad (2-2)$$

where θ_W is the observed contact angle on the rough surface, θ_0 is the contact angle of a flat surface as described by Young's equation, and R_f is a roughness factor. The roughness factor is defined as the actual surface area divided by the geometric surface, or the surface area if the surface was perfectly flat. This equation shows that the roughness of a surface amplifies the original wetting properties of the surface such that increasing the roughness of a surface will cause a hydrophobic surface to become more hydrophobic (higher contact angle) and a hydrophilic surface to become more hydrophilic (lower contact angle), as seen in Figure 2.3 [Jung and Bhushan 2006].

The Wenzel wetting equation (Eq. (2-2)) can be used to model the wetting state of a droplet on a chemically homogeneous, rough surface. In the case of a chemically dissimilar secondary material being present on a composite surface, the resulting contact angle is described by the Cassie equation [Cassie 1948],

$$\cos\theta_{CB} = f_1\cos\theta_{01} + f_2\cos\theta_{02} \quad (2-3)$$

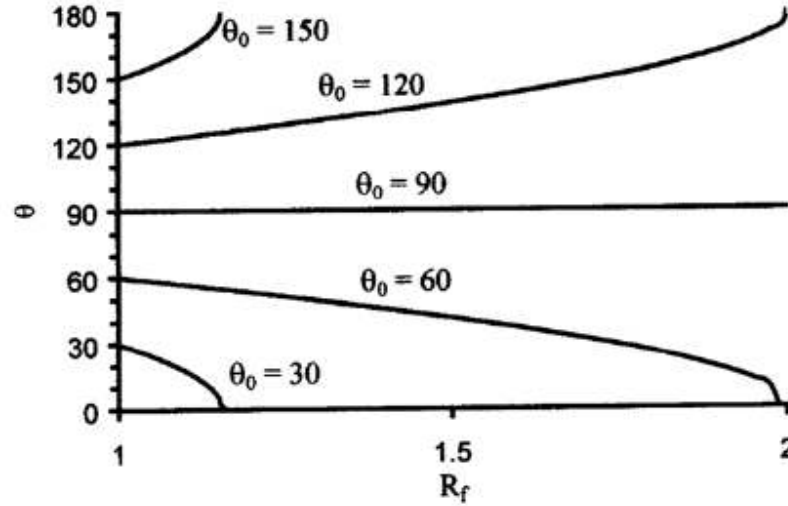


Figure 2.3: The amplification effect of roughness factor R_f in the Wenzel equation [Jung and Bhushan 2006].

where θ_{CB} is the wetting angle of the composite surface, f_i is the fraction of solid surface in contact with the water droplet for each material, and θ_{0i} are the Young's contact angles for each solid surface. In special circumstances, surfaces of significant roughness can cause air to be trapped between the solid and liquid. In this scenario, the water droplet will be sitting on top of a composite interface composed of solid and air as displayed in Figure 2.4. This is shown in Equation (2-4) and is often referred to as the Cassie-Baxter state. The equation describing this phenomenon is the same as Equation (2-3), where the second phase is air with $\theta_0 = 180^\circ$. In this modified version of Equation (2-3), f is the solid fraction in contact with the liquid and θ_0 is the Young's contact angle of the solid material [Cassie and Baxter 1944].

$$\cos\theta_{CB} = f\cos\theta_0 + f - 1 \quad (2-4)$$

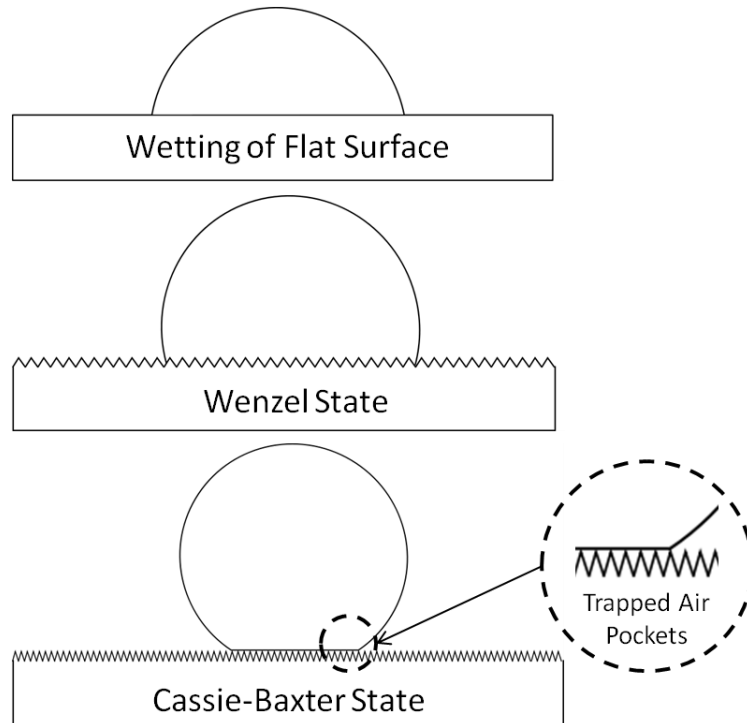


Figure 2.4: Visual representation of the different wetting states

While a very high static contact angle ($>150^\circ$) is one measure to determine superhydrophobicity, the ease with which a droplet can roll over the surface is crucial to provide a self-cleaning effect. The ability for a droplet to roll off of a surface can be quantified by a parameter known as the tilt angle. The tilt angle of a droplet is the minimum angle a surface must be tilted to for the droplet to first begin to roll. When a liquid droplet first begins moving along a surface, two separate contact angles can be observed, the advancing contact angle and receding contact angle. The difference in these two contact angles is known as contact angle

hysteresis. A low contact angle hysteresis, meaning similar advancing and receding contact angles will result in a low tilt angle allowing droplets to easily roll off the surface. A high contact angle hysteresis will lead to higher tilt angles and much “stickier” surfaces. Much work has been done in determining the dynamics of a rolling water droplet on the surface and how to minimize contact angle hysteresis. It has been shown that systems in the Wenzel state as well as the Cassie-Baxter state can display very high contact angles, over 150° , however, the Cassie-Baxter state results in a lower contact angle hysteresis allowing droplets to easily slide off the surface [Quéré et al. 2003]. McHale et al. used theoretical calculations to show that when compared to a smooth surface, droplets in the Wenzel states will have an amplification of the contact angle hysteresis whereas in the Cassie-Baxter state contact angle hysteresis is attenuated [McHale et al. 2004]

Priest et al. have shown that the distribution and nature of the discontinuous phase of a composite will affect the contact angle hysteresis [Priest et al. 2009]. The study used two templates, one containing arrays of square pillars and the other containing arrays of square holes. In both situations, a Cassie-Baxter state was achieved where air was trapped either between the pillars or in the holes of the solid. For this composite, the air is the more hydrophobic region while the solid surface is more hydrophilic. For the sample consisting of pillars, the trapped air formed a continuous hydrophobic matrix with the tops of the pillars representing hydrophilic defects. The sample containing holes was the reverse of this as the solid surface is the more hydrophilic matrix with the trapped air in the holes working as hydrophobic defects. For these two cases, it is found that the contact angle hysteresis will differ depending on the nature of the defect as well as the defect density. This is due to the dynamics of the triple line while passing

over areas of different composition. For both situations it was found that contact angle hysteresis increased with increasing defect density (pillar/hole) [Priest et al. 2009].

2.2 Synthesis of Composite Coatings using Electrodeposition

Electrodeposition is a well established commercial technique for the production of thin films, metal coatings, as well as free-standing parts. Electrodeposition is a versatile technique as many different metals and alloys can be deposited onto a variety of conductive surfaces [Schlesinger and Paunovic 2010]. Many studies in the field of electrodeposition have focused on enhancing the properties of electrodeposited coatings. Properties of electrodeposited coatings can be modified, for example, by adding secondary particles to the electrodeposition bath and co-depositing the particles to form metal-matrix composite materials. The use of secondary particles has garnered significant interest and much work has been done studying the properties attainable using different particle types as well as the fundamental co-deposition mechanism to allow for the inclusion of non-conductive, inert particles.

2.2.1 Mechanism for Co-deposition

Some of the first work towards detailing the co-deposition mechanism was done by Guglielmi in 1972 [Guglielmi 1972]. In this work, Guglielmi described the co-deposition mechanism of particles as a two step process, based on the influence of two distinct phenomena, electrophoresis and adsorption. The first step in the process is loose adsorption of the particles, which occurs when particles come in close vicinity of the cathode surface. This adsorption is completely physical as any charge on the particle is screened by counter ions and solvent

molecules. The second step is a strong electric-field assisted adsorption. The electric field present around the cathode strips away screening ions exposing the particle surface charge and results in strong electric-field assisted adsorption. In this step it is assumed that metal ions in the bath preferentially adsorb on the particle surface, thus imparting a positive charge on the particles. This proposed process is illustrated in Figure 2.5, where loose adsorption results in a high coverage of particles, and then a fraction of these particles are strongly adsorbed allowing the metal matrix to grow around the particles embedding them within the coating.

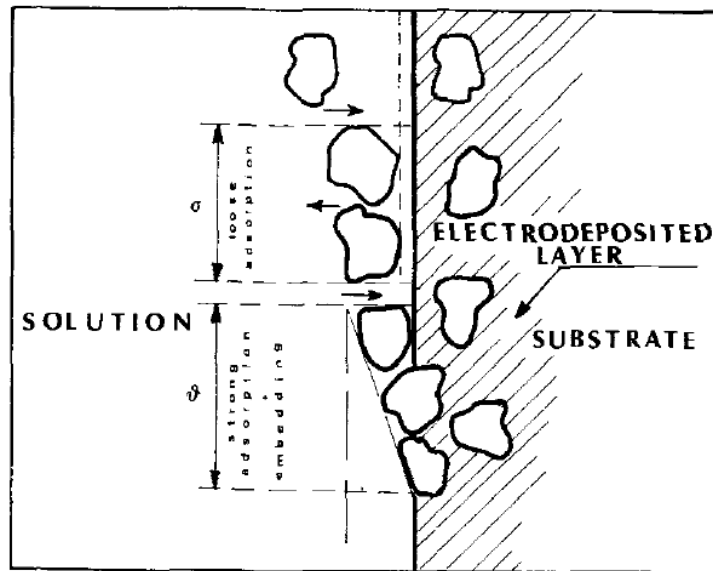


Figure 2.5: Guglielmi's proposed two step process for particle incorporation [Guglielmi 1972]

The weak adsorption step is dependent on the concentration of suspended particles in the bath and can be modeled using the Langmuir adsorption isotherm. A modification to the adsorption expression is needed to account for area unavailable for adsorption due to strongly adsorbed particles already on the surface. The expression used to model the weak adsorption is as follows [Guglielmi 1972],

$$\sigma = \frac{kC}{1 + kC} (1 - \vartheta) \quad (2-5)$$

where σ and ϑ are the loose and strong adsorption coverage of particles respectively, as shown in Figure 2.5, C is the concentration of the suspended particles in the bath, and k is a constant that describes the intensity of the interaction between particle and cathode.

The rate of particle co-deposition can be described by the rate that loose adsorption coverage, σ , becomes strongly adsorbed. The strong adsorption rate is dependent on the electric field at the cathode. The overall rate of strongly adsorbed particles, dV_p/dt , on the surface is described by the following expression [Guglielmi 1972],

$$\frac{dV_p}{dt} = \sigma v_o e^{B\eta} \quad (2-6)$$

where the rate dV_p/dt is the volume of particles strongly adsorbed on 1 cm² of cathode surface per second, σ is the loose adsorption coverage calculated using Equation (2-5), η is the overpotential of the system, and v_o and B are constants. The overpotential of the system is related to the current density that is used in the deposition process. The constants in Equations (2-5) and (2-6) can be determined through experimental work where the particle content in a deposit is compared to particle concentration in the bath at different current densities [Guglielmi 1972].

More recent studies have further developed the original model by Guglielmi. In 1977 Celis and Roos tested the model proposed by Guglielmi using copper sulfate baths with alumina

particles [Celis and Roos 1977]. Their experimental results showed good agreement with the Gugliemli model for the co-deposition of α -alumina and copper. Particular attention was given to the second strong adsorption step, by studying the effect of current density on the deposition rate. It was determined that the copper ions indeed adsorbed onto the alumina surface and increasing the current density lead to a higher rate of reduction of the adsorbed ions and thus increased the co-deposition rate of alumina. It was also found that a small addition of monovalent thallium ions acted as a catalyst to increase the rate of reduction of copper ions, allowing for an increase in the amount of embedded alumina.

Gugliemli's model is able to quantify the effects of both particle concentration and current density of specific systems; however the model is quite limited in predicting results for general cases due to its simplicity. Important factors in the co-deposition process, such as bath agitation, particle size and type, are left out of the model. Fransaer, Celis and Roos added a trajectory model to include the particle motion in the bath caused by agitation [Fransaer et al. 1992]. A rotating disk electrode was setup to give control over the hydrodynamic conditions. Theoretical predictions were verified with experimental results and it was shown that fluid flow velocities and tangential shearing force were major factors in the co-deposition of particles. It was determined that rate at which particles are brought to the electrode is controlled entirely by convection brought on by the rotating disk as well as dispersion forces [Fransaer et al. 1992].

Berçot et al. also adapted the Gugliemli model to predict the co-deposition of PTFE particles when using magnetic stirring [Berçot et al. 2002]. It was determined that for a given concentration of PTFE particles in a nickel plating bath, an optimum agitation rate (rpm) exists to maximize particle incorporation rate. Experimental results showed a low incorporation rate at

low rpm when there was a laminar flow as well as at very high rpm during pure turbulent flow. Maximum particle incorporation was found when the stirring rate produced a transient laminar-turbulent flow [Berçot et al. 2002]. A corrective factor was determined from these experimental results to take into account the effects of magnetic stirring and combined with the work of Gugliemli, theoretical models agreed closely with experimental results for the incorporation of PTFE particles into a nickel coating.

The mechanism of co-deposition is very complex and while many different models have shown agreement with experimental results, usually these only hold true for systems under specific conditions. There are many variables at play in the co-deposition process and the modeling of a general system that can be applied universally has not yet been achieved.

2.2.2 Effect of Surfactant on Co-deposition Process

Surfactants are long chained amphiphilic molecules, meaning they contain both a hydrophobic and hydrophilic end. This unique property causes the surfactant molecules to accumulate at interfaces, reducing the surface energy and allowing for liquids to better wet solid surfaces. The addition of surfactants in electroplating baths has long been used as a method to lower surface tension to prevent hydrogen bubbles clinging to the cathode surface resulting in pitting in the electrodeposit [Di Bari 2010]. The use of surfactants in electroplating becomes very important when secondary particles are added to the bath. As such, there has been significant focus on the effect of surfactants in order to optimize the co-deposition process. The nature and concentration of surfactants used plays a significant role in the stability of the particles in solution as well as the surface charge present on particles.

The stability of particles in colloidal solutions relies on creating repulsion forces between particles to prevent agglomeration. This can be accomplished in two ways, using steric or electrostatic methods. Steric repulsion occurs when non-ionic macromolecules, such as long chained polymers, are adsorbed on to the surface of different particles. Particle agglomeration is prevented as it is thermodynamically unfavourable for polymer chains on different particles to overlap, thus particles have to maintain a minimum distance away from each other [Napper and Netschey 1971]. This is the mechanism when non-ionic surfactants are used to increase stability.

Electrostatic repulsion occurs when colloidal particles have a similar electric charge surrounding each particle causing a repulsion force between particles. The formation of an electric charge starts with the phenomenon of inert particles gaining surface charge in an electrolyte solution. A particle surface becomes charged in an electrolyte solution through specific adsorption of charge determining ions [Lyklema 1995]. This means that in an electrolyte, a particular ion type will have a stronger affinity to adsorb on the particle surface resulting in a build-up of charge whose sign depends on the nature of this ion.

Once a surface charge has been established, the associated electrostatic field will affect the rest of the ions in the electrolyte. As a result, an electrical double layer forms around the particle, with an associated electrical potential depicted in Figure 2.6 [Duhkin and Goetz 2010]. In this figure, two distinct layers surrounding a charged surface are highlighted, the Stern layer and the diffuse layer. In the Stern layer, counterions specifically adsorb near the surface forming a sublayer. The diffuse layer also consists of an excess of counterions and a deficit of co-ions (ions having the same charge as the surface) however the ions are less firmly adsorbed to the particle in the region. At the edge of the diffuse layer is the slipping plane, and the distance

between the particle and the slipping plane is known as the Debye length. The slipping plane is significant because if agitation is applied, the liquid outside of the slipping plane will flow past the particle while the liquid inside the slipping plane will remain stationary in reference to the particle.

The double layer consists of a high concentration of counterions which screens the surface charge, resulting in a drop in the potential as the distance from the particle surface increases. The electrostatic charge of a particle is therefore defined as the potential at the slipping plane, known as the zeta potential, ζ . When the magnitude of zeta potential is greater than 25 mV, sufficient electrostatic force exists around each particle to provide enough repulsive force to prevent formation of agglomeration, and the colloid is considered stable [Duhkin and Goetz 2010].

The use of ionic surfactants allows for control over the surface charge around the particle. Ionic surfactants have a strong affinity to hydrophobic particles in an aqueous environment due to the long hydrophobic tail component of the surfactant molecule. Therefore, surfactant molecules will surround the hydrophobic particle with the tail facing towards the particle and the charged head group out towards the solution, thus acting as an effective surface charge for the particle. Choice of cationic or anionic surfactants allows control over the surface charge of particles in a colloid solution.

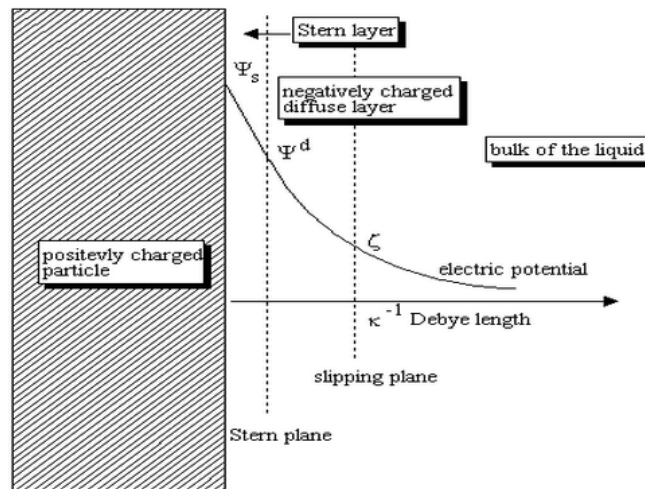


Figure 2.6: Electric double layer around charged particle in solution. The zeta potential is defined at the outer boundary of the diffuse layer (slipping plane) [Duhkin and Goetz 2010]

Experimental work has been done to quantify the effect surfactants have on the particle incorporation during both electrodeposition and electroless deposition. Helle and Walsh suggested the use of cationic surfactants provides stability to the bath as well as creating artificially high positive zeta potentials which will aid in the co-deposition process [Helle and Walsh 1997]. The cationic surfactants provide a positive charge to the surface of the particle, increasing the attraction to the cathode surface and the chance of the particle being embedded in the coating. Guo et al. tested this theory by comparing the co-deposition effectiveness of carbon nanotubes (CNT) with nickel when using no surfactant, an anionic surfactant (sodium dodecylsulfate, SDS), and a cationic surfactant (hexadecyltrimethylammonium bromide, CTAB). When 0.3 g/L of CNT were added to the nickel plating bath, the results showed that with no surfactant the coating contained 5.07 wt% CNT, with 0.6 g/L of anionic SDS the coating contained 4.91 wt % CNT, and with 0.6 g/L of cationic surfactant a coating with 10.84 wt%

CNT was produced [Guo et al. 2008]. The co-deposition effectiveness was slightly decreased with the addition of SDS and greatly increased with the addition of CTAB, agreeing with the proposed effect stated by Helle.

Similar results were found in the work by Mafi and Dehghanian on electroless Ni-P-PTFE composite plating. Figure 2.7 summarizes the results, where cationic surfactant (CTAB) produced the highest amount of co-deposited PTFE, anionic surfactant (SDS) prevented co-deposition altogether, while a non-ionic surfactant (poly-vinylpyrrolidone, PVP) and no surfactant allowed for a moderate amount of co-deposited PTFE [Mafi and Dehghanian 2011].

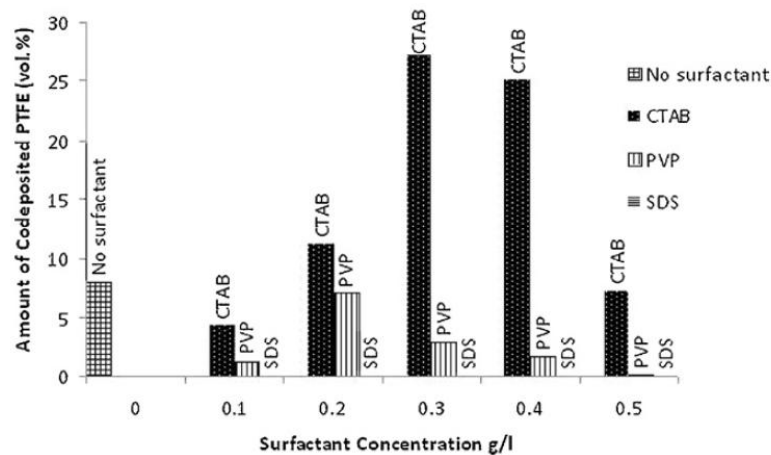


Figure 2.7: Amount of co-deposited PTFE with different surfactants. CTAB is a cationic surfactant, PVP is non-ionic and SDS is anionic surfactant [Mafi and Dehghanian 2011].

Kilic et al. studied electrodeposition of nickel with SiC nanoparticles, and found that as CTAB concentration in the bath was increased from 0-400 mg/L the zeta potential increased from slightly negative to +20 mV as shown in Figure 2.8. This ultimately led to an increase in the co-deposited SiC from 1.26-11.37 vol% [Kilic et al. 2013]. Similar results for the Ni-SiC

system were observed by Rudnik et al. confirming the positive influence CTAB has on electrodeposition [Rudnik et al. 2010]. Rudnik et al. measured the adsorption of Br^- and Ni^{2+} ions to the SiC surface as a function of CTAB concentration in the bath. As CTAB concentration increased, the amount of nickel ions adsorbed on the surface decreases. However, the amount of SiC deposited increased at higher concentrations of CTAB, suggesting that the cationic surfactant provides enough attraction to the cathode and the adsorption of nickel ions onto the particle surface is not crucial to the co-deposition process [Rudnik et al. 2010].

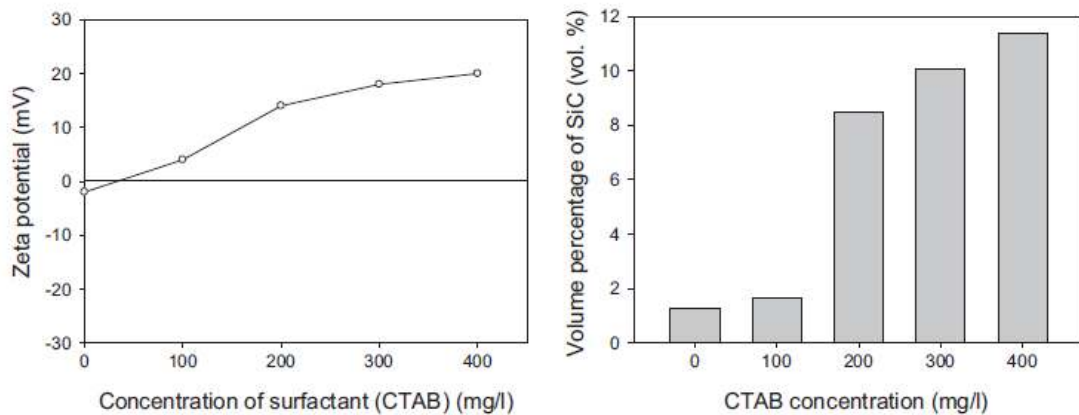


Figure 2.8: Effect of cationic surfactant concentration in co-deposition of SiC particles [Kilic et al. 2013]

2.2.3 Effect of Particles on Coating Properties

Many different types of particles have been used in composite plating to impart a variety of properties on the coatings. The most common material properties that are enhanced in this way include hardness, coefficient of friction and corrosion resistance. Functional surface properties such as increased hydrophobicity have been studied as well.

Early work in this field was done by Zimmerman et al., where SiC particles were incorporated into a nanocrystalline nickel matrix in order to enhance hardness and strength [Zimmerman et al. 2002]. The SiC concentration in a Watt's plating bath was increased from 20 g/L to 100 g/L which resulted in SiC content in the nickel coating ranging from 0.1-3 wt%. Microhardness measurements showed a maximum hardness of 659 kg/mm^2 (659 HV), which is similar to the hardness of pure nanocrystalline nickel. It was concluded that the addition of SiC particles did not increase the hardness of the coating and the high hardness values were attributed to the nanocrystalline structure of the nickel matrix. Similar results for the Ni-SiC system was found by Gul et al. In this study a maximum of 10 vol% (~4wt%) of submicron SiC particles was co-deposited reaching a maximum hardness of 571 HV [Gul et al. 2010]. No grain size measurements were done in this study to take into account effect of any grain refinement in the process. Rudnik et al. studied the effect of surfactant on co-deposition of SiC particles. In this study, the maximum amount of co-deposited SiC was about 17 vol% which resulted in a microhardness of over 900 HV. The increase in hardness was attributed to both the presence of hard SiC particles as well as fine grains (20-30 nm) in the nickel matrix cause by the addition of the surfactant CTAB [Rudnik 2010].

Coatings with enhanced corrosion resistance have been made with the addition of inert secondary particles such as PTFE using both electrodeposition as well as electroless deposition. Mafi and Dehghanian used electroless deposition to produce Ni-P-PTFE coatings with the aid of various surfactants. The maximum amount of PTFE incorporated in the coatings was 27.2 vol% with the aid of cationic surfactant CTAB. At this coating composition, the corrosion resistance in a 3.5% NaCl solution increased 16 times over the Ni-P deposited [Mafi and Dehghanian 2011]. Improvements in corrosion resistance of electroless Ni-P-PTFE were similarly found in

other studies eg [Ankita and Singh 2011, Rossi et al. 2003, Wang et al. 2011]. Omar and Morsi electrodeposited Ni-PTFE coatings and compared the corrosion properties to mild steel. With a composition of 38 vol% PTFE, Ni-PTFE coatings displayed a corrosion rate of 3.1×10^{-4} mpy (mils per year) in a 5% NaCl solution, compared to 9.1 mpy for mild steel [Omar and El Morsi 2008]. This shows that electrodeposited Ni-PTFE coatings provide good corrosion protection to mild steel surfaces.

Gyawali et al. studied the corrosion properties of electroplated composite coatings containing hexagonal boron nitride (h-BN) nanosheets in a nickel matrix. The corrosion rate of Ni-h-BN composites was approximately 12 times lower than the pure Ni coatings [Gyawali et al. 2013]. The lower corrosion rate was attributed to higher corrosion resistance of h-BN than nickel, the modification of the nickel crystal orientation with addition of nanoparticles, as well as the possibility of the formation of many corrosion micro cells between nanoparticles and nickel [Gyawali et al. 2013].

The inclusion of soft, self lubricating particles can reduce the coefficient of friction of a coating resulting in favourable dry lubrication properties leading to lower wear rates. The most commonly used secondary particle of this type is PTFE due to its very low coefficient of friction. Pena-Munoz et al. studied the coefficient of friction of Ni-PTFE coatings produced through electrolytic and electroless deposition. Tribological measurements were done using a standard tribometer ball/plan with a 10 mm diameter steel ball. The coefficient of friction decreases from approximately 0.6 for electrodeposited pure Ni to 0.2 for Ni-PTFE. An increase in the amount of PTFE in the coating allowed for the coefficient of friction to remain at 0.2 for a greater number of cycles showing greater wear resistance. The electroless coatings showed a similar coefficient

of friction but better wear resistance, which is attributed to the presence of phosphorous in nickel matrix [Pena-Munoz et al. 1998]. Wu et al. measured the coefficient of friction for Ni-P samples containing 0, 4.2, 10.6 and 15.2 wt% PTFE using a load of 70 N and rotation speed of 50 rpm for 20 minutes of wear. The addition of 4.2 wt% PTFE to Ni-P matrix decreased the coefficient of friction from approximately 0.6 to 0.33, and this is further reduced to 0.12 when additional PTFE (15.2 wt%) is deposited [Wu et al. 2011]. Although the antifriction properties were shown to increase in this study, the addition of soft PTFE particles lead to worse wear resistance at heavy applied loads [Wu et al. 2011]. The addition of PTFE particles has shown to increase wear resistance through dry lubrication in gold [Rezrazi et al. 2004] and bronze [Balaji et al. 2006] coatings as well.

Several electroless Ni-P-PTFE coatings have been developed that are commercially available including Niflor by Surface Technology plc, Tribocoat[®] by Mold-Tech[®], Apticote 450 by Poeton, and MicroLube by Micro Plating Inc. These coatings are marketed towards low friction applications with additional benefits including corrosion resistance.

A unique method of producing wear resistant and corrosion resistant properties involves the inclusion of liquid filled microcapsules into a metal matrix. Xu et al. used electrodeposition to deposit microcapsules into a copper matrix (shown in Figure 2.9), where liquid from the microcapsules is deposited gradually onto the surface as the coating is worn down. The microcapsules have a methyl cellulose shell and the core is a liquid hydrophobic agent, which is a mixture of KF-99 hydrogen-containing silicone oil and inhibitor 1H-Benzotriazole [Xu et al. 2011]. The coatings display excellent wear resistance, corrosion resistance as well as hydrophobic properties in both copper and nickel matrices [Xu et al. 2011].

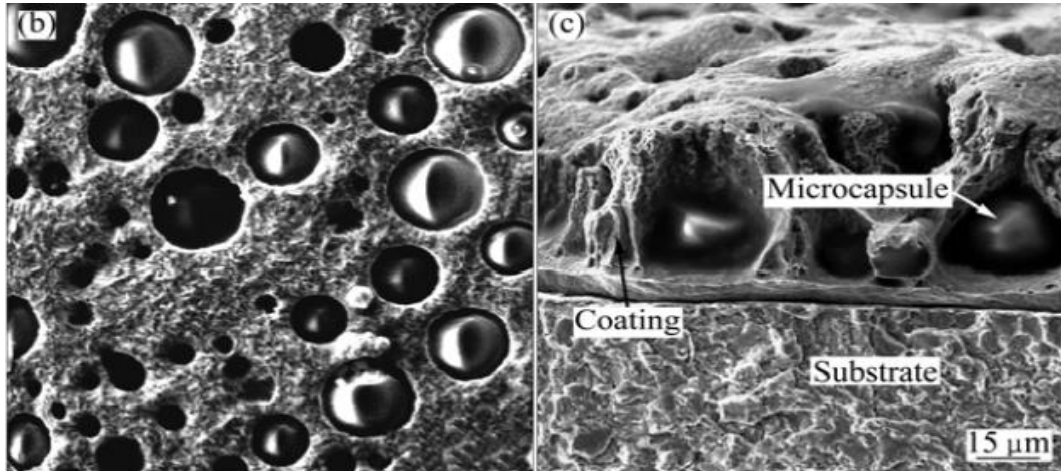


Figure 2.9: SEM images of copper-microcapsule composite showing surface and cross-section [Xu et al. 2011].

Co-deposited secondary particles can be used to create a superhydrophobic surface using two different methods. The first method is to co-deposit fine particles to create a very rough surface, and then coat the hydrophilic material with a low surface energy film creating a very rough, highly hydrophobic coating. The second method is to alter the surface chemistry directly by co-depositing low surface energy particles with no additional surface treatments necessary.

An example of the first method was done by Huang et al. In this work, Ni-TiO₂ nanocomposite was produced using electrodeposition and then modified with a layer of fluoroalkylsilane (FAS-17) to produce superhydrophobic surfaces. The TiO₂ particles in this work were between 15-30 nm in diameter. The addition of nanoparticles influenced the crystal growth, with fine thorn-like shaped crystals observed. This fine crystal structure caused by the addition of 50 g/L of TiO₂ nanoparticles combined with the surface modification using FAS-17 resulted in a superhydrophobic surface displaying a contact angle as high as 174.9° [Huang et al. 2011]. This type of material is highly dependent on the surface modifying film and any damage

to this will cause the underlying hydrophilic material to be exposed, which will greatly reduce the contact angle.

The second method of producing superhydrophobic coatings using electrodeposited composites has been studied using PTFE as a secondary particle. Work by Ibe et al. and Wang et al. have both shown Ni-PTFE composite surfaces that display high contact angles. Ibe et al. used 5 μm diameter particles and produced a coating containing 45 vol% PTFE which resulted in a contact angle of 156° [Ibe et al. 1998]. Wang et al. used smaller sub-micron PTFE particles with an average particle size of 0.3 μm . A maximum of 47.4 vol% PTFE was achieved, displaying a contact angle of 154.9° [Wang et al. 2004]. Figure 2.10 shows SEM image of this coating surface as well as a contact angle image.

Another example of this technique was done by Shrestha et al. where surface-modified SiO_2 was co-deposited with nickel. SiO_2 particles were modified to be hydrophobic by treating them with a functional short-chain siloxane. Composite coatings containing 45 vol% of the hydrophobic SiO_2 displayed a contact angle of 156° [Shrestha et al. 2004]. None of the studies outlined above made mention of the adhesion of the water droplets through tilt angle measurements, contact angle hysteresis or any other techniques. There was also no mention of any grain size measurements for the nickel matrix of these coatings.

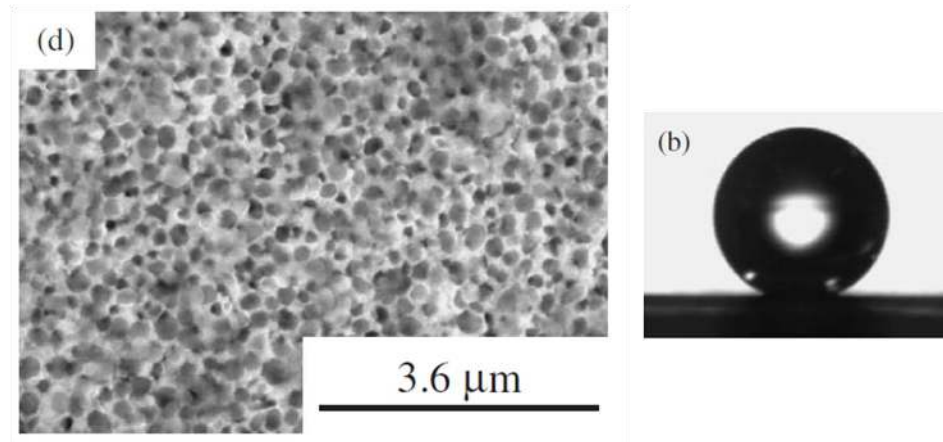


Figure 2.10: SEM image of Ni-PTFE coating containing 47.4 vol% PTFE displaying superhydrophobicity [Wang et al. 2004].

2.3 Nanocrystalline Metals

Nanocrystalline metals can be described as materials that have been produced in a way to possess a very fine structure, with grain sizes 100 nm or less [Kear and Siegel 1992]. Study of these unique materials has brought forth the realization that many different bulk properties of metals are significantly changed when the grain size is reduced down to the nanometer scale. This has led to a great deal of research into the development of nanocrystalline metals for both scientific study and commercialization.

The most significant difference in the structures when comparing nanocrystalline and polycrystalline material is the distribution of the location of atoms. In a polycrystalline material, the vast majority of all atoms are located inside grains at perfect lattice locations. When the grain size decreases, the percentage of atoms located in disordered regions, such as grain boundaries and triple junctions, increases. To mathematically determine the volume fraction of

intercrystalline atoms, grains have been modeled with a 14 sided tetrakaidecahedral shape. From this model, the proportion of intercrystalline material can be calculated for a given grain boundary thickness. The results of this calculation can be seen in Figure 2.11 for a grain boundary thickness of 1 nm [Palumbo et al. 1990]. As the grain size is reduced from 1000 nm to 5 nm, the total volume fraction of the interface increases from less than 1% to over 50% of the material. This drastic change brings about equally drastic changes in some of the properties of the material. Table 2.1 summarizes material properties that have been found to be grain size dependent and grain size independent for fully dense nanocrystalline electrodeposits [Erb 2010]. For the work in this project, the properties of interest are hardness and yield strength and associated properties such as resistance to wear. Nanocrystalline nickel is chosen in the current study as the matrix material in the composite coating to provide mechanical strength.

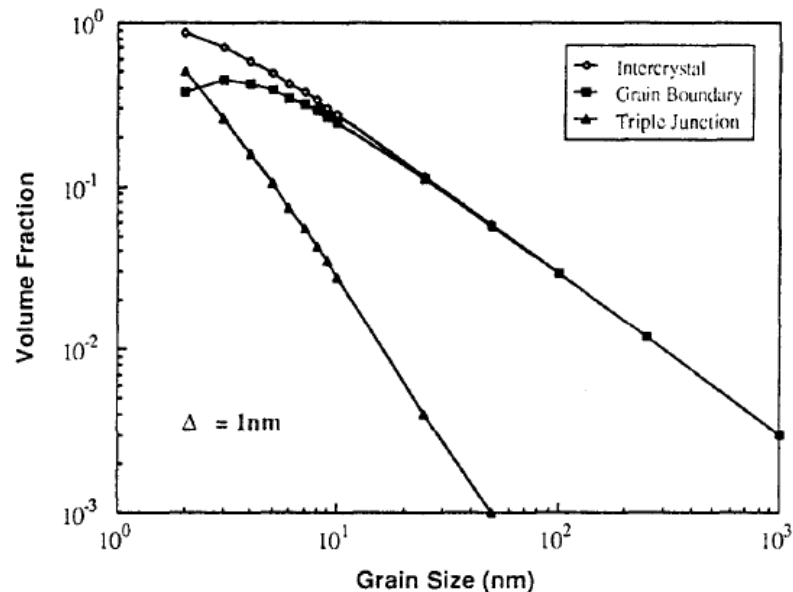


Figure 2.11: Volume fraction of intercrystalline regions as a function of grain size [Palumbo et al. 1990]

Table 2.1: Dependence of grain size on various properties [Erb 2010].

Strong Grain Size Dependence	Weak Grain Size Dependence
Hardness	Young's Modulus
Yield Strength	Fatigue Performance
Tensile Strength	Thermal Expansion
Elongation to Fracture	Specific Heat
Coefficient of Friction	Saturation Magnetization
Abrasive Wear Resistance	Curie Temperature
Adhesive Wear Resistance	Salt Spray Corrosion Resistance
Localized Corrosion	Passivity in Corrosion
Hydrogen Diffusivity	
Electrical Resistivity	
Coercivity	

Synthesis of nanocrystalline materials can be done using several different techniques including: vapour phase processing, liquid-phase processing, solid-state processing, chemical synthesis and electrochemical synthesis. The focus of this work is on synthesis through electrodeposition. Nanocrystalline metals produced using electrodeposition is an area that has been well studied [Erb et al. 2011] and has been shown to be able to produce fully dense material [Haasz et al. 1995].

2.3.1 Synthesis of Nanocrystalline Nickel using Electrodeposition

Electrodeposition is a well established industrial method for producing metal and alloy coatings, thin films or free standing components. The technique is a fairly straight-forward process. The main required components include an electrolyte bath containing metal ions, a power supply, a cathode substrate for metal ion reduction, and an anode material. The basic mechanism for the deposition of metal coating is that the external power source drives the

reduction of metal ions onto the cathode surface. The reactions at the cathode surface, in an acidic electrolyte, can be simplified to:



In this simplified example, a metal ion of valency z is reduced on the cathode surface forming a metal atom while simultaneous reduction of hydrogen ions forms hydrogen gas. The formation of hydrogen gas is an undesired competing reaction that reduces the overall efficiency of the process. The stated cathodic reactions are simplified as in reality intermediate steps can make the mechanism more complex depending on the metal being deposited.

The evolution of the metal matrix on the cathode surface takes place in two steps. First crystals nucleate on the surface in various crystallographic orientations, then these crystals begin to grow through surface diffusion of newly deposited atoms. As plating continues, growth of existing grains and nucleation of new grains compete, and this ultimately determines how fine or coarse the grain structure is in the final deposit. To produce nanocrystalline metals using electrodeposition, the structure evolution must be controlled in a way to promote massive nucleation while minimizing grain growth. This can be done by careful selection of plating parameters [Schlesinger and Paunovic 2010].

One plating parameter that has a direct effect on grain nucleation is current density. A high current density allows for two important effects to occur that helps to promote nucleation. High current density allows for a higher rate of nickel reduction and it also reduces the critical size needed for crystal nucleation, r_c [Erb et al. 2011]. These two effects combined will cause

the rate of nucleation to be much greater than the rate of crystal growth. However, the magnitude that the current density can be raised to is limited when using direct current (DC). When current density becomes very high, the metal ions reduce at a very fast rate and the transport of metal ions from the electrolyte to the cathode surface is the rate determining step [Schlesinger and Paunovic 2010]. The limiting current, I_L , that be used is thus directly related to the diffusion coefficient of the metal ions in solution and is given by the following equation

$$I_L = \frac{zFD}{\delta} C_b \quad (2-8)$$

where z is the number of electrons in the reduction reaction, D is the diffusion coefficient of the metal ions to be deposited, F is the Faraday constant, δ is the diffusion layer thickness and C_b is the concentrations of metal ions in the bulk electrolyte. When the limiting current is exceeded, alternative reactions occur on the cathode surface due to the absence of metal ions such as hydrogen evolution as described in Equation (2-7) [Schlesinger and Paunovic 2010].

To increase the current density past the limiting current to further promote massive nucleation, a method known as pulse plating can be used [El-Sherik and Erb 1995]. Pulse plating is a technique where the current is cycled on and off. Deposition takes place at a peak current, I_{peak} , much higher than the limiting current described for DC plating, but in short intervals. The current is briefly turned off between intervals and it is during this off time that metal ions have time to diffuse and the double layer is replenished without other reactions occurring [Erb et al. 2011].

While the use of pulse plating can allow for very high current densities, and thus very high nucleation rates, the mobility of the metal atoms across the surface must be reduced to prevent grain growth during the electrodeposition process [Choo et al. 1995]. This can be done through the use of organic additives as growth inhibitors. A commonly used additive of this type used in nickel electroplating baths is saccharin ($C_7H_5NO_3S$). As well as preventing surface diffusion of metal ions, saccharin addition in nickel plating lowers the overpotential of nickel ion reduction and blocks crystalline growth which increases nucleation [El-Sherik and Erb 1995].

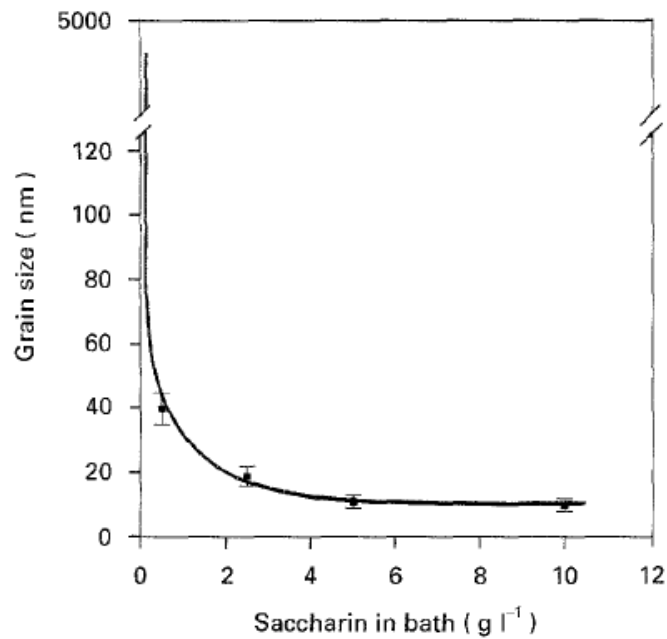


Figure 2.12: Effect of saccharin addition to electroplating bath on the grain size of nickel [El-Sherik and Erb 1995].

El-Sherik and Erb showed the grain size refining effects of saccharin when using pulse plating to produce nickel deposits [El-Sherik and Erb 1995]. In this work, a small amount of saccharin, 0.5 g/L, was sufficient to reduce the grain size from the micrometer range down to 40

nm. Additional saccharin concentration reduced the grain size to 10 nm at a concentration of 5 g/L, but no further decrease in grain size was noted up to 10 g/L of saccharin. The leveling off of grain refining property of saccharin addition is attributed to leveling off of overpotential for nickel reduction and the saturation of adsorption sites for saccharin molecules on the cathode surface [El-Sherik and Erb 1995].

2.3.2 Grain Size Effect on Hardness and Yield Strength

Refining the grain size of polycrystalline metals is an effective and well understood method of increasing both the hardness and strength of a metal. The relationship can be described by the Hall-Petch equation which is valid for both the hardness, H , and yield strength, σ ,

$$H = H_o + kd^{-1/2} \quad (2-9)$$

$$\sigma_y = \sigma_{yo} + k'd^{-1/2} \quad (2-10)$$

where H_o and σ_{yo} are the hardness and yield strength values at very large grain size, d is the grain size of the metal and k and k' are constants. Investigations of the validity of this relationship in nanocrystalline materials have been a large area of interest. El-Sherik et al. completed one of the first studies on the effect of grain size on hardness in nanocrystalline nickel produced by electrodeposition [El-Sherik et al. 1992]. The results of the work are shown in Figure 2.13. Nickel was produced through electrodeposition with grain sizes varying from 100 - 10 nm and compared with polycrystalline nickel with a grain size of 100 μm . The Hall-Petch equation was

shown to be valid for large grained material, however a deviation from the expected hardness was observed at small grain sizes (<25nm).

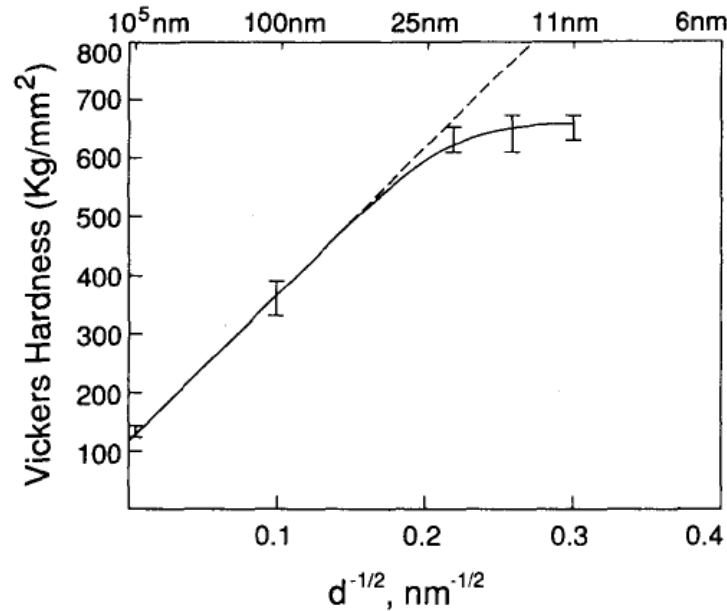


Figure 2.13: Hall-Petch plot for Vickers hardness of electrodeposited nanocrystalline nickel [El-Sherik et al. 1992]

The deviation from the Hall-Petch relationship shows that as the grain size becomes very small, the dislocation hardening mechanism loses effectiveness. To understand the deviation from the Hall-Petch relationship further understanding of the deformation mechanisms in nanocrystalline materials is needed. In conventional coarse grained materials, the dominant mechanism to accommodate plastic deformation is intragranular slip caused by dislocation motion. In this situation the strength-controlling process is the pile-up of dislocations against grain boundaries, where grain size refinement results in an increase in the resistance to plastic flow due to an increase in the number of grain boundaries. However, as grain sizes become very small, into the nanometer range, the operation of Frank-Read sources within a very small grain

(<50 nm) requires extremely high level of shear stress [Dao et al. 2007]. This suggests that traditional intragranular slip is no longer possible as dislocation nucleation within the grains is no longer possible.

The inability of dislocation sources to function at very small grain sizes suggests that alternative deformation mechanisms must play a more significant role, mainly grain boundary assisted deformation. Deformation processes at the grain boundaries include the emission of perfect and partial dislocations from the grain boundary into grains, grain boundary shear and grain boundary rotation [Dao et al. 2007]. This change in the dominating deformation mechanism explains the deviation from the Hall-Petch relationship, as a change in deformation mechanism will result in changing values for k and k' in equations (2-7) and (2-8).

Chapter 3

Experimental Procedures

3 Experimental Procedures

This chapter outlines the experimental procedures used for all sections of the thesis as described in Figure 1.6. This starts with the characterization of the PTFE particles that were used in the plating of the Ni-PTFE composite material. Experimental work for Chapter 4 includes the synthesis procedures for initial composite coatings and characterization of the deposited composites using scanning electron microscopy (SEM), energy-dispersive X-ray spectroscopy (EDX), and contact angle measurements. For the work presented in Chapter 5, which focuses on grain size refinement of nickel, this work includes synthesis of pure nickel coatings containing saccharin, characterization of grain size and texture using XRD and microhardness measurements. Chapter 6, which covers the synthesis of nano-Ni-PTFE composite coatings, uses all of the characterization techniques from the previous two sections with the addition of 3-D surface profilometry to characterize the surface roughness.

3.1 Particle Characterization

Polytetrafluoroethylene (PTFE) powder used in this research project was supplied by AGC Chemicals America, Inc., under the product brand name of Fluon[®] PM FL1710. PTFE is a

fluorocarbon polymer with chemical structure $(C_2F_4)_n$. It is a linear polymer chain where the repeating unit is given by the structural formula shown in Figure 3.1.

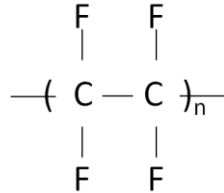


Figure 3.1: Structural formula for PTFE [Callister 2008]

Table 3.1 summarizes the relevant properties of the powder as specified by the manufacturer. Particle type is described as soft submicron particles in clusters implying agglomerations that may be able to be broken up with strong agitation. The particle size is given using two different testing methods, the first method is laser diffraction and it involves low shear forces acting on the clusters meaning breaking up of agglomerations is unlikely. The second particle sizing method was done using a Hegman gauge in a high shear environment where agitation was applied to clusters, breaking up agglomerations.

Table 3.1: Typical properties for Fluon 1710 PTFE micropowder

Property	Typical Values
Particle Type	Soft, round submicron particles in clusters Clusters break-up to smaller size upon mixing
Particle Size – Low Shear (Laser Diffraction)	Average 9 μm D10 <4 μm D90 <17 μm
Particle Size – High Shear (Hegman Gauge)	3 μm
Relative Density	2.2

3.1.1 Scanning Electron Microscopy

SEM images of the as received PTFE powder were taken using a Hitachi S-4500 field emission SEM. Secondary electron images were taken at 1.5kV at a working distance of 5 mm. Image analysis was used to measure the particle size using ImageJ software. To account for non-spherical shape of the particles, measurements of the major and minor axis of the particles were taken and averaged to get an average particle diameter. The PTFE powder as received contains particles at two different scales, large micron-sized particles/agglomerations as well as submicron particles. Average particle size for both the micron sized particles/agglomerations and the submicron particles were measured separately.

3.1.2 Ultrasound-Based Methods

Acoustic techniques are relatively new in the characterization of colloids and have several distinct advantages over traditional techniques for the research presented here. Acoustic methods using ultrasound, allow for characterization of a large range of particle sizes (5 nm - 1000 μm) along with measurements in highly concentrated (up to 50 vol%) solutions [Dukhin and Goetz 2010]. The equipment used to characterize the solutions in this work is the DT-1200 manufactured by Dispersion Technology, Inc. This equipment is able to measure both the particle size and the zeta potential of the PTFE powder when dispersed in aqueous solution.

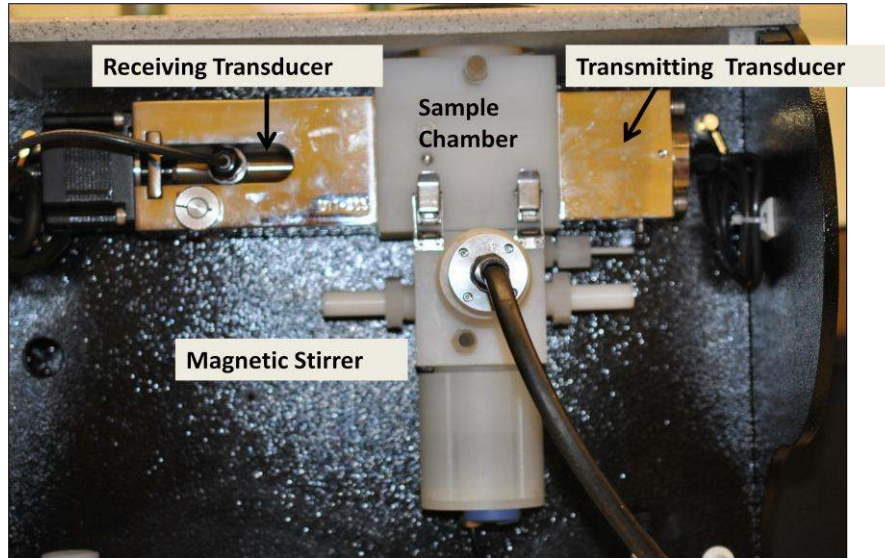


Figure 3.2: DT-1200 close up image of sample chamber.

Particle size distributions (PSD) determined from this instrument are approximations based on the assumption of a modified log normal distribution. An approximate PSD is satisfactory for the research done as an accurate count of individual particle size bins in a histogram is not necessary. Particle size characterization is done by measuring the attenuation of sound waves when passed through a colloidal solution. Ultrasound waves are passed through the sample at different frequencies (1-100 MHz) and the attenuation caused by the particles is recorded. Before measuring a colloidal solution, the electrolyte solution is tested to measure the intrinsic attenuation of the liquid so this is not accounted for when determining particle size. Input parameters that are needed to measure particle size include the density of both the electrolyte and dispersed particles and the weight fraction of particles in the solution. Detailed explanation of attenuation mechanism and the calculation of PSD from the attenuation is included in Appendix 3. The PSD measurements were run three times for each sample to

demonstrate reproducibility. Once the attenuation curves are produced, computer software automatically fits the data to either a unimodal or bimodal log normal PSD based on which has a lower error.

To measure particle size distribution, PTFE particles were first dispersed in deionized water with the aid of cationic surfactant cetyltrimethylammonium bromide (CTAB). The reason for using CTAB as the surfactant will be discussed in section 3.2. CTAB was added to DI water at 60°C and stirred using a magnetic stirrer until dissolved. PTFE powder was then added and strongly agitated until all powder was wet by the solution. The particles were then ultrasonically agitated for an hour in order to break up agglomerates.

Zeta potential measurements were done using the electroacoustic technique. The zeta potential probe, pictured in Figure 3.2, consists of a transmitting and receiving transducer. Acoustic energy is used to cause vibrations in the colloid solution, resulting in particles gaining induced dipole moments [Duhkin and Goetz 2010]. The electric field caused by the sum of the dipole moments is sensed and measured by a gold electrode at the end of the probe. The electric field causes a current to flow into the probe, which is referred to as the colloidal vibration current (CVI). CVI can then be converted into zeta potential given proper parameters. Further explanation is included in Appendix 4.

Calibration is done using a standard which is 10 wt% silica (Ludox TM-50) in 0.01M KCL aqueous solution with a well established and stable zeta potential of -38 mV. The electrolyte is first tested to measure any background signal. This background signal is saved and subsequently subtracted from future measurements to ensure the signal is only coming from the particles. Inputs for measurements include: density of electroplating bath, density of PTFE,

concentration of PTFE particles, and particle size. Since particle size is an input and has significant impact on the conversion from CVI to zeta potential, particle size measurements are required to be run first.

3.2 Synthesis of Composite

PTFE particles were first dispersed in deionized water with the aid of cationic surfactant cetyltrimethylammonium bromide (CTAB). CTAB was chosen based on many previous reports in the literature that have shown the positive influence a cationic surfactant has on the particle co-deposition process, as summarized in section 2.2.2. The CTAB molecule, $(C_{16}H_{33})N(CH_3)_3Br$ (Figure 3.3), consists of a long hydrocarbon chain ($C_{16}H_{33}$) that makes up the hydrophobic tail, with a trimethylammonium ion, $N(CH_3)_3^+$, as the hydrophilic head group. This is balanced with a bromine ion, Br^- , to form an electrically neutral molecule. When in solution, the CTA^+ dissociates from the Br^- ion resulting in the charged CTA^+ surfactant molecule.

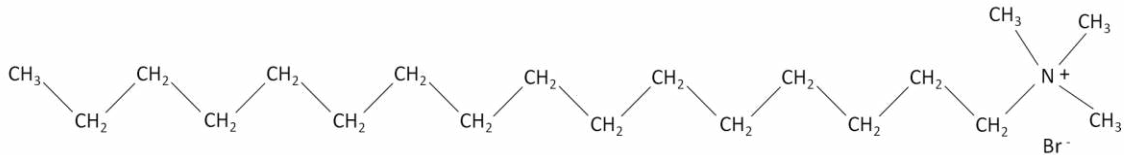


Figure 3.3: Structural formula for CTAB

CTAB was added to DI water at 60°C and stirred using a magnetic stirrer until dissolved. PTFE powder was then added and strongly agitated until all powder was wet by the solution. The particles were then ultrasonically agitated for an hour in order to fully break up all agglomerates.

PTFE concentration in the bath varied from 10-40 g/L, with the ratio of CTAB to PTFE powder kept constant at 0.033g CTAB/g PTFE. This ratio of surfactant to PTFE particles was chosen through trial and error as it was found to effectively disperse the particles in solution as well as reduce pitting effects during electrodeposition. Chemicals used in a Watt's type nickel electroplating bath were then added to the PTFE-surfactant solution. The bath composition used for all samples is listed in Table 3.2.

Copper coupons were used as cathodes. Coupons were 2 cm x 2 cm with a thickness of 1.56 mm. The copper was polished using 1200 grit abrasive paper and ultrasonically cleaned in ethanol. Plating was done on only the front side of the copper with non-conductive electroplating tape used to cover the back. Dissolvable Inco nickel R-Rounds contained in a dimensionally stable titanium basket were used as anode material. During electrodeposition, the anode and cathode were placed vertically, directly across from one another with a distance of 3 cm between them. A magnetic stirrer was used to agitate the bath and maintain particle dispersion. Plating conditions were kept constant for all samples and are listed in Table 3.2. After completion of plating, samples were ultrasonically cleaned in ethanol for 5 minutes. The thickness and mass of each coupon was measured before and after plating to obtain the thickness and mass of the electroplated coatings.

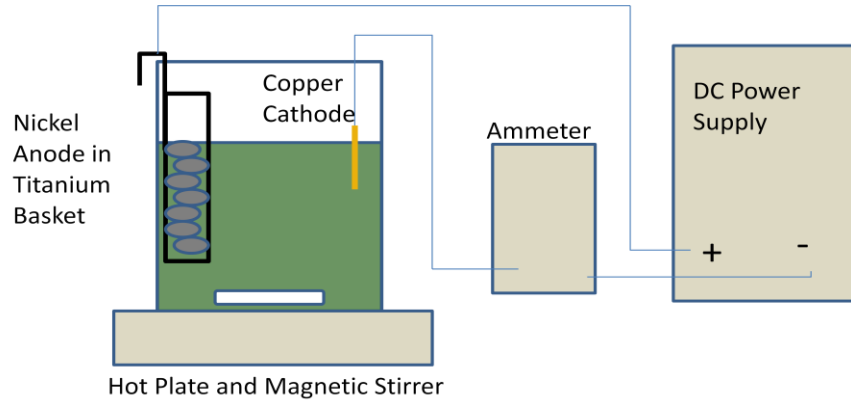


Figure 3.4: Schematic diagram showing the electrodeposition setup used.

Table 3.2: Electroplating bath composition and parameters

Component	Concentration (g/L)	Parameter	Value
NiSO ₄ x 6H ₂ O	300	Current Density	100 mA/cm ²
NiCl ₂ x 6H ₂ O	45	Temperature	60°C
H ₃ BO ₃	45	pH	3.25-3.5
PTFE	0-40	Time	30 min
CTAB	0.033 (gCTAB/gPTFE)	Agitation	400 RPM
		Thickness	60-80 μm

3.3 Electrodeposit Characterization

3.3.1 SEM and Image Analysis

Scanning electron microscopy was used to observe the surface of the composite coatings to make qualitative observations of the distribution of PTFE particles on the coating surface, surface morphology of the nickel matrix, and the Ni-PTFE interface. A Hitachi S-4500 field

emission SEM was used to take secondary electron images at high magnification. Images were taken at 1.5 kV to reduce charging, at a working distance of 5 mm. A Hitachi S-3500 was used to take images using backscattered electrons. Images were taken at 20 kV and a working distance of 10 mm with a variable pressure of 50Pa in the sample chamber which reduced charging effects. These images show a very large contrast between nickel and PTFE due to atomic number contrast.

Cross-sectional images of composite samples were taken to observe PTFE particle distributions throughout the deposit. Preparation for cross-sectional images involved cutting the samples using a diamond blade, and then mounting the sample in epoxy resin. The mounted cross-section was ground and polished to remove areas of large deformation caused by cutting.

The PTFE content in the composite coatings was determined using both image analysis as well as energy-dispersive X-ray spectroscopy (EDX). SEM images at x2500 magnification from three different representative areas of each sample were taken and analyzed using ImageJ. The high contrast between the PTFE particles and surrounding nickel matrix made it possible to threshold the images and use the built in ImageJ function to measure the area fractions of PTFE particles.

3.3.2 Energy Dispersive X-Ray Spectroscopy

To further quantify the composition of Ni-PTFE coatings, energy dispersive x-ray spectroscopy (EDX) was done on representative samples. The Hitachi S-3500 SEM was used at 20kV, working distance of 10 mm and a chamber pressure of 50 Pa. EDX scans were completed at x500 magnification, in order to capture a large area. The amount of nickel and fluorine, by

weight, was quantified. The weight percent fluorine was converted to weight percent PTFE under the assumption of 2:1 fluorine-to-carbon ratio based on the molecular formula for PTFE, C_2F_4 . The composition in weight percentage was then converted to volume percentage. Sample calculations are provided in Appendix 1. EDX scans were done at three distinct areas for each sample and were used to obtain an average composition for the coating.

3.3.3 Contact Angle Measurements

To measure the hydrophobicity of composite coatings, the static contact angle of 5 μ l water droplets were measured. A sample stage was set up and leveled to ensure the coating surface was flat during measurements. A Nikon D3000 digital camera with a macro lens attached was mounted on a tripod and adjusted so that the camera was at the same level of the stage and with the sample in the middle of the frame. Samples were placed flat on a surface directly in line with the camera lens. 5 μ L droplets of DI water were placed on the samples using a micropipette. The self-timer function was used to ensure stability while the pictures were being taken. Images were analyzed using ImageJ, where the outside angle of the drop, as shown in Figure 3.5 was measured. The outside angle was subtracted from 180° to obtain the contact angle. The average contact angle of five droplets across the surface of the coating was used to determine the wetting properties of each sample.

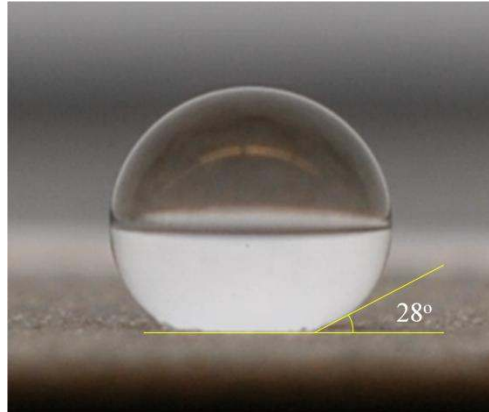


Figure 3.5: Example of contact angle measurement using ImageJ.

3.3.4 X-Ray Diffraction

X-ray diffraction patterns of the nickel coatings as well as Ni-PTFE composite coatings were recorded using a Rigaku MiniFlex X-ray diffraction instrument which uses a Co-K α source with a wavelength, $\lambda = 0.179$ nm. XRD was done using a standard θ - 2θ setup at a power of 30kV, 15mA. Scans covered the angular 2θ range from 40° - 140° . The purpose of using X-ray diffraction for this work was to characterize the nickel matrix in terms of crystallographic orientation and grain size.

Peak broadening in X-ray diffraction occurs due to a combination of instrumental contribution as well as contributions from the crystal structure of the material. When the grain size of a metal is very small, below 100 nm, significant broadening of diffraction lines occurs [Cullity and Stock 2001]. This effect is due to the limited amount of diffraction planes at this small grain size, preventing complete destructive interference when the angle deviates slightly from the Bragg angle. At smaller grain sizes, diffracted signals are able to be measured further

away from the Bragg angle. The contribution of peak broadening associated with crystal size can be described using the Scherrer formula:

$$d = \frac{0.9\lambda}{B \cos \theta_B} \quad (3-1)$$

where d is the grain size, B is the broadening of the diffraction line caused by grain size reduction measured at full width at half maximum measured in radians, λ is the wavelength of the incident X-ray beam, and θ_B is the Bragg angle. The line broadening due to small grains needs to be isolated from instrumental broadening. This is done by measuring the diffraction pattern of a large grained polycrystalline nickel standard. This value is saved and then the broadening due to grain size effects is isolated using the following equation

$$B^2 = B_M^2 - B_S^2 \quad (3-2)$$

where B_M is the measured broadening from the diffraction pattern, B_S is the broadening measured for the standard and B is the line broadening caused by grain size effects [Cullity and Stock 2001]. The measured value used for B_S is 0.1° . Grain size measurements are done automatically using software MDI JADE version 5.0.26 to analyze the XRD patterns.

Characterization of any texture present in the samples was done by determining the orientation index, I_{hkl} . The orientation index is defined as the fractional intensity of a particular set of planes to its fractional intensity in the same material with a random structure [Willson and Rogers 1964]. The relative peak intensities for a random nickel structure were calculated and compared to measure relative intensity of the electrodeposited nickel and Ni-PTFE samples using the following relation,

$$I_{hkl} = \frac{\left(\frac{i_{hkl}}{\sum i}\right)_e}{\left(\frac{i_{hkl}}{\sum i}\right)_r} \quad (3-3)$$

where i_{hkl} is the intensity of the diffraction line of a specific plane, $\sum i$ is the sum of the intensities of all the diffraction lines, e is the value for each line measured from electrodeposited samples and r is the corresponding value calculated for a random sample. The orientation indices were calculated for the diffraction peaks corresponding to the {111}, {200}, {220}, {311}, and {222} planes. If all orientation indices are equal to 1 then a random structure exists, whereas an orientation index larger than one for any peak indicates preferential orientation of that plane with respect to the surface of the sample.

3.3.5 Vicker's Microhardness

Characterizing the strength of the electrodeposited nickel samples is difficult due to the geometry of the samples produced. Limited thickness of the coatings prevents the use of tensile test methods and bending tests. For this reason, the property that was measured to characterize the mechanical characteristics of the material produced is hardness. In particular, Vicker's microhardness is the test method best suitable for this purpose. The samples were prepared to comply with ASTM standard E384-11e1, Standard Test Method for Knoop and Vickers Hardness of Materials [ASTM Standard E384 2011e1]. As described in the standard, samples were polished to a flat surface to ensure indentations are clearly defined. According to the ASTM standard the thickness of the sample is required to be at least 10 times the indentation depth to make certain the copper substrate does not affect the measurements. Indentation depth for each sample can be calculated using the measured length of the indentation diagonal and the

standardized indenter geometry specified in the ASTM standard. Five indentations were made on each sample using a 50 g load and the values were averaged. Indentation depths were calculated and confirmed to be at least $1/10^{\text{th}}$ the measured sample thickness.

3.3.6 Surface Profilometry

Surface roughness has a significant impact on the contact angle of a surface, as seen in the Wenzel and Cassie-Baxter models (equations (2-2) and (2-3) in Chapter 2.1.2). To investigate the surface roughness of the samples in this work, surface profilometry analysis was used. A stylus profiler (KLA-Tencor P16+) was used to do 3D mapping. To map out a 3D area, multiple line scans were recorded with 10 μm spacing between each scan. 50 line scans each 500 μm long were measured resulting in a 3D scan of a 500 μm x 500 μm area. Built in software automatically leveled the scans to remove effects of sloped surfaces. Raw data of the x,y,z locations of the profilometer stylus was exported into MATLAB and 2D colour maps were created using the mesh function. Line scans were also plotted using MATLAB.

Chapter 4

Co-Deposition of Ni-PTFE Composite

4 Co-deposition of Ni-PTFE Composite

Electrodeposition has been shown to be a simple, cost effective method of preparing metal matrix composite coatings. As shown in section 2.2.3, a wide range of particles can be used to enhance certain properties of the metal matrix as well as impart additional functional properties to the coating surface. In this section, the results of co-deposition of PTFE particles within a nickel matrix are presented. The as-received PTFE particles used in the experiments were first characterized in powder form and when dispersed in a solution of DI water and surfactant (CTAB). The relationship between particle concentration in the electroplating bath and the amount of PTFE co-deposited in a Watt's plating bath (Table 3.2) was then determined. SEM work was done to characterize the composite coatings. Finally the effect of changing the coatings wetting behaviour through the addition of PTFE was observed by measuring the contact angle as described in section 3.3.3.

4.1 Particle Characterization

4.1.1 Particle Size

As-received PTFE particles were characterized using both SEM imaging and acoustic particle size techniques. Figure 4.1 shows examples of SEM images at different magnifications of the PTFE powder. From the SEM images it is clear that there are many micron scale agglomerates of round submicron-sized particles. Figure 4.1 B shows a large micron-sized particle that appears to be quite compact compared to the loose agglomerate shown in Figure 4.1 C. There are many large solid particles observed between 1 and 10 microns in size. Digital analysis of the images was done to separately measure the larger particles and agglomerates as well as the submicron particles. The average size for micron scale particles/agglomerations was $6.1 \pm 2.2 \mu\text{m}$, while submicron average particle size was $0.28 \pm 0.06 \mu\text{m}$. Histograms of the measured particle size distributions are shown in Figure 4.2. The submicron particle size distribution is determined from measurement of 100 particles where the micrometer scale particles size distribution is from a sample of 50 particles.

Examples of the particle size distributions acquired from acoustic particle size measurements are shown in Figure 4.3. Figure 4.3 A is a cumulative particle size distribution on a volume basis. This can be shown as a density particle size distribution as seen in Figure 4.3 B, where the values on the y axis are equal to the slope of the cumulative plot at the same particle diameter. Three measurements of the same sample are shown to demonstrate reproducibility, the average of the three measurements were used for the median values given.

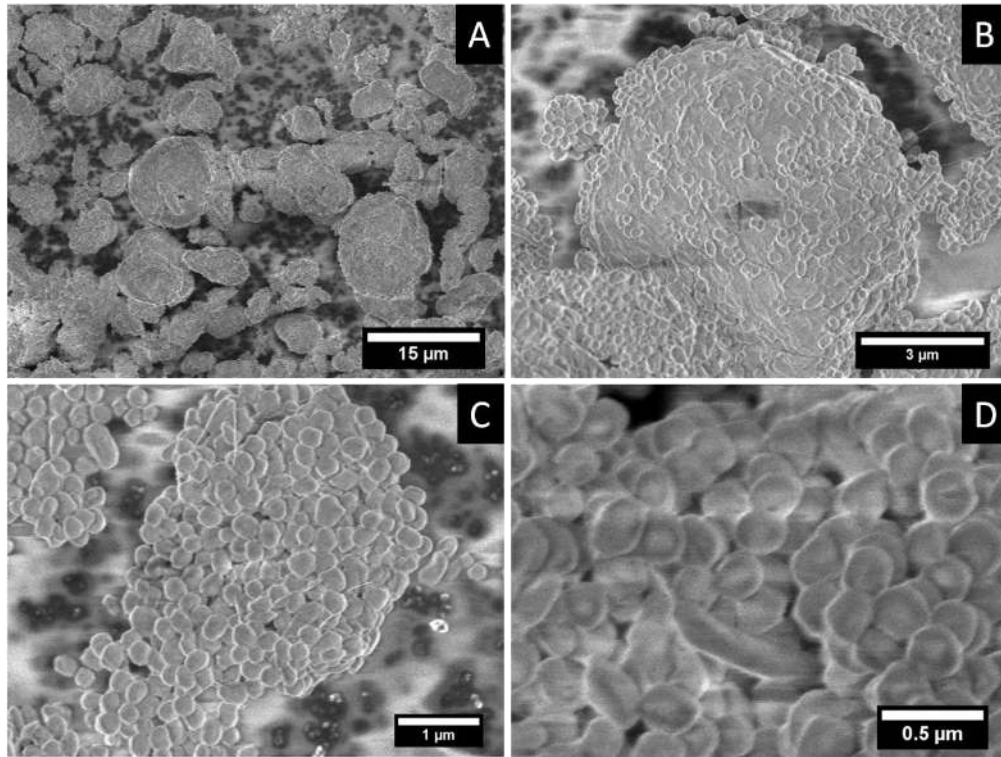


Figure 4.1: PTFE particles at A) x1,500 B) x10,000, large single particle C) x20,000, agglomeration of submicron particles D) x50,000 submicron particles

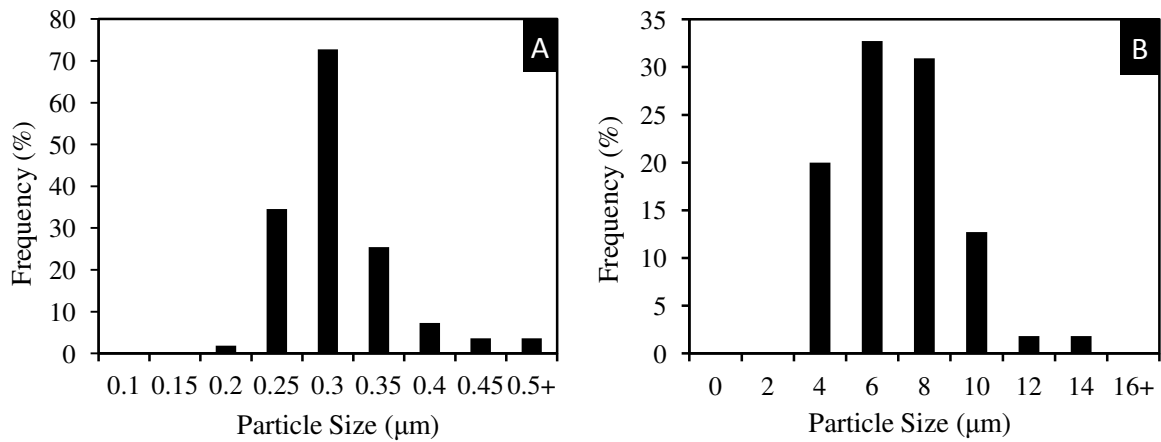


Figure 4.2: Particle size distributions for A) submicron particles (as seen in Figure 4.1 D) and B) micrometer scale particles and agglomerates (as seen in Figure 4.1 A and B)

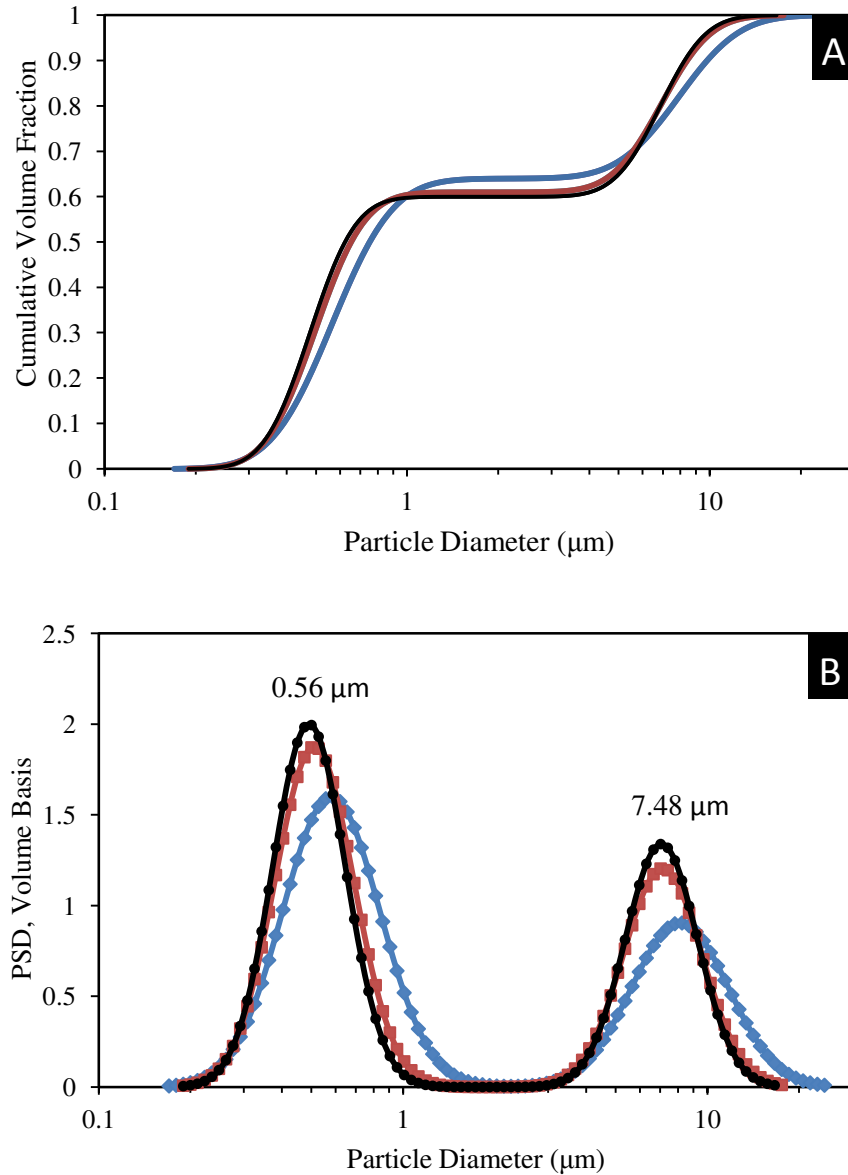


Figure 4.3: Particle size distribution of PTFE particles in solution of DI water and surfactant CTAB. Three results of the same solution are provided to demonstrate repeatability. A) Cumulative PSD on a volume basis B) density PSD

The DT-1200 software automatically fits the attenuation data to show a bimodal distribution. The distribution shows peaks in the micron and submicron range. The peak in the

micron range has a median value of 7.48 μm while the submicron peak has a median of 0.56 μm . The manufacturer's specifications, shown in Table 3.1, describe the particle type as soft, round submicron particles in clusters which is what was observed during SEM investigation. It was also noted by the manufacturer that clusters of particles break up upon mixing. The bimodal distribution, with a submicron peak, indicates that many of the clusters are indeed broken up with the use of a magnetic stirrer, ultrasonic agitation and surfactants.

From the cumulative plots, Figure 4.3 A, it is observed that 60% of the particles in the solution, by volume, have a diameter of less than 1 μm . The plateau in the distribution past this point suggests that there are very few agglomerations or solid particles between 1-4 μm . The distribution further shows that about 40% of the particles fall in the range of 4-15 μm . This is in good agreement with the measurements done using SEM images, shown in Figure 4.2 B, where no large agglomerates/particles were measured below 4 μm . The maximum particle size measured in solution is between 10-20 μm , which once again agrees with SEM observations shown in Figure 4.2 B where very few particles greater than 10 μm were measured.

When the median values are compared to the measured values from SEM work, it is observed that in solution the particle size at both scales is slightly larger. This PSD determined using acoustics suggests that the agglomerates of submicron particles are not completely breaking up in solution. Acoustic measurements take place within the sample chamber shown in Figure 3.2, where agitation is provided by magnetic stirring using a small motor and stir bar. The agitation is significantly stronger during the electrodeposition process, which may result in further break up of agglomerates.

4.1.2 Zeta Potential

Zeta potential results for PTFE particles in CTAB solution with varying ionic concentration are shown in Table 4.1. The components of the electroplating bath were incrementally added to the dispersion in the same ratio as used in the Watt's type bath described in Table 3.2. A significant drop in zeta potential is noted when the ion concentration reaches 0.1 M and becomes very low at 1.85 M, the concentration used in the electrolyte bath. The slight increase from 1M to 1.85M is likely due to background noise, as the input signal is extremely low for these samples. However, even though the zeta potential is very low for PTFE particles in Watt's bath, the PTFE particles appear well dispersed in the electroplating bath. The stability of the particles in the bath cannot be explained by strong electrostatic repulsion and therefore the lack of agglomerations is likely due to a combination of steric repulsion due to the long chain of the CTAB molecule as well as mechanical agitation of the bath through the use of a magnetic stirrer.

Table 4.1: Zeta potential at different ion concentrations

Bath Concentration*	Zeta Potential (mV)
0 M (CTAB only)	+39
0.01M (2.1 g/L)	+27
0.1M (21 g/L)	+14
1M (210 g/L)	+1
1.85M (390 g/L) Watt's Bath	+2

*Bath contains all components of Watt's electroplating bath in same proportions as specified in Table 3.2

The trend that there is a decrease in zeta potential with increasing ionic concentration is in agreement with findings in various other investigations [Dukhin et al. 2005, Arai and Kato 2013, Simunkova et al 2009]. Models of electric double layers predict that at high ionic strength (>1.0 M), the high concentrations of counterions causes the double layer to collapse very close to the particle surface greatly reducing the zeta potential [Duhkin et al. 2005].

The relationship between zeta potential and the co-deposition mechanisms is not fully understood. There have been a few papers reporting a large, positive zeta potential (+20 mV and above) for PTFE in electroless nickel plating solutions [Hu et al. 1997, Ger and Hwang 2002] however, these electroless nickel baths have a much lower ionic strength, consisting of ~ 30 g/L of NiSO_4 compared to 300g/L used in Watt's bath. A few studies have measured substantial zeta potential for particles in nickel electroplating baths [Omar and El Morsi 2009, Chen et al. 2006], however this was not observed in this study. Although the magnitude of the zeta potential is suppressed in the high ionic concentration environment of a Watt's bath, the positive values measured at all concentrations indicates that the cationic surfactant CTAB is in fact adsorbing on the surface of PTFE particles thus promoting positive charge on the surface. In the next section it is shown that co-deposition of the PTFE particles is readily accomplished despite the low zeta potential measurements.

Similar results have been previously reported. Arai and Kato studied the mechanism of co-deposition of multi-walled CNT as well as carbon black particles with copper [Arai and Kato 2013]. In this study the zeta potential of both CNT and carbon black had a very low magnitude of only a few millivolts, when dispersed in the copper plating bath with the addition of polyacrylic acid (PA5000) as a dispersant. Despite the low zeta potential, co-deposition of CNT

and carbon black was achieved. It was determined that the stability of the bath was therefore provided by a steric effect from the polymer chains and not electrostatic forces. Electrophoresis of particles was also ruled out as a significant factor in co-deposition mechanism due to low zeta potential measurements [Arai and Kato 2013].

Simunkova et al. studied the effect of zeta potential on the electrodeposition of nickel ZrO₂ composites [Simunkova et al 2009]. The same equipment as in the present research, DT-1200 by Dispersion Technology, Inc, was used to measure the zeta potential of ZrO₂ in both water and in Watt's bath. A very similar trend to the current work was observed where the zeta potential of the ZrO₂ particles was much lower when measured in Watt's bath compared to water (12.7 mV in water ,1.4 mV in Watt's bath). Co-deposition of up to 13.7 vol% ZrO₂ was accomplished despite the very low magnitude zeta potential [Simunkova et al 2009].

The low zeta potential of the particles in solution is likely due to a high concentration of negative ions (Cl⁻, SO₄²⁻) screening the positive charge associated with the PTFE particles surrounded by CTA⁺ molecules. When the particles are transported very close to the cathode surface through agitation of the bath, Gugliemli's model predicts that the negative charge at the cathode surface repels the negative counter ions, exposing the positive charge of the particle. This would allow for strong electrostatic adsorption between the surfactant encased particle and the cathode surface. This strong adsorption is necessary for the particle to remain fixed to the cathode until nickel ions reduce around the particle permanently embedding it.

4.2 Effect of Particle Concentration on Co-deposition

Composite coatings were produced using the Watts bath composition shown in Table 3.2 with constant plating variables such as current density, pH, temperature and stirring rate. In this series of experiments, the only variable was the concentration of PTFE in the plating bath which ranged from 5-40 g/L.

Examples of SEM images, taken using backscattered electrons, of the composite coating containing 69 vol% PTFE are shown in Figure 4.4. PTFE particles are seen across the entire surface. The coverage however, is not uniform as the distribution of the larger, micron sized particles varies across the surface. There are distinct areas where there is a much lower concentration of large PTFE particles, as seen in the upper left portion of Figure 4.4 A. Submicron particles appear to be evenly distributed in between the large particles throughout the surface allowing for very high packing of PTFE in the composite. SEM figure of all other samples are included in Appendix 2.

Figure 4.5 A shows a cross sectional image of a composite coating containing 61 vol% PTFE. The copper substrate used as the cathode is seen on the right hand side of the image, with the composite coating in the middle of the image and the epoxy used to mount the sample showing on the left hand side. The dark areas in the coating are PTFE particles or voids from particles that have been pulled out during polishing. The image shows the presence of PTFE particles throughout the entire coating from the substrate to the surface. Figure 4.5 B shows a high magnification image of the interface between copper and Ni-PTFE where a high concentration of PTFE particles is observed. There is no noticeable concentration gradient of

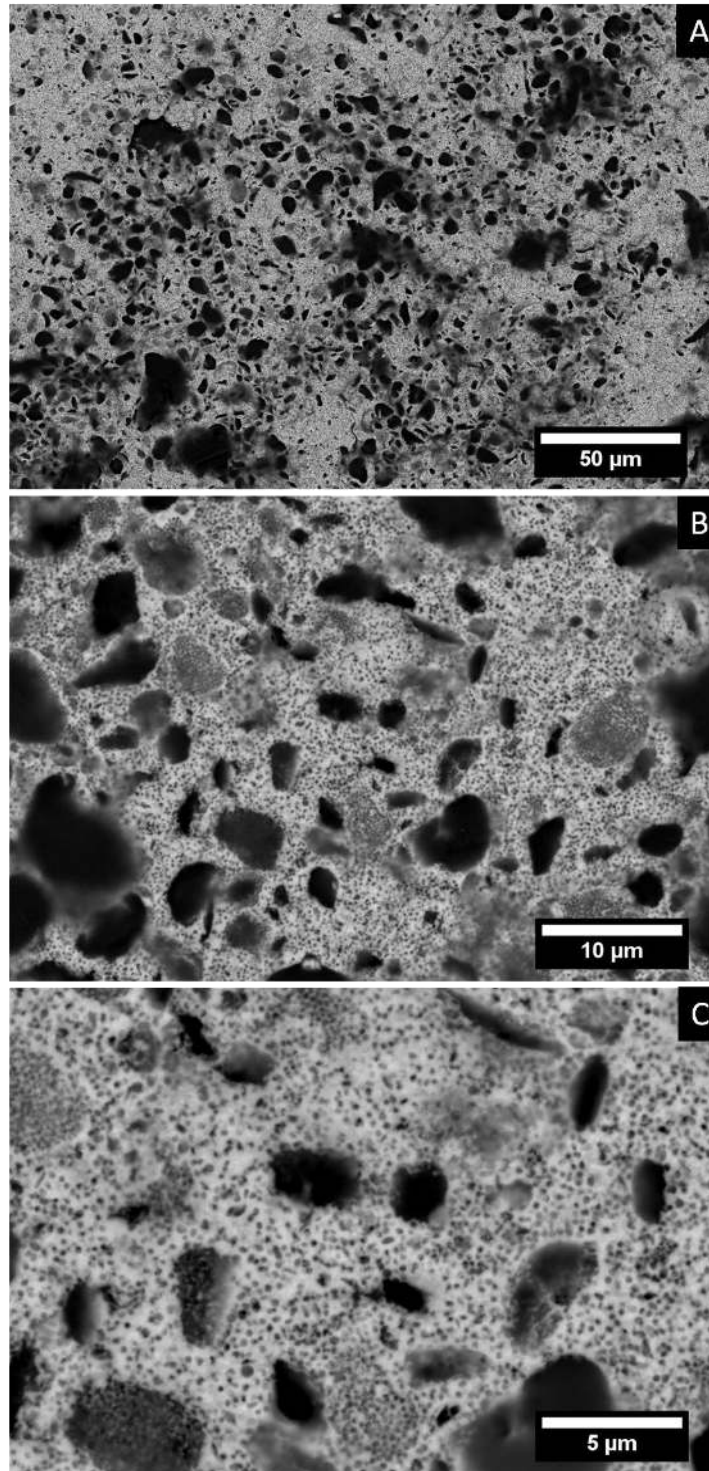


Figure 4.4: SEM images of composite coating containing 69 vol% PTFE using backscattered electrons. A) x500 magnification showing uneven distribution of micron scale particles B) x2,500 magnification showing submicron particles evenly distributed between larger particles C) x5,000 magnification

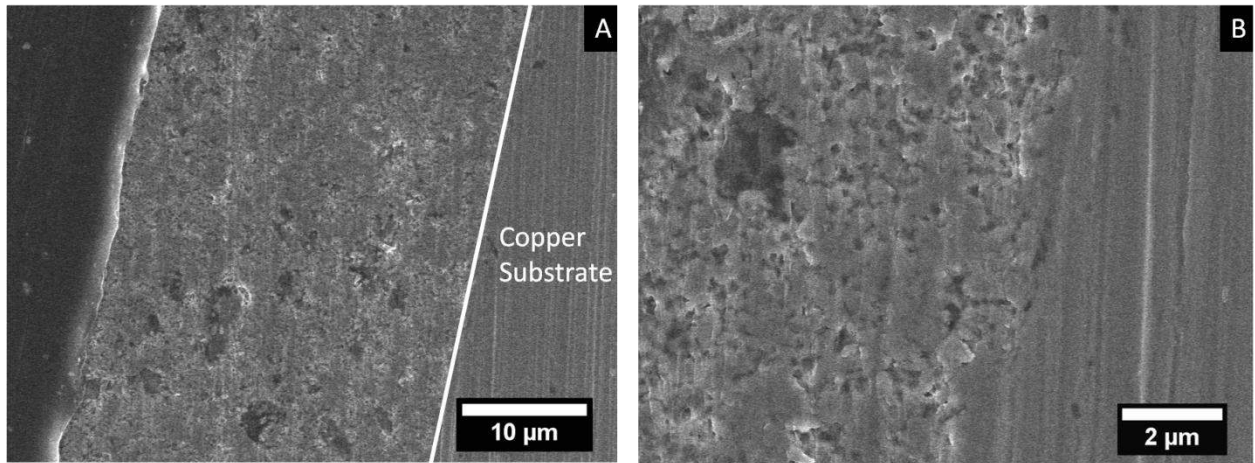


Figure 4.5: Cross section images of Ni-PTFE coating containing 61 vol% PTFE, dark areas show areas where PTFE particles have been embedded in coating. A) x2,500 magnification, the white line in highlights the interface between coating and copper substrate B) x10,000 magnification

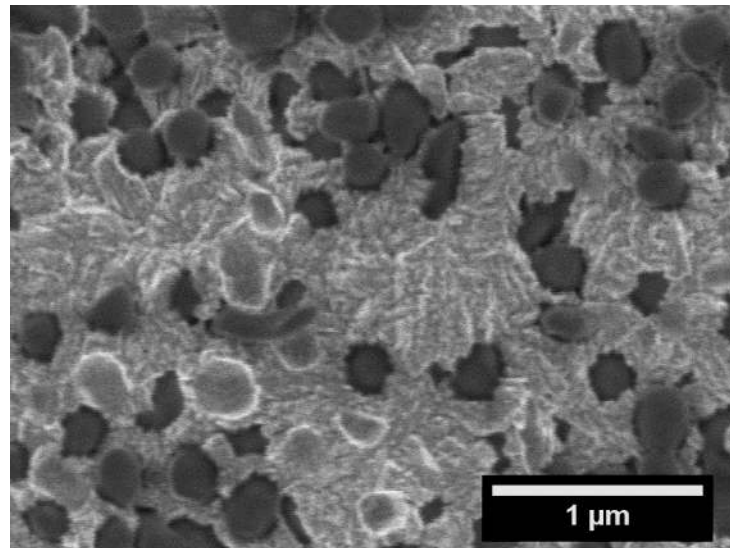


Figure 4.6: High magnification image of nickel matrix with embedded PTFE particles exposed on the surface

PTFE particles throughout the thickness, indicating consistent PTFE inclusion rate during the entire plating process. Additional SEM images showing the even distribution of PTFE particles throughout the thickness are included in Appendix 2. Fracture surfaces are shown from Ni-PTFE coatings electrodeposited under the same conditions as in the current work. These images are results of work done by Andreas Klingler [Klingler 2014].

Higher magnification SEM images of the coating surface provide insight into the nickel matrix as well as the interface between the PTFE particles and the nickel. In Figure 4.6, the nickel matrix can be clearly seen growing around the PTFE particles, fully embedding the particles. The nickel also appears to have a coarse grain structure.

The amount of co-deposited PTFE particles in the composite is strongly related to the concentration of PTFE particles in the electroplating bath, which is shown in Table 4.2. Figure 4.7 displays PTFE content of the deposits in vol% PTFE, as determined by EDX as well as image analysis using ImageJ. Both methods of determining PTFE content display agreement in the overall trend; however the EDX results generally show a higher amount of PTFE incorporation. EDX scans were done at lower magnification (500x) than image analysis (2,500x), encompassing a larger area. Moreover, EDX was done at an accelerating voltage of 20 kV at which the beam will penetrate into the surface producing a large interaction volume. For this reason, the EDX scans are likely more representative of the coating composition as more volume is taken into account. The amount of co-deposited PTFE ranges from 40 vol%, determined by EDX, at a concentration of 5g/L to a maximum value of 69 vol% when a concentration of 30 g/L is used. A slight decrease in PTFE incorporation is observed at 40 g/L. This agrees directionally with the literature, where the maximum amount of PTFE incorporated

into a nickel matrix was found at 25 g/L and remained constant with further PTFE addition [Wang 2004].

Table 4.2: PTFE content in deposit with varying PTFE concentration in plating bath

PTFE Concentration (g/L)	Amount of PTFE in deposit (vol%)	
	Image Analysis	EDX
0	0	0
5	33 ± 4	41 ± 3
10	48 ± 9	45 ± 7
20	53 ± 5	58 ± 1
30	60 ± 4	69 ± 4
40	55 ± 4	63 ± 6

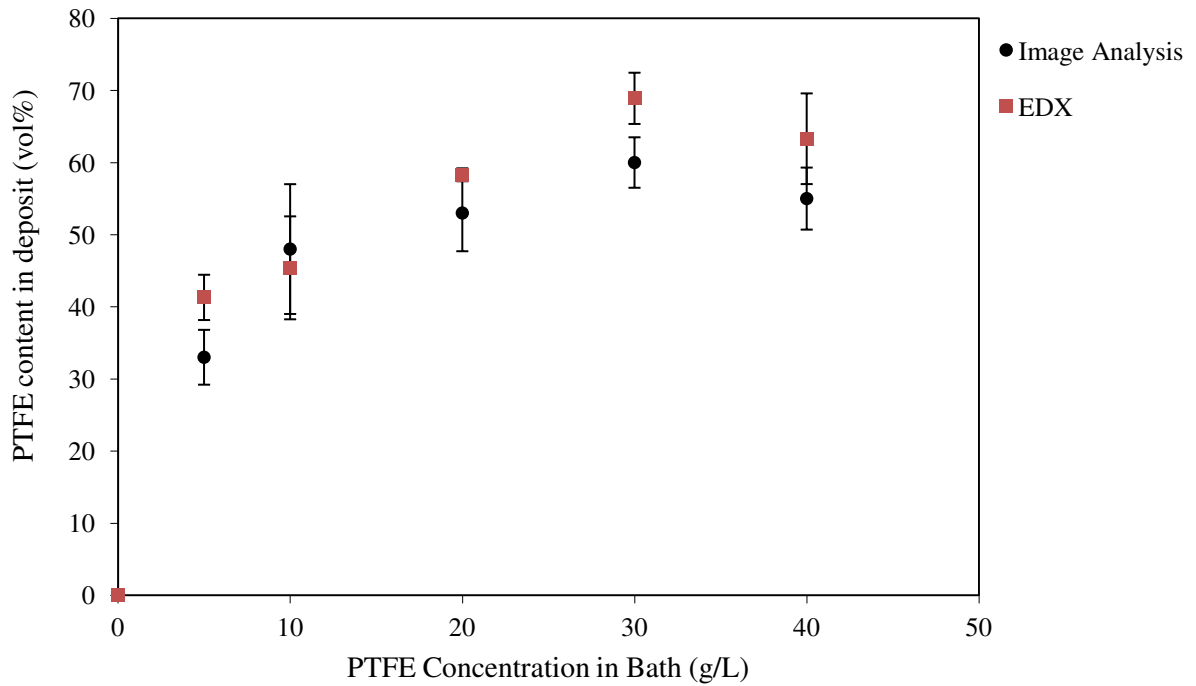


Figure 4.7: PTFE incorporation in coatings versus PTFE concentration in the plating bath. Results of both image analysis and EDX are provided.

PTFE co-deposition is enhanced with the increase in concentration in the bath, due to an increase of particles transported to the cathode surface [Guglielmi 1972]. The leveling out effect is due to a maximum amount of particle flux achieved. The slight decrease in PTFE content in the sample containing 40 g/L PTFE may be due to particle agglomeration occurring. Very high particle concentrations will result in increased collisions of particles and higher chance of agglomerate formation. This effect has been observed in previous work with electrodeposition of Ni-PTFE [Hamid and Omar 1999, Ramesh Bapu and Mohan 1995].

4.3 Effect of PTFE on Wetting Properties

The addition of PTFE particles to the nickel matrix has a significant effect on the wetting properties of the material. The change in contact angle of DI water as a function of the amount of co-deposited PTFE, as per EDX, can be seen in Table 4.3 and Figure 4.8. The low surface energy of PTFE, along with increased surface roughness that is imposed by the particle incorporation, work together to drastically increase the wetting angle when the PTFE content rises above 50 vol%. The maximum average wetting angle observed was $152 \pm 8^\circ$. The wetting angle achieved is similar to results from previous studies of electrodeposited Ni-PTFE coatings where Ibe et al. reported a maximum contact angle of 156° with 45 vol% PTFE and Wang et al. achieved a contact angle of 154.9° with 47.4 vol% PTFE in the coating [Ibe et al. 1998, Wang et al. 2004]. Figure 4.9 shows that for samples containing 41 - 69 vol% PTFE, a linear relationship exists between the amount of PTFE deposited in the coating and the wetting angle.

At PTFE concentration of 40 g/L in the bath, the coating became very brittle and small cracks were visible throughout the surface. The presence of the cracks will have a large impact

on the contact angle, as seen in Table 4.3, and for this reason the contact angle of this sample was not included in Figure 4.9. The brittle coating is likely caused by the CTAB concentration being too high in the bath. During trial and error testing of nickel electrodeposition, it was observed that too high of a CTAB concentration resulted in a highly stressed and therefore brittle deposit with many cracks across the surface. The ratio of $0.033 \text{g}_{\text{CTAB}}/\text{g}_{\text{PTFE}}$ was determined through trial and error to produce good quality coatings when 30 g/L of PTFE was used. This ratio was kept constant to maintain consistency in the electroplating bath composition and was effective for all samples except for when 40 g/L of PTFE and 1.32 g/L of CTAB are added.

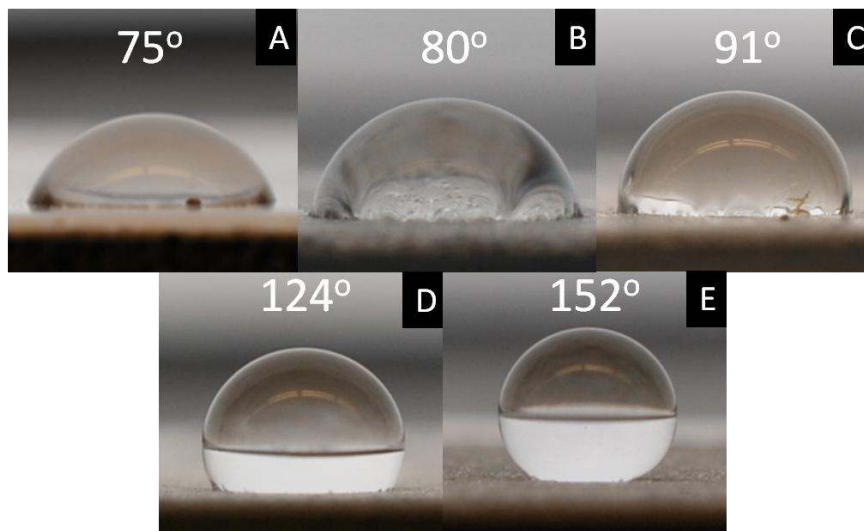


Figure 4.8: Contact angles for composite coatings with different PTFE content. A) 0vol% PTFE B) 41 vol% PTFE C) 45 vol% PTFE D) 58 vol% PTFE E) 69 vol% PTFE

Table 4.3: Wetting properties of Ni-PTFE coatings

PTFE Concentration (g/L)	PTFE Content* (vol%)	Contact Angle (°)
0	0	75 ± 10
5	41 ± 3	80 ± 6
10	45 ± 7	91 ± 1
20	58 ± 1	124 ± 4
30	69 ± 4	152 ± 3
40	63 ± 6	126 ± 8

*PTFE content as determined using EDX

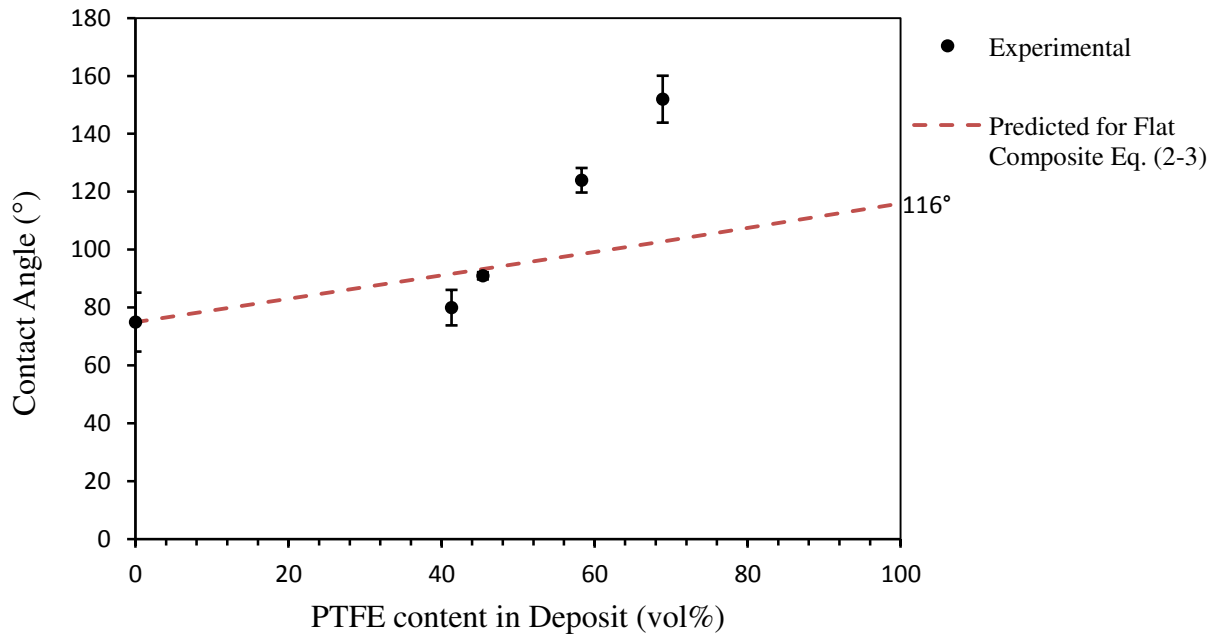


Figure 4.9: Contact angle with varying amount of PTFE. PTFE incorporation determined through EDX.

The addition of 69 vol% PTFE to the nickel surface resulted in a contact angle of 152°, significantly higher than the contact angle of smooth PTFE which is 116° [Busscher et al 1983]. This increase above smooth PTFE signifies that a surface roughness effect is causing advanced

wetting. This is shown in Figure 4.9 by the dashed red line. This line represents the expected wetting angle predicted for a flat coating with varying PTFE concentration based on Equation (2-3), using a contact angle of 116° for PTFE and 75° for nickel. 75° was the measured value for the electrodeposited nickel as shown in Table 4.3. When the PTFE concentration is above 50%, the measured contact angles are much greater than what is expected from just changing the surface chemistry meaning enhanced wetting through roughness is achieved.

To demonstrate the difference in surface roughness, 2D line scans from surface profilometry are shown in Figure 4.10 comparing the pure nickel sample with the Ni - 69 vol% PTFE material. The maximum peak height in the pure nickel coating line scan is $0.52\ \mu\text{m}$ and the minimum is $-0.36\ \mu\text{m}$ giving a difference of $0.88\ \mu\text{m}$. For the Ni - 69 vol% PTFE material, the line scan shows a maximum of $2.15\ \mu\text{m}$ and a minimum of $-2.69\ \mu\text{m}$ giving a difference of $4.84\ \mu\text{m}$. This shows that the addition of PTFE particles results in a higher surface roughness.

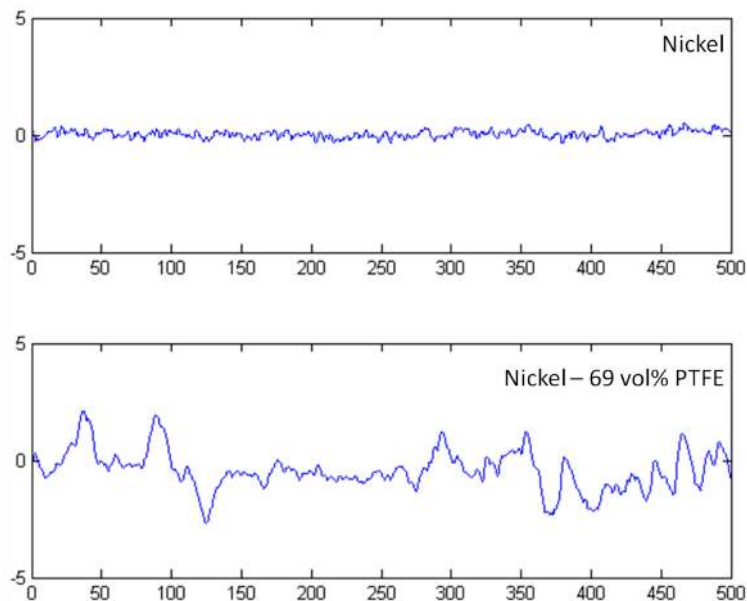


Figure 4.10: Profilometry line scans illustrating added roughness to the surface during co-deposition with PTFE particles.

By definition, a superhydrophobic surface has a contact angle with a water droplet over 150° as well as low adhesion to the droplet quantified by a very low tilt angle ($<10^\circ$) [Bhushan and Jung 2011]. The current work has shown by adding an increasing amount of PTFE particles into nickel deposits, the wetting angle of the deposit approaches 150° ; however, the water droplets still adhere to the surface of the deposits displaying tilt angles greater than 60° . Previous studies done by Ibe et al. and Wang et al. for similar material with contact angle $>150^\circ$ did not report a value for the tilt angle or contact angle hysteresis [Ibe et al. 1998, Wang et al. 2004].

The resistance of the water droplet from rolling off the surface gives a clue regarding the wetting state the droplet is in while on the surface. When comparing the two wetting states defined by Cassie-Baxter and Wenzel, it is established that a water drop in the Cassie-Baxter state will demonstrate lower contact angle hysteresis and a thus lower tilt angle [Quéré et al. 2003]. This suggests that the droplet is most likely in the Wenzel wetting state where a high contact angle is achieved accompanied with a large contact angle hysteresis. The wetting state of the Ni-PTFE samples studied here is very complex due to the non-uniform roughness and chemical composition. It has been shown in literature that contact angle is a function of the local area directly adjacent to the triple line (within approximately 100 nm), that is the interface between liquid, solid, and air [Bormashenko 2009]. The wetting state is defined by the local concentration of PTFE (see Figure 4.4 and Appendix 2) as well as the local roughness, which will vary significantly at different locations around the droplet edge. For easy water roll-off, a uniform surface is essential as any defects, such as areas of high nickel concentration, will pin the droplets and prevent roll off.

Chapter 5

Grain Refinement of Nickel Coatings

5 Grain Refinement of Nickel Coatings

The focus of this part of the study is on the grain refinement of the nickel matrix. As shown in Figure 1.6, the study presented in this chapter was done on the grain refinement of pure nickel samples without any PTFE addition.

In this section the addition of a grain refiner, saccharin, into the Watt's electroplating bath is explored on the basis of earlier results [El-Sherik and Erb 1995]. Saccharin concentrations of 0.1, 1, 3 and 5 g/L were added to the pure nickel bath shown in Table 3.2, with an additional 0.1 g/L of CTAB added. Changes to the texture and grain size of the nickel deposits are examined through the use of X-ray diffraction. Microhardness testing was done to follow the increase in hardness through grain size reduction as has been observed earlier [El-Sherik et al 1992]. Finally, contact angle measurements were performed to establish the effect of saccharin on the wetting properties of the surface.

5.1 SEM Images

SEM analysis was done to observe changes to the grain structure that are caused by the addition of CTAB and saccharin. Figure 5.1 shows x5,000 magnification micrographs of three

samples: A) pure nickel with no additives B) nickel with 0.1 g/L CTAB added to the plating bath and C) nickel with 0.1 g/L of CTAB and 0.1 g/L of saccharin added to the plating bath.

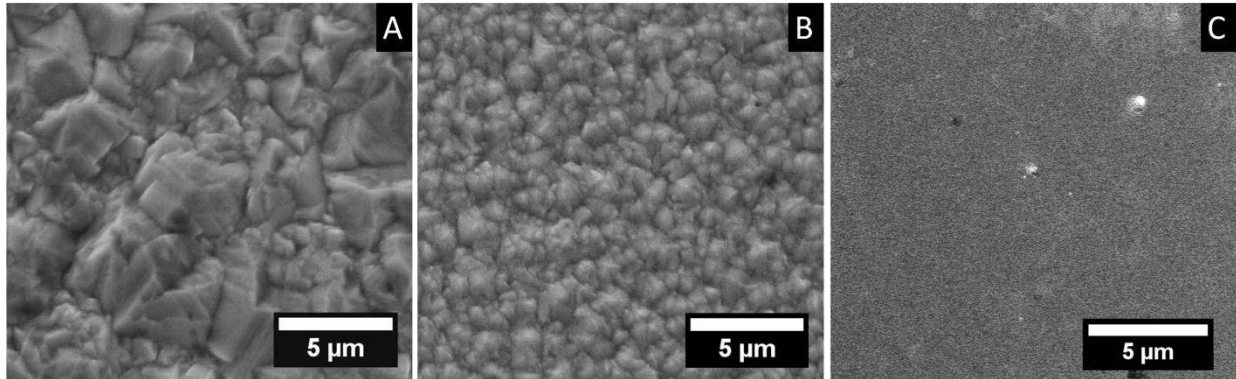


Figure 5.1: SEM images of pure nickel coatings x5,000 magnification A) no additives B) 0.1 g/L CTAB C) 0.1 g/L CTAB + 0.1 g/L saccharin

For the nickel sample with no additives, very large grains, $>2 \mu\text{m}$, are observed. The material also displays a wide grain size distribution with sub-micron grains observed in between the larger grains. The addition of CTAB into the plating bath causes significant refinement of the larger crystals as shown in Figure 5.1 B down to the sub-micron range. The grain size distribution is still wide with even smaller crystals still present in between these sub-micron grains. When saccharin and CTAB are both added to the plating bath the grain size is significantly refined further. At this point individual crystals can no longer be resolved. This indicates very small grain size likely in the nanometer scale.

5.2 XRD Results

5.2.1 Grain Size

The Scherrer formula was used to calculate the grain size of the deposits based on the peak broadening as explained in section 3.3.4. X-ray diffraction patterns are shown in Figure 5.2. Results of grain size calculations for the {111} peak are shown in Table 5.1. In addition to saccharin, a small amount (0.1 g/L) of the cationic surfactant CTAB was added to remain consistent with the bath composition during electrodeposition of Ni-PTFE composites as well as prevent pitting in the deposits. Previous work has shown that CTAB also functions as a grain refiner which can explain the low grain size observed at 0 g/L saccharin [Chen 2008]. However, the grain size of 43 nm at 0 g/L saccharin is not consistent with the surface morphology observed in Figure 5.1 B which clearly shows crystal facets of grains in the micrometer range. The peak broadening for this sample in XRD may be partially due to other effects such as internal stress or stacking faults [Cullity and Stock 2001] in addition to the broadening due to the very small grains that are present in the distribution. Therefore, the grain size given in Table 5.1 for saccharin-free nickel may be an underestimate of the average grain size.

Table 5.1: Grain size with saccharin addition

Saccharin Concentration (g/L)	Grain Size {111} Peak (nm)
0	43*
0.1	20
1	24
3	22
5	24

*Likely underestimated

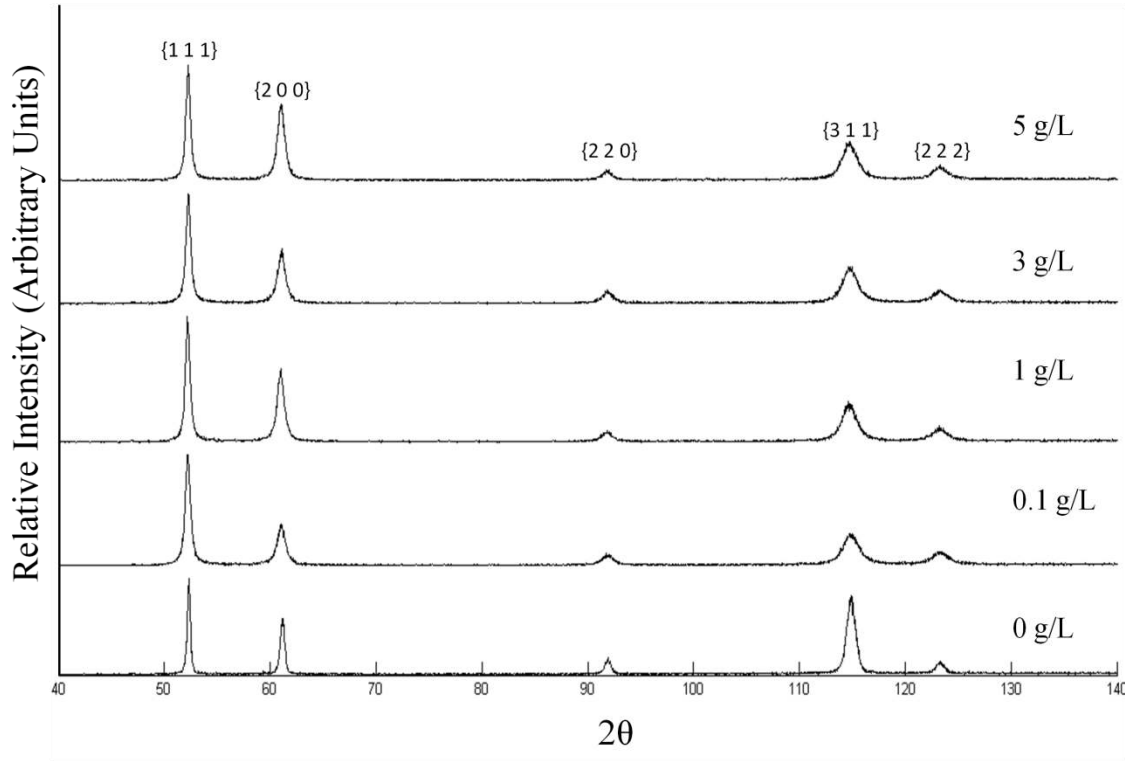


Figure 5.2: X-ray diffraction patterns for pure nickel coatings plated using different saccharin concentrations. All samples also contain 0.1 g/L CTAB.

With the addition of just 0.1 g/L of saccharin, the grain size is refined to 20 nm. Higher levels of saccharin concentration in the bath do not provide any additional grain size refinement. The small grain sizes for these materials derived from the XRD peak broadening are consistent with the SEM observations shown in Figure 5.1 C in which no crystals were resolved in the very smooth coating surfaces. A grain size of ~20 nm agrees well with work done by Rashidi and Amadeh for nanocrystalline nickel coatings under similar conditions [Rashidi and Amadeh 2010]. In their work, electroplating was done using DC power at a current density of 100 mA/cm², the grain size was greatly reduced with the addition of saccharin, and a leveling off at 20 nm was observed at 3 g/L saccharin addition. The grain size measurements in that study were done using XRD in similar fashion to the work in the current thesis.

The noticeable difference in the work presented here and the previous work by Rashidi and Amadeh, is the very fast leveling off of grain size, with no further reduction noted past 0.1 g/L of saccharin. The main experimental difference in this work was the addition of CTAB. The leveling off of the grain size with saccharin addition can be attributed to corresponding levelling off in the overpotential and/or saturation of adsorption sites at the cathode for saccharin molecules [El-Sherik and Erb 1995]. It is likely that CTAB molecules are already occupying some of the available adsorption sites at the cathode resulting in saturation of the adsorption sites at lower saccharin concentrations. As CTAB is a cationic surfactant molecule, there will be strong attraction to the negatively charged cathode.

5.2.2 Texture

Texture was investigated by calculating relative intensities of each peak compared to the relative intensity that is expected in a random nickel sample. The intensity of a randomly oriented nickel sample was calculated using the following equation,

$$I = |F|^2 p \left(\frac{1 + \cos^2 2\theta_B}{\sin^2 \theta_B \cos \theta_B} \right) \quad (5-1)$$

where I is the intensity of a diffraction line in arbitrary units, F is structure factor, p is multiplicity factor, θ_B is the Bragg angle [Cullity and Stock 2001]. Details of the calculation are included in Appendix 5. Table 5.2 summarizes the calculated relative intensities for the first five characteristic diffraction peaks of FCC nickel with random crystal orientation distribution.

Table 5.2: Calculated intensity of diffraction peaks for random nickel

Normalized Relative Intensity, <i>I</i>				
{111}	{200}	{220}	{311}	{222}
100%	46.7%	32.1%	57.2%	20.5%

Using the intensities of each peak determined from the XRD patterns, the orientation indices are calculated using equation (3-3). Table 5.3 lists the orientation index values for the first five crystallographic planes of nickel. An orientation index with a value larger than one indicates that there is a preferred texture for that peak.

Table 5.3: Orientation Index with varying saccharin concentration

Saccharin Concentration (g/L)	Grain Size (nm)	Orientation Index				
		I_{111}	I_{200}	I_{220}	I_{311}	I_{222}
0	43*	0.971	1.192	0.429	1.359	0.599
0.1	20	1.403	1.070	0.374	0.662	0.796
1	24	1.202	1.502	0.509	0.614	0.720
3	22	1.286	1.281	0.405	0.700	0.736
5	24	1.150	1.679	0.309	0.669	0.730

*Likely underestimated

For the sample containing no saccharin, a weak {200}{311} double fiber texture is observed. The {311} peak is stronger than what is typically found in electrodeposited nickel. This is likely caused by the use of CTAB as an additive. The texture is changed to a weak {111}{200} double fibre texture with the addition of saccharin. Overall the numbers presented in Table 5.3 indicate very weak crystallographic texture in these materials.

5.3 Hardness Testing

Vicker's microhardness testing was done to determine enhancement in mechanical properties that can be achieved through the current method of grain size refinement. It is well established through the Hall-Petch relationship that a reduction in grain size causes an increase in the strength and hardness of a material. Hardness values obtained for samples made using different saccharin concentrations are shown in Table 5.4. Data is not available for 5 g/L of saccharin due to the resulting coating being macroscopically too rough to perform meaningful hardness measurements as required according to ASTM standards [ASTM standard E384 2011e1]. The indentation depth was calculated for the softest sample to be 3.3 μm , which was the maximum indentation depth for any measurement. The coating thickness was approximately 50 μm after polishing for all samples, which is greater than 10x the indentation depth so there should be no influence from the copper substrate in the measurements.

Table 5.4: Microhardness values for samples produced with varying saccharin concentration

Saccharin Concentration (g/L)	XRD Grain Size (nm)	Hardness	
		(HV [kg/mm ²])	(GPa)
0	43*	352 \pm 6	3.45 \pm 0.06
0.1	20	487 \pm 8	4.78 \pm 0.08
1	24	519 \pm 7	5.09 \pm 0.07
3	22	528 \pm 9	5.18 \pm 0.09
5	24	N/A	

*Likely underestimated

The microhardness results show a large increase in the hardness from 352HV to 487HV-528HV range, an increase of up to 50%, with the addition of saccharin. This agrees with the grain size measurements (Table 5.1) which showed a large decrease in grain size when 0.1 g/L of

saccharin was added. Previous work has been done relating the grain size to microhardness values for nanocrystalline metal [El-Sherik et al. 1992]. In this study the hardness of nickel increased with decreasing grain size down to 11 nm. The trend between hardness and grain size found in the present study is directionally very similar to the study by El-Sherik. In order to explain the somewhat lower hardness of the sample with 20 nm grain size compared with the materials with 22 and 24 nm grain size, details of the grain size distributions are required. X-ray diffraction provides only an average grain size. Grain size distribution could be obtained from extensive transmission electron microscopy studies which should be done in future work.

5.4 Wetting Properties

The saccharin addition to the electroplating bath resulted in a transition in surface finish from a dull grey to a smooth, mirror like surface finish. Table 5.5 and Figure 5.3 show the result of contact angle measurements versus saccharin concentration in the bath. It was observed that an increase in the amount of saccharin in the bath produced samples displaying a decrease in the contact angle from $75^\circ \pm 10^\circ$ to $54^\circ \pm 10^\circ$.

Table 5.5: Contact angle of water on nickel samples with the addition of saccharin

Saccharin Concentration (g/L)	XRD Grain Size (nm)	Contact Angle ($^\circ$)
0	43	75 ± 10
0.1	20	63 ± 3
1	24	57 ± 9
3	22	59 ± 10
5	24	54 ± 10

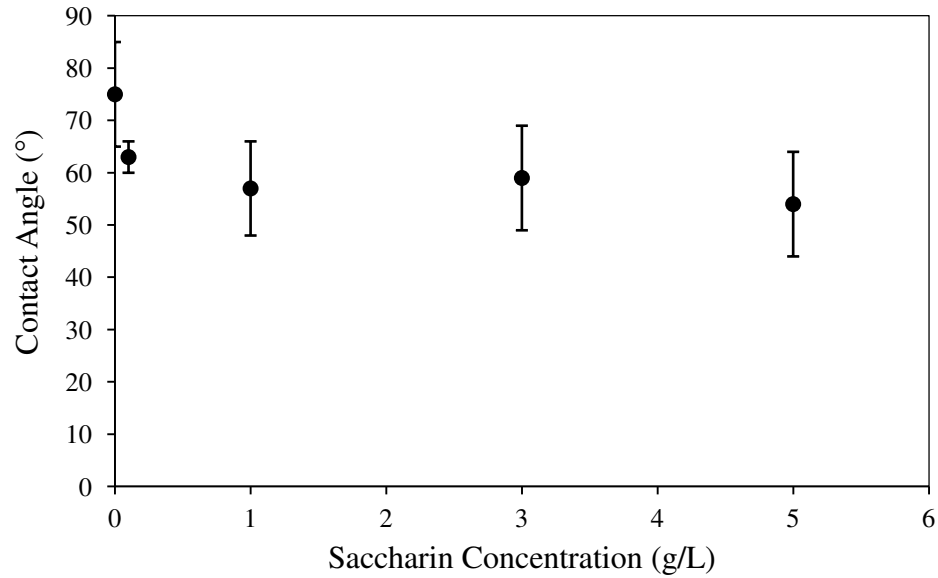


Figure 5.3: Contact angle as a function of saccharin concentration in the bath

Previous work has shown that grain size does not have a significant effect on the wetting properties of nickel [Hsiao 2002]. In this study, nickel samples with different grain sizes were polished to a very flat surface and the contact angles were measured. No significant difference was found indicating no change to the surface energy with changes in grain size. An important factor in the interpretation of this finding was the possible presence of a thin nickel oxide layer that forms when nickel is exposed to air. As a change in grain size does not account for the drop in wetting angle, a possible cause for the decreasing contact angle observed in Figure 5.3 could be changes to the surface structure. The surface structure of the nickel coating changed with the addition of saccharin. This can be seen at a macroscopic level as the reflectivity of the surface increases when saccharin is added and the coatings have a mirror like finish. The SEM images shown in Figure 5.1 show a significant change to the microstructure occurs when saccharin is added. In Figure 5.1 A and B, a coarse pyramidal structure is observed and when a small amount

of saccharin is added this transitions into to a much smoother surface with no resolvable surface features seen in Figure 5.1 C.

Chapter 6

Nanocrystalline Nickel – PTFE Composite

6 Nanocrystalline Nickel - PTFE Composite

In Chapter 4, it was established that PTFE addition to a nickel surface can drastically increase the wetting angle. Then in Chapter 5, it was demonstrated that saccharin can be added to the plating bath to refine the grain size to the nano-scale and thus significantly increase the hardness of a nickel deposit. In this section, as shown in Figure 1.6, the results of combining the two approaches will be presented. Both PTFE and saccharin will be added to the electroplating bath in an effort to produce a composite coating containing PTFE particles embedded in a nanocrystalline nickel matrix. PTFE concentration was kept constant at 30 g/L, the optimal concentration found in section 4.2, while the saccharin concentration was varied from 0.1-5 g/L as was done in Chapter 5. X-ray diffraction and microhardness testing was carried out to determine changes to the crystal structure of the nickel matrix and contact angle measurements will reveal changes that occur in the wetting properties. Finally surface profilometry was utilized to examine the surface roughness of different deposits.

6.1 XRD Patterns

X-ray diffraction patterns for the samples containing varying amount of saccharin are shown in Figure 6.1. All samples were electroplated using 30 g/L of PTFE with 1 g/L of CTAB.

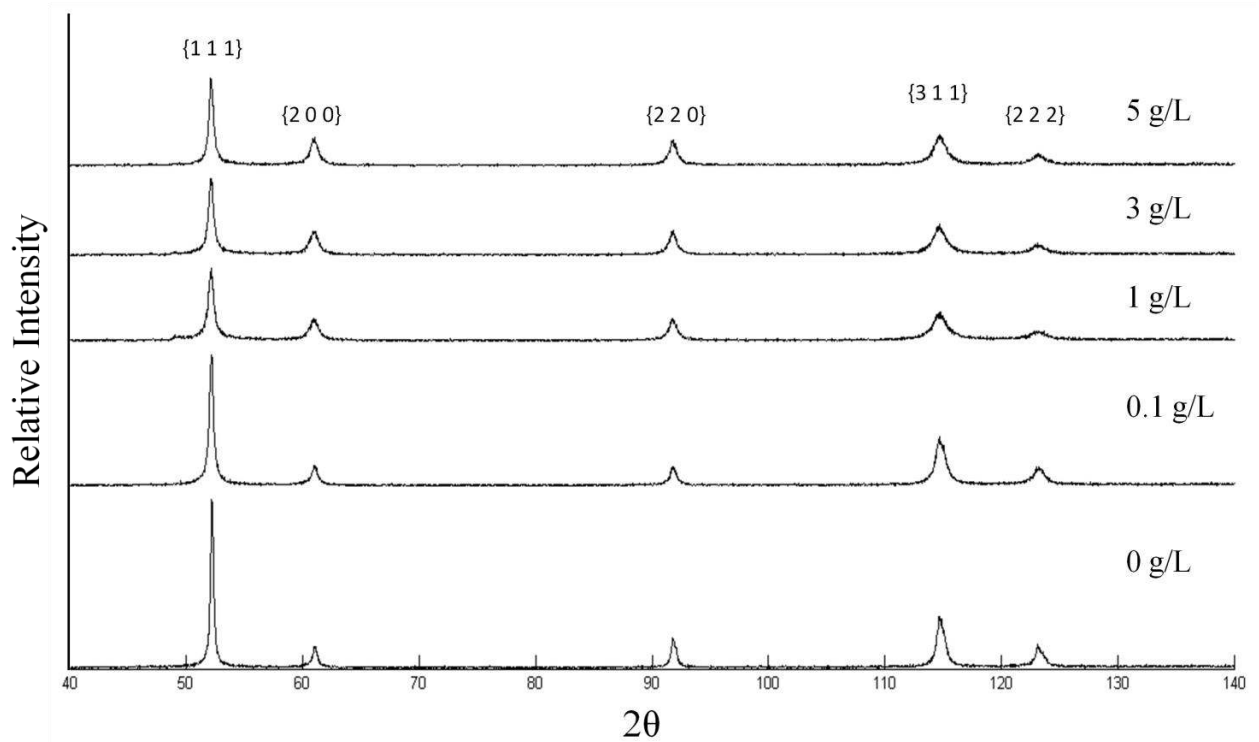


Figure 6.1: X-ray diffraction patterns of Ni-PTFE coatings plated using different saccharin concentrations

6.1.1 Grain Size

Results of grain size determined through peak broadening (Equation (3-1)) are presented in Table 6.1. The grain size calculated is shown along with the concentration of saccharin used as well as the PTFE content in the coatings.

The grain sizes calculated for these samples show a large decrease from 54 to 31 nm with the addition of 0.1 g/L of saccharin. The grain sizes measured for the samples containing PTFE were generally larger than the nickel samples containing the same saccharin concentrations as seen in Table 5.1. This is likely due to different growth behavior when PTFE particles are added to the matrix. While there does not seem to be a trend relating grain size to the saccharin concentration, the grain size appears to be related to the amount of PTFE co-deposited. The

samples containing greater amounts of PTFE have larger measured grain size. As the Scherrer formula gives only an approximation of grain size through an indirect method, more accurate grain size measurements through transmission electron microscope analysis are needed to make any conclusions regarding any possible relationship between grain size and PTFE content.

Table 6.1: Grain size measured using the Scherrer formula for Ni-PTFE samples with varying saccharin concentration

Saccharin Concentration (g/L)	PTFE Content (vol%)	Grain Size (nm)
0	69 ± 4	54*
0.1	59 ± 7	31
1	48 ± 4	21
3	52 ± 0.2	24
5	59 ± 4	27

*Likely underestimated

6.1.2 Texture

The orientation index calculated for the Ni-PTFE composites are shown in Table 6.2. The Ni-PTFE sample containing no saccharin concentration was formed with a weak double fibre {111}{311} texture. This is in contrast with the nickel sample prepared using no saccharin which had a weak {200}{311} double fibre texture (Table 5.3). Another difference observed is that the {200} peak for the Ni-PTFE sample was very weak with an I_{hkl} value of 0.3; compared to when no PTFE was present this value was 1.2. It appears that PTFE addition is causing a change in the nickel grain orientations.

Table 6.2: Orientation Index for Ni-PTFE samples with varying saccharin concentration

Saccharin Concentration (g/L)	Grain Size (nm)	Orientation Index, I_{hkl}				
		I_{111}	I_{200}	I_{220}	I_{311}	I_{222}
0	54	1.300	0.299	0.697	1.291	0.796
0.1	31	1.423	0.414	0.670	0.914	1.024
1	21	1.265	0.767	1.094	0.798	0.653
3	24	1.226	0.785	1.123	0.781	0.805
5	27	1.262	0.785	1.121	0.724	0.788

The addition of saccharin alters the texture slightly, as the texture transitions to a weak $\{111\}\{220\}$ double fibre. The I_{hkl} values for samples containing 1, 3 and 5 g/L of saccharin, are all quite close to 1, showing very close to random orientation. The orientation index of the $\{200\}$ planes increases as the grain size decreases, this is opposite to the effect observed for pure nickel samples. There is once again a distinct change to the orientation that is observed with saccharin addition.

6.2 Hardness

Microhardness results for the samples are shown below in Table 6.3. The hardness values are an average of five measurements. Compared with the hardness values for pure nickel, there are very high standard deviations associated with these measurements. This is likely due to the fact that the hardness values for the composite are strongly dependent on the local PTFE concentration at the indentation site, which will vary due to non-uniform particle distribution (as seen in SEM micrographs in Figure 4.4 and Appendix 2).

Table 6.3: Hardness values for Ni-PTFE composite coatings with varying saccharin content

Saccharin (g/L)	PTFE content (vol%)	Grain Size (nm)	Composite Hardness		Nickel Hardness*	
			(HV)	(GPa)	(HV)	(GPa)
0	69 ± 4	54	145 ± 45	1.42 ± 0.44	352 ± 6	3.45 ± 0.06
0.1	60 ± 7	31	228 ± 31	2.24 ± 0.30	487 ± 8	4.77 ± 0.08
1	48 ± 4	21	268 ± 27	2.63 ± 0.26	519 ± 7	5.09 ± 0.07
3	52 ± 0.2	24	266 ± 35	2.61 ± 0.35	528 ± 9	5.17 ± 0.09
5	59 ± 4	27	226 ± 26	2.22 ± 0.25	N/A	N/A

*From Table 5.4 for pure nickel samples deposited at the same saccharin concentration

The results of the hardness measurements shows a significant increase in hardness when saccharin is added to the plating bath. The addition of 0.1 g/L of saccharin to the plating bath resulted in a 57% increase in hardness over the saccharin free sample. The increase in hardness can be attributed to two factors, the increase in hardness of the nickel matrix from grain size refinement as well as a decrease in the amount of soft PTFE particles in the deposit, i.e. higher volume fractions of hard nickel phase.

A rule of mixtures can be used to predict the hardness of the various samples. Equation 6.1 shows the rule of mixtures used to predict the hardness of a composite material in general,

$$H_C = f_{Ni}H_{Ni} + f_{PTFE}H_{PTFE} \quad (6-1)$$

where H_C is the calculated hardness of the composite, H_{Ni} and H_{PTFE} are the hardness values for nickel and PTFE respectively, and f_{Ni} and f_{PTFE} are the volume fractions of nickel and PTFE respectively. Equation (6-1) is based on the Voigt model where an iso-strain condition is assumed.

A study was done by Kim to determine the validity of using the rule of mixtures to predict the hardness of particle reinforced composites [Kim 2000]. In this study, the finite element method (FEM) was used to calculate stress-strain curves and hardness values for a composite of nickel inclusions in a silver matrix. The results were compared to predicted values for the rule of mixtures under iso-strain and iso-stress conditions. The results of the FEM model show that the stress states match closely to the iso-strain when a high volume fraction of particles was present, and match the iso-stress condition for a low volume fraction of particles [Kim 2000]. All the samples in this study contain a high volume fraction (>45 vol%) and therefore it can be assumed that an iso-strain condition is met during hardness testing.

Figure 6.1 shows the measured values of hardness compared to the calculated values using Equation (6-1). The volume fractions used in this calculation are the average volume fractions as measured by EDS. The values used for H_{Ni} are the hardness values measured for the pure nickel samples when using the same concentration of saccharin, as shown in the last column of Table 6.3. Hardness of PTFE must be approximated, as there are no reported values for Vicker's hardness of PTFE. Hardness of polymers, including PTFE, is generally measured in the Shore D scale or Rockwell R. The hardness values for the Fluon[®] PTFE powders used in the research are D55 (Shore) and R25 (Rockwell), however there is no conversion factor from these scales to Vicker's hardness.

To approximate the hardness of PTFE, a generalized relation between tensile strength, σ_{UTS} , and Vicker's hardness, H_V , is used. Equation (6-2) has been shown to be a reliable predictor for metals [Brooks et al. 2008], and as an approximation it will be assumed that this relationship holds true for PTFE. Tensile strength for Fluon[®] PTFE powders, as given by the manufacturer,

ranges from 20.6-34.3 MPa [Fluon 2007]. The values for σ_{UTS} and H_V to be used in equation (6-2) are in GPa.

$$H_V = 3 \cdot \sigma_{UTS} \quad (6-2)$$

This relationship gives an approximate Vicker's hardness range of 6.3-10.5 HV (0.062-0.103 GPa) for the PTFE particles used in this research. Equation (6-1) was used to calculate predicted hardness values for the composite. Table 6.4 and Figure 6.2 show the calculated hardness values compared to the measured values.

Table 6.4: Comparison between measured hardness values for Ni-PTFE composite and predicted hardness using Equation (6-1)

Saccharin Concentration (g/L)	PTFE Content (vol%)	Measured Hardness (HV)	Predicted Hardness (HV)	
			PTFE $H_v = 6.3HV$	PTFE $H_v = 10.5HV$
0	69 ± 4	145 ± 45	113	116
0.1	60 ± 7	228 ± 31	199	201
1	48 ± 4	268 ± 27	273	275
3	52 ± 0.2	266 ± 35	257	259
5	59 ± 4	226 ± 26	N/A*	N/A*

*Predicted hardness is not available since no hardness values are available for nickel matrix with 5g/L of saccharin (see Table 5.4)

Figure 6.2 shows the rule of mixture results agree directionally with the measured values for hardness. While the trend is the same, it is noted that the predicted hardness values are consistently lower than the measured hardness. The reason for this is likely due to a difference in local PTFE concentration at the indentation site compared to the measured average value used in the rule of mixture. To ensure an accurate hardness measurement, the indentation site must be chosen such that the diamond indentation is clearly visible and the diagonals can be measured

correctly. While doing hardness measurements it was found that the indentations cannot be resolved easily when there is a very high concentration of PTFE particles, so therefore it was necessary to find lower PTFE concentration areas to indent in. For this reason, the PTFE volume fraction used in the rule of mixture is very likely an overestimate of the local PTFE concentration at the indentation site and thus predicts lower hardness than the measured values.

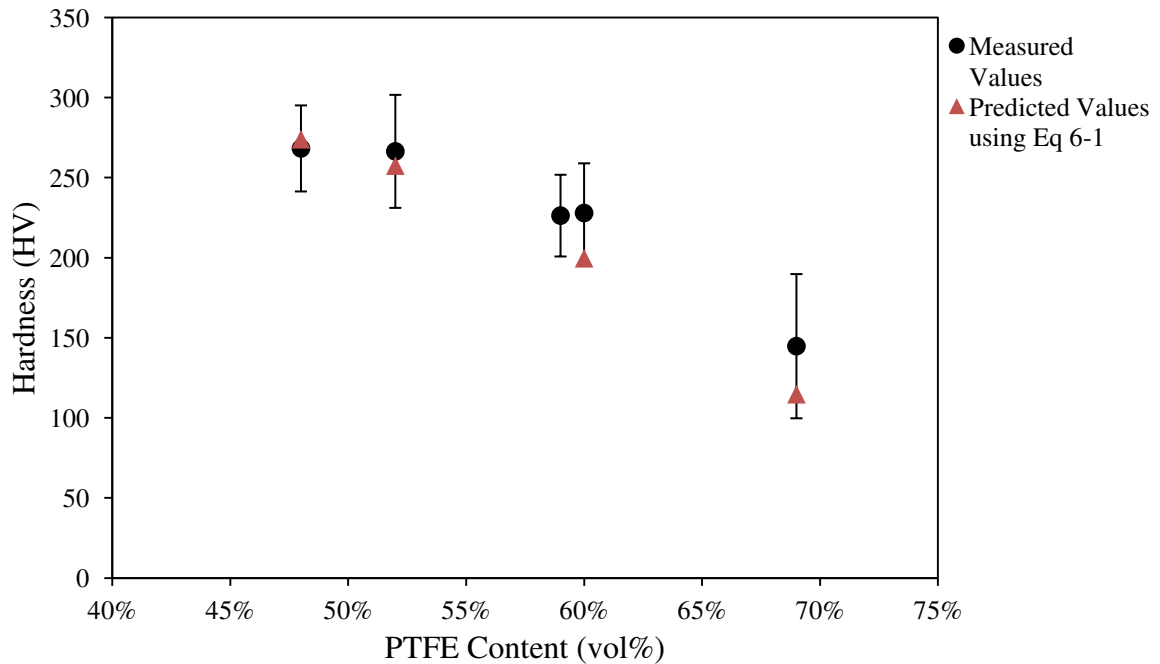


Figure 6.2: Comparison between measured hardness values for Ni-PTFE composite and predicted hardness using Equation (6-1)

The agreement between the rule of mixtures prediction and the actual measured hardness shows that the grain size refinement technique is still effective when PTFE is co-deposited with the nickel. This agrees with the XRD results which show a decrease in grain size from 54 nm to 31 nm with the addition of 0.1 g/L of saccharin.

For the samples in Table 6.3 that contain saccharin, similar hardness values are measured for the samples that have similar PTFE content, such as for 0.1 g/L and 5 g/L of saccharin as well as 1 g/L and 3 g/L. This leads to the conclusion that after the addition of 0.1 g/L of saccharin, there is little improvement in the hardness of the composite caused by further saccharin addition.

6.3 Wetting Properties

Table 6.5 shows the measured wetting angle versus saccharin concentration in the bath. The addition of saccharin to the nickel plating bath containing PTFE particles caused a continuous decrease in the measured contact angle. The samples had a varying amount of PTFE in the deposits with no distinct trend between saccharin concentration and PTFE content. To take into account changes in wetting properties based on composition, the expected wetting angle based on the PTFE content was calculated for each sample using the linear relationship between PTFE content and contact angle developed in section 4.3. The measured wetting angle was compared to the expected wetting angle, showing a very large drop in contact angle when the saccharin concentration was 1 g/L or greater.

The addition of saccharin has a large effect on the wetting properties of the Ni-PTFE surface, lowering the contact angle below what was measured for a pure nickel surface. The EDX results show that there is a substantial amount of PTFE co-deposited; however, this PTFE no longer imparts the same effect that was noted for the saccharin free composites in section 4.3.

Investigation of changes to the surface structure was done by examining SEM images of the Ni-PTFE surfaces plated with saccharin as shown in Figure 6.3. The SEM images show a change in the morphology of the nickel matrix, transitioning from coarse, pyramidal type structure seen in Figure 6.3 A, to a fine, more rounded structure seen in Figure 6.3 C-E.

Table 6.5: Summary of PTFE content and contact angle for samples containing 0-5 g/L of saccharin.

Saccharin Concentration (g/L)	PTFE Content (vol%)	Measured Contact Angle	Expected Contact Angle	Difference in Contact Angle
0	69 ± 4	152 ± 8°	152°	0
0.1	60 ± 7	130 ± 10°	128°	+2°
1	48 ± 4	86 ± 27°	96 °	-10°
3	52 ± 0.2	73 ± 11°	108°	-35°
5	59 ± 4	53 ± 11°	126°	-73°

6.4 Surface Profilometry

Surface profilometry results of the five samples containing 0-5 g/L of saccharin are shown in Figure 6.4. These images are 2D colour plots, where the colour is representative of the height of the surface at that point. The colour bars have been adjusted in MATLAB to be consistent amongst profiles in order to easily visualize differences between samples. All values have units of μm . Further images of surface profilometry and SEM images of the surfaces are included in Appendix 6.

For all plots, the median plane represented by height 0 is displayed in light green. Peaks are shown in a gradient from yellow to red with orange representing a height of about 5 μm

above the median and red being roughly 8-10 μm and above. Valleys in the surface are shown in a gradient from light blue to dark blue. The dark blue areas represent areas between -3 and -5 μm in height or below.

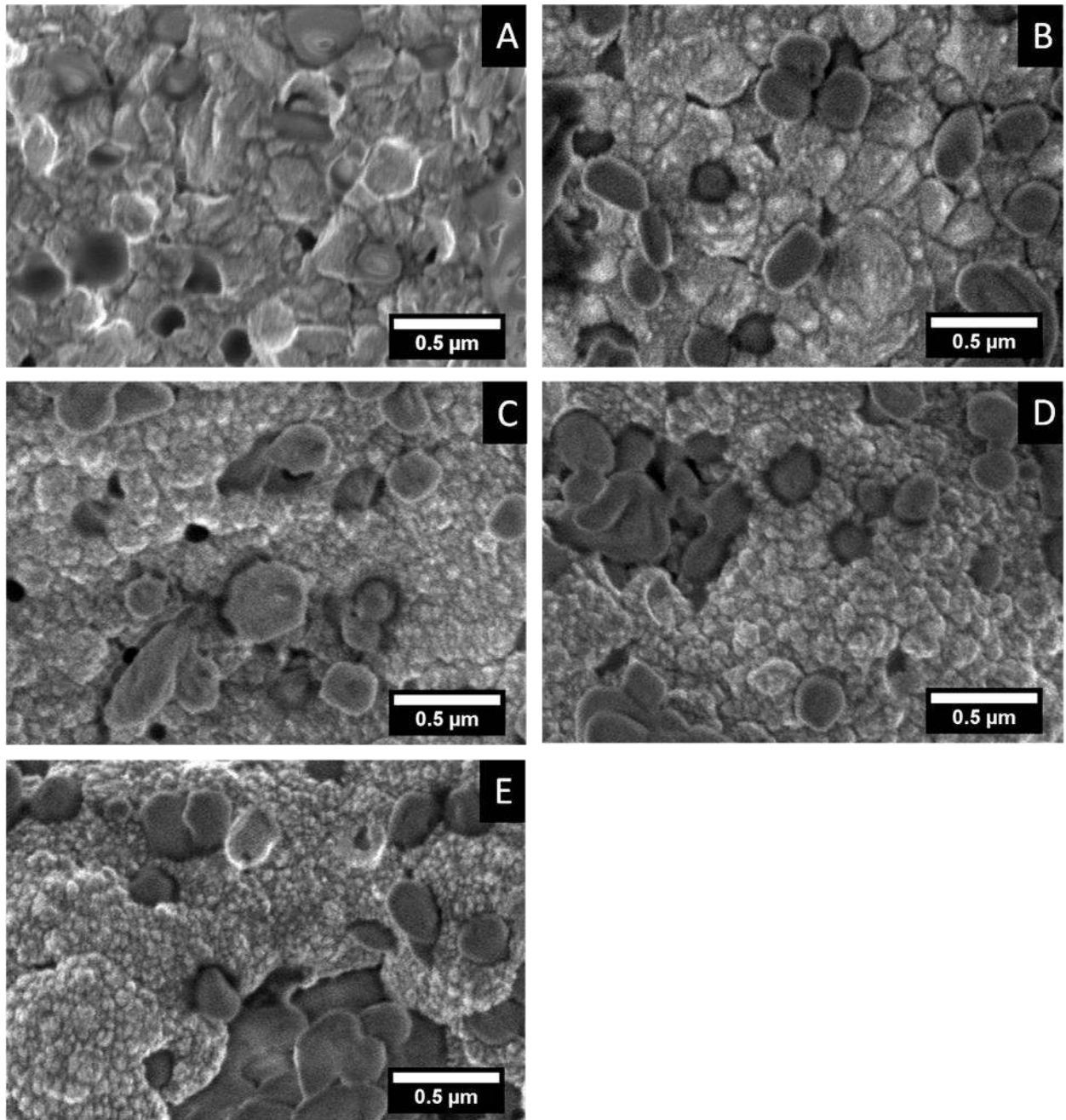


Figure 6.3: SEM images at x20,000 magnification A) 0 g/L saccharin B) 0.1 g/L saccharin C) 1 g/L saccharin D) 3 g/L saccharin E) 5 g/L saccharin

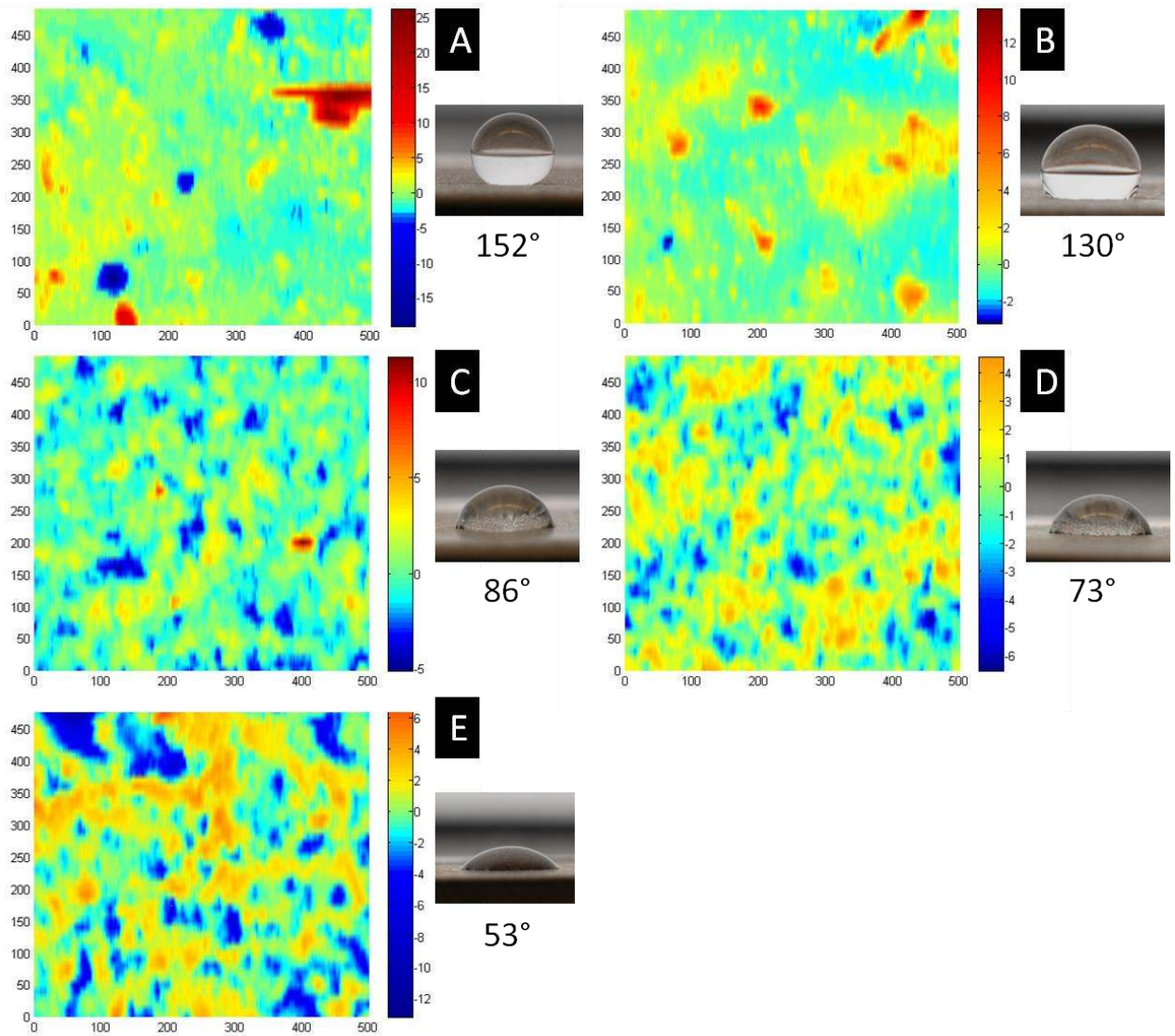


Figure 6.4: 2D colour plots of surfaces with colour representing height of the surface. A,B,C,D,E represent samples with 0, 0.1, 1, 3, 5 g/L saccharin respectively.

Qualitatively, there appears to be a significant transition from images A and B to C,D,E. Images A and B show relatively flat surfaces with large distinct peaks scattered throughout the surface. There are very few valleys except for a few very deep, circular valleys in image A which are pits formed in the coating from the electrodeposition process. In images C,D and E,

the number of valleys present increases drastically, and there appears to be an equal number of valleys and peaks evenly distributed across the surface. There are no distinct outliers, particularly in images D and E where no area has a peak higher than 5 μm

Further detail of the surfaces can be obtained when looking at individual line scans from these images. Figure 6.5 shows a line scan for each sample taken from the 2D maps at $y=400 \mu\text{m}$. This particular spot was chosen as no outlying extreme peaks or valleys appear at this point in any of the samples.

The line scans reaffirm the qualitative observations noted above. Scans A and B both consist of mainly peaks varying in height protruding from a roughly level surface with very few if any valleys. This transitions quite dramatically as a number of deep valleys in samples are present in C,D and E. Also of note, the peaks in these three samples are smoother and broader, resulting in lower peak density (peaks/ μm). Scans A and B have areas of relatively flat surface consisting of many small sharp peaks, this type of feature doesn't appear in scans C,D and E.

The roughness factor, R_f , as defined in the Wenzel model (Equation (2-2)) could not be measured due to limitations in the resolution of the profilometer. The limiting factor for the resolution was the stylus tip radius, which was 2 μm for this instrument. Surface features smaller than the tip radius will not accurately be recorded by the stylus and a true measure of the very fine surface roughness features is impossible with this particular instrument.

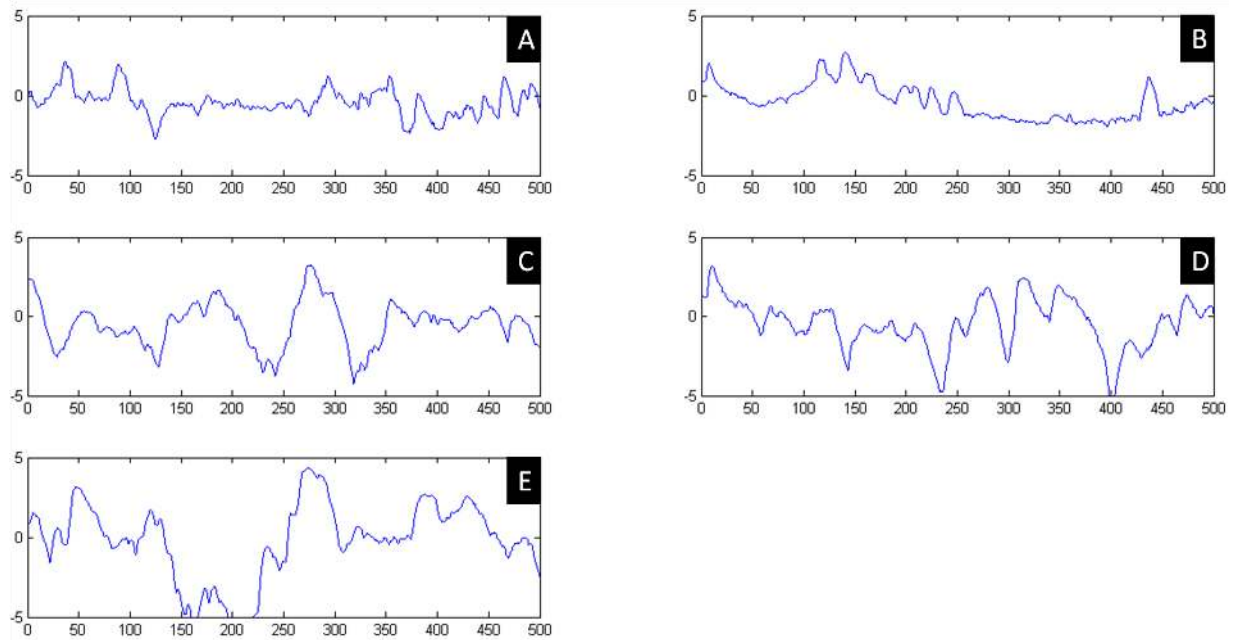


Figure 6.5: Line scans of surfaces taken at $y=400 \mu\text{m}$ in Figure 6.4. A,B,C,D,E represent samples with 0, 0.1, 1, 3, 5 g/L saccharin respectively.

The connection between these changes to surface morphology and the associated drastic decrease in contact angle is not entirely known at this point. The transition from a flat surface with many sharp peaks to a surface containing both peaks and valleys may be indicative of a change in the way PTFE is exposed on the surface. For enhanced wetting to occur in this composite system, the PTFE particles embedded must be exposed to the surface, protruding above the nickel matrix in order to have significant effect on the contact angle. If many of the PTFE particles are concentrated in valleys, they will not have an effect on the contact angle. The contact angle measured of 53° , when 5 g/L of saccharin was added to the bath, is very low, lower in fact than any of the pure nickel surfaces measured, even though EDX results show 59 vol% PTFE. Assuming a flat surface, the change in surface energy from the addition of that concentration of PTFE should increase the contact angle to 96° using the Cassie equation

(Equation (2-3)). This means that the amount of PTFE being exposed to the water droplet interface is much less than what is indicated by EDX. The conclusions from the surface profilometry points towards a change in the growth mechanism during the co-deposition process when the grain size is refined through saccharin addition. This change appears to have a detrimental effect on the hydrophobicity of the surface.

Chapter 7

Conclusions

7 Conclusions

In conclusion, the work presented in this thesis provides a synthesis method to produce a metal-matrix composite displaying a superhydrophobic surface. Electrodeposition was used as a method to produce nickel coatings containing a significant amount of PTFE particles embedded throughout the deposit. The PTFE particles provide a change in the chemical makeup of the surface, lowering the surface energy, as well as providing roughness to the surface that allows for drastic alterations to the wetting properties of nickel. The main objective of the thesis was divided into three sections as displayed in Figure 1.6. The findings for each section are summarized below.

Study of the co-deposition process showed that the concentration of PTFE particles in the electroplating bath had a significant effect on the amount of co-deposited PTFE. Increasing the PTFE composition in the bath from 5-40 g/L, resulted an increase of embedded PTFE from 41 vol% up to a maximum of 69 vol% at a concentration of 30 g/L. The inclusion of PTFE particles was able to significantly increase the water contact angle from $75 \pm 10^\circ$ for pure nickel to $152 \pm 8^\circ$ when the composition was 69 vol% PTFE.

Saccharin, a known grain refiner in electrodeposition processes, was added in various concentrations to a nickel electroplating bath. Through the use of X-ray diffraction, grain size

was calculated based on line broadening that occurs due to small crystal size. It was found that the addition of just 0.1 g/L of saccharin resulted in a 50% decrease in grain size, from over 40 nm to 20 nm. Saccharin concentrations of 1, 3 and 5 g/L did not show any additional grain size refinement. It should be noted that the addition of CTAB to the plating bath already resulted in significant grain size refinement compared with pure Watt's bath. The grain size refinement results in a large increase in the hardness of the nickel, measured by Vickers microhardness. The Vickers microhardness increased 40% with the addition of 0.1 g/L of saccharin, increasing from 352 ± 6 HV with no saccharin added, to 487 ± 8 HV. A maximum hardness of 527 ± 9 HV was measured for sample synthesized using 3 g/L saccharin. The addition of saccharin also was observed to cause a decrease in the contact angle from $75 \pm 10^\circ$ to $54 \pm 10^\circ$, with 0 and 5 g/L of saccharin respectively.

The addition of saccharin to the electroplating bath containing 30 g/L of PTFE had the same grain refining effect seen in the pure nickel samples. The grain size of the nickel matrix, measured using XRD, varies between 20-30 nm and the measured size appears to be influenced by the amount of PTFE in the deposit. Microhardness measurements show a 57% increase in hardness with the addition of 0.1 g/L of saccharin, going from 145 ± 45 HV to 225 ± 31 HV. No significant increase in hardness was noted with further saccharin addition.

The contact angle for nano-Ni-PTFE samples, dropped significantly with the addition of saccharin. Upon taking into account fluctuations in the PTFE content, the wetting angle dropped by as much as 70° when 5 g/L of saccharin was added. SEM images along with surface profilometry of the samples reveals significant changes to the surface morphology, in particular a transition from flat surface with distinct peaks to a uniform, wavy surface with equal peaks and

valleys. The severe drop in the wetting angle with the addition of saccharin appears to be linked closely to the modification of the surface morphology.

The combined results of the wetting angle and hardness testing of the nano-Ni-PTFE composite coatings show that a superhydrophobic coating with enhanced strength can be achieved with the addition of a small amount of saccharin to the electroplating bath. With the addition of 0.1 g/L of saccharin the composite coating gained a 57% increase in hardness while maintaining a very high contact angle. Further increase in saccharin concentration caused a significant decrease in wetting angle while not providing substantial improvement in hardness. Therefore in conclusion, the best results to achieve a high hardness, superhydrophobic composite coating are obtained with the addition of 30 g/L of PTFE and 0.1 g/L of saccharin to the electroplating bath.

For the final composite material there are several variables that will affect the structure and properties of the coating. The grain size of the nickel matrix is decreased with the addition of the surfactant CTAB and substantially more with the addition of saccharin. The amount of PTFE in the composite deposit is controlled mainly by the PTFE concentration in the electroplating bath. The addition of surfactant (CTAB) allows for dispersion of particles and the breakup of agglomerates which will increase the amount of PTFE co-deposited as well as possibly changing the size distribution of deposited PTFE particles.

Chapter 8

Future Work

8 Recommended Future Work

There are several areas in this research where further investigation is needed to achieve the desired goals. The first area of work needed is to decrease the roll off angle down to 10° or below to create a true superhydrophobic surface. Based on the SEM images of the Ni-PTFE samples created in this work, the wide size distribution of the PTFE particles caused a non uniform surface to form, where the concentration of large PTFE particles varied throughout the surface. A narrow particle size distribution should help ensure even distribution of particles across the surface, which may aid in preventing the water droplet from pinning on areas of high nickel concentration. Experiments testing different sized (micron versus submicron) PTFE particles with narrow particle size distributions can aid in optimizing the contact and roll off angle to produce a superhydrophobic surface.

Further research can be done on quantifying the effects of plating parameters on the co-deposition process. Factors such as current density and agitation in the bath likely have a substantial effect of the amount of PTFE content in the deposit. Controlled studies can be done to isolate the effects of these parameters on co-deposition rates. The effect of current density of the grain size distribution of the nickel matrix should also be further studied.

XRD as a measure of grain size is an indirect measurement technique and the end results are an approximation. An accurate measure of grain size is needed to verify the trends noted between grain size and PTFE incorporation in the coatings. The most direct method of grain size determination is through TEM analysis. It is suggested that TEM analysis of coatings should be done to get better insight into the grain size of the nickel in all samples.

Further research into the surface morphology can be aided by the use of high resolution instruments. Optical profilometry or atomic force microscopy (AFM) are two potential methods that can be used to allow for a more detailed look at the surface morphology. An increase in the detail of the surface structure will allow for characterization of protrusion heights and widths of the surface.

Finally, the method of refining grain size when PTFE particles are present needs to be investigated. The saccharin addition has proven effective in reducing grain size, but there is a coinciding detrimental effect to the contact angle measurements. An alternative method to grain size refinement through electrodeposition is the use of nickel phosphorous alloys. This alternative method should be investigated as the Ni-P-PTFE composite may prove to be effective in refining grain size while maintaining superhydrophobicity. Hardness of the composite coatings can be further improved if smaller grain sizes can be achieved without affecting the wetting properties.

References

- Ankita, S. and A.K. Singh. "Corrosion and Wear Resistance Study of Ni-P and Ni-P-Ptfe Nanocomposite Coatings." *Central European Journal of Engineering* 1, no. 3 (2011): 234-243.
- Arai, S. and A. Kato. "Mechanism for Codeposition of Multiwalled Carbon Nanotubes with Copper from Acid Copper Sulfate Bath." *Journal of the Electrochemical Society* 160, no. 9 (2013): D380-D385.
- ASTM Standard E384, 2011e1. "Standard Test Method for Knoop and Vickers Hardness of Materials ", ASTM International ,West Conshohocken, PA, 2011, www.astm.org
- Balaji, R., M. Pushpavanam, K. Y. Kumar and K. Subramanian. "Electrodeposition of Bronze-Ptfe Composite Coatings and Study on Their Tribological Characteristics." *Surface & Coatings Technology* 201, no. 6 (2006): 3205-3211.
- Bechert, D. W., M. Bruse and W. Hage. "Experiments with Three-Dimensional Riblets as an Idealized Model of Shark Skin." *Experiments in Fluids* 28, no. 5 (2000): 403-412.
- Bercot, P., E. Pena-Munoz and J. Pagetti. "Electrolytic Composite Ni-Ptfe Coatings: An Adaptation of Guglielmi's Model for the Phenomena of Incorporation." *Surface & Coatings Technology* 157, no. 2-3 (2002): 282-289.
- Bhushan, B. and Y. C. Jung. "Micro- and Nanoscale Characterization of Hydrophobic and Hydrophilic Leaf Surfaces." *Nanotechnology* 17, no. 11 (2006): 2758-2772.
- Bhushan, B. and Y. C. Jung. "Natural and Biomimetic Artificial Surfaces for Superhydrophobicity, Self-Cleaning, Low Adhesion, and Drag Reduction." *Progress in Materials Science* 56, no. 1 (2011): 1-108.
- Bormashenko, E. "A Variational Approach to Wetting of Composite Surfaces: Is Wetting of Composite Surfaces a One-Dimensional or Two-Dimensional Phenomenon?" *Langmuir* 25, no. 18 (2009): 10451-10454.
- Brooks, I., P. Lin, G. Palumbo, G. D. Hibbard and U. Erb. "Analysis of Hardness-Tensile Strength Relationships for Electroformed Nanocrystalline Materials." *Materials Science and Engineering a-Structural Materials Properties Microstructure and Processing* 491, no. 1-2 (2008): 412-419.

- Busscher, H. J., A. W. J. Vanpelt, H. P. Dejong and J. Arends. "Effect of Spreading Pressure on Surface Free-Energy Determinations by Means of Contact-Angle Measurements." *Journal of Colloid and Interface Science* 95, no. 1 (1983): 23-27.
- Cao, L. L., A. K. Jones, V. K. Sikka, J. Z. Wu and D. Gao. "Anti-Icing Superhydrophobic Coatings." *Langmuir* 25, no. 21 (2009): 12444-12448.
- Cassie, A. B. D. "Contact Angles." *Discussions of the Faraday Society* 3, (1948): 11-16.
- Cassie, A. B. D. and S. Baxter. "Wettability of Porous Surfaces." *Transactions of the Faraday Society* 40, (1944): 0546-0550.
- Celis, J.P. and J.R. Roos. "Kinetics of the Deposition of Alumina Particles from Copper Sulfate Plating Baths ".
- Celis, J.P. and J.R. Roos. "Kinetics of the Deposition of Alumina Particles from Copper Sulfate Plating Baths " *Journal of The Electrochemical Society* 124, no. 10 (1977): 1508-1511.
- Chen, Li, Liping Wang, Zhixiang Zeng and Junyan Zhang. "Effect of Surfactant on the Electrodeposition and Wear Resistance of Ni–Al₂O₃ Composite Coatings." *Materials Science and Engineering: A* 434, no. 1–2 (2006): 319-325.
- Choo, R. T. C., J. M. Toguri, A. M. El-Sherik and U. Erb. "Mass Transfer and Electrocrystallization Analyses of Nanocrystalline Nickel Production by Pulse Plating." *Journal of Applied Electrochemistry* 25, no. 4 (1995): 384-403.
- Cullity, B. D. and S.R. Stock *Elements of X-Ray Diffraction*. 3rd ed. Upper Saddle River: Prentice Hall, 2001.
- Dao, M., L. Lu, R. J. Asaro, J. T. M. De Hosson and E. Ma. "Toward a Quantitative Understanding of Mechanical Behavior of Nanocrystalline Metals." *Acta Materialia* 55, no. 12 (2007): 4041-4065.
- Di Bari, G.A. "Electrodeposition of Nickel." In *Modern Electroplating*, edited by M. Schlesinger and M. Paunovic, 79-114. Hoboken, NJ: Wiley, 2010.
- Dukhin, A., S. Dukhin and P. Goetz. "Electrokinetics at High Ionic Strength and Hypothesis of the Double Layer with Zero Surface Charge." *Langmuir* 21, no. 22 (2005): 9990-9997.

- Dukhin, A.S. and P.J. Goetz. *Characterization of Liquids, Nano- and Microparticulates, and Porous Bodies Using Ultrasound*. 2nd ed. Studies in interface science ; vol. 24. Amsterdam: Elsevier, 2010.
- El-Sherik, A. M. and U. Erb. "Synthesis of Bulk Nanocrystalline Nickel by Pulsed Electrodeposition." *Journal of Materials Science* 30, no. 22 (1995): 5743-5749.
- El-Sherik, A. M., U. Erb, G. Palumbo and K. T. Aust. "Deviations from Hall-Petch Behaviour in as-Prepared Nanocrystalline Nickel." *Scripta Metallurgica et Materiala* 27, no. 9 (1992): 1185-1188.
- Erb, U. "Size Effects in Electroformed Nanomaterials." *Key Engineering Materials* 444, (2010): 163-188.
- Erb, U., G. Palumbo and J.L. McCrea. "The Processing of Bulk Nanocrystalline Metals and Alloys by Electrodeposition." In *Nanostructured Metals and Alloys : Processing, Microstructure, Mechanical Properties and Applications*, edited by S.H. Whang, 119-151. Oxford, UK: Woodhead Publishing, 2011.
- Fransaer, J., J. P. Celis and J. R. Roos. "Analysis of the Electrolytic Codeposition of Non-Brownian Particles with Metals." *Journal of the Electrochemical Society* 139, no. 2 (1992): 413-425.
- Fluon. "Typical Properties of Fluon® PTFE." (2007) Accessed March 3, 2014 [Online]: <http://www.fluon.jp/fluon/english/products/ptfe/properties.shtml>
- Ger, M. D. and B. J. Hwang. "Effect of Surfactants on Codeposition of Ptfе Particles with Electroless Ni-P Coating." *Materials Chemistry and Physics* 76, no. 1 (2002): 38-45.
- Guglielmi, N. "Kinetics of the Deposition of Inert Particles from Electrolytic Baths." *Journal of the Electrochemical Society* 119, no. 8 (1972): 1009-1012.
- Guo, C., Y. Zuo, X. H. Zhao, J. M. Zhao and J. P. Xiong. "Effects of Surfactants on Electrodeposition of Nickel-Carbon Nanotubes Composite Coatings." *Surface & Coatings Technology* 202, no. 14 (2008): 3385-3390.
- Gyawali, G., R. Adhikari, H.S. Kim, H-B. Cho and S.W. Lee. "Effect of H-Bn Nanosheets Codeposition on Electrochemical Corrosion Behavior of Electrodeposited Nickel Composite Coatings." *Ecs Electrochemistry Letters* 2, no. 3 (2013): C7-C10.

- Gül, H., F. Kılıç, M. Uysal, S. Aslan, A. Alp and H. Akbulut. "Effect of Particle Concentration on the Structure and Tribological Properties of Submicron Particle Sic Reinforced Ni Metal Matrix Composite (Mmc) Coatings Produced by Electrodeposition." *Applied Surface Science* 258, no. 10 (2012): 4260-4267.
- Haasz, T. R., K. T. Aust, G. Palumbo, A. M. El-Sherik and U. Erb. "Intercrystalline Density of Nanocrystalline Nickel." *Scripta Metallurgica et Materialia* 32, no. 3 (1995): 423-426.
- Hamid, Z. A. and A. M. A. Omar. "The Relation between Anionic/Non-Ionic Surfactant and Electrodeposition of Nickel-Polytetrafluoro Ethylene Polymer Composite." *Anti-Corrosion Methods and Materials* 46, no. 3 (1999): 212-216.
- Hang, T., A. Hu, H. Ling, M. Li and D. Mao. "Super-Hydrophobic Nickel Films with Micro-Nano Hierarchical Structure Prepared by Electrodeposition." *Applied Surface Science* 256, no. 8 (2010): 2400-2404.
- Helle, K. and F. Walsh. "Electrodeposition of Composite Layers Consisting of Inert Inclusions in a Metal Matrix." *Transactions of the Institute of Metal Finishing* 75, (1997): 53-58.
- Hsiao, C.K. "A Surface Tension Study on Conventional Polycrystalline and Nanocrystalline Nickel." University of Toronto, 2002.
- Hu, X., C. Dai, J. Li and D. Wang. "Zeta Potential & Codeposition of Ptfе Particles Suspended in Electroless Nickel Solution." *Plating and Surface Finishing* 84, no. 3 (1997): 51-53.
- Huang, S., Y. Hu and W. Pan. "Relationship between the Structure and Hydrophobic Performance of Ni-TiO₂ Nanocomposite Coatings by Electrodeposition." *Surface & Coatings Technology* 205, no. 13-14 (2011): 3872-3876.
- Huang, Y. S., X. T. Zeng, I. Annergren and E. Liu. "Development of Electroless Nip-Ptfe-Sic Composite Coating." *Surface & Coatings Technology* 167, no. 2-3 (2003): 207-211.
- Ibe, T., H. Kiyokawa, Y. B. Chong, S. Yonezawa and M. Takashima. "Electrodeposition and Surface Properties of Nickel-Ptfe Composite Film." *Materials Science Research International* 4, no. 3 (1998): 148-152.
- Jung, Y.C. and B. Bhushan. "Contact Angle, Adhesion and Friction Properties of Micro- and Nanopatterned Polymers for Superhydrophobicity." *Nanotechnology* 17, no. 19 (2006): 4970-4980.
- Kear B.H, R.W. Siegel (1992) Preface. *Nanostructured Materials* 1:iii

- Kilic, F., H. Gul, S. Aslan, A. Alp and H. Akbulut. "Effect of Ctab Concentration in the Electrolyte on the Tribological Properties of Nanoparticle Sic Reinforced Ni Metal Matrix Composite (Mmc) Coatings Produced by Electrodeposition." *Colloids and Surfaces a-Physicochemical and Engineering Aspects* 419, (2013): 53-60.
- Kim, H. S. "On the Rule of Mixtures for the Hardness of Particle Reinforced Composites." *Materials Science and Engineering a-Structural Materials Properties Microstructure and Processing* 289, no. 1-2 (2000): 30-33.
- Klingler, A. Master`s Thesis *Technical University of Kaiserslautern* (2014) To be published.
- Mafi, I. R. and C. Dehghanian. "Comparison of the Coating Properties and Corrosion Rates in Electroless Ni-P/Ptfe Composites Prepared by Different Types of Surfactants." *Applied Surface Science* 257, no. 20 (2011): 8653-8658.
- McHale, G., N. J. Shirtcliffe and M. I. Newton. "Contact-Angle Hysteresis on Super-Hydrophobic Surfaces." *Langmuir* 20, no. 23 (2004): 10146-10149.
- Napper, D. H. and A. Netschey. "Studies of the Steric Stabilization of Colloidal Particles." *Journal of Colloid and Interface Science* 37, no. 3 (1971): 528-535.
- Nosonovsky, M. and B. Bhushan. "Superhydrophobic Surfaces and Emerging Applications: Non-Adhesion, Energy, Green Engineering." *Current Opinion in Colloid & Interface Science* 14, no. 4 (2009): 270-280.
- Omar, A. M. A. and A. El Morsi. "Development of a Nickel-Polymer Composite by Using Friendly Environmental Polymeric Surfactant." *Materials Science and Engineering a-Structural Materials Properties Microstructure and Processing* 521-22, (2009): 397-400.
- Palumbo, G., S. J. Thorpe and K. T. Aust. "On the Contribution of Triple Junctions to the Structure and Properties of Nanocrystalline Materials." *Scripta Metallurgica et Materiala* 24, no. 7 (1990): 1347-1350.
- Pena-Munoz, E., P. Bercot, A. Grosjean, M. Rezrazi and J. Pagetti. "Electrolytic and Electroless Coatings of Ni-Ptfe Composites - Study of Some Characteristics." *Surface & Coatings Technology* 107, no. 2-3 (1998): 85-93.
- Priest, C., T.W.J. Albrecht, R. Sedev and J. Ralston. "Asymmetric Wetting Hysteresis on Hydrophobic Microstructured Surfaces." *Langmuir* 25, no. 10 (2009): 5655-5660.

- Quere, D., A. Lafuma and J. Bico. "Slippy and Sticky Microtextured Solids." *Nanotechnology* 14, no. 10 (2003): 1109-1112.
- Rajarao, N.S.S.V., A. Phanendralal Varma, V. Brahmajirao and A.V. Sarma. "Experimental Technique Developed to Measure Dielectric Constants of Aqueous Sulphates, Chloride and Nitrates at 298k Part I " *International Journal of Engineering Science and Technology* 5, no. 3 (2013): 691-698.
- Ramesh Babu, G.N.K and S. Mohan. "Electrodeposition of Nickel-Polytetrafluoroethylene (Ptfe) Polymer Composites." *Plating & Surface Finishing* 82, no. 4 (1995): 86-88.
- Rashidi, A. M. and A. Amadeh. "Effect of Electroplating Parameters on Microstructure of Nanocrystalline Nickel Coatings." *Journal of Materials Science & Technology* 26, no. 1 (2010): 82-86.
- Rezrazi, M., M. L. Doche, P. Berçot and J. Y. Hihn. "Au–Ptfe Composite Coatings Elaborated under Ultrasonic Stirring." *Surface and Coatings Technology* 192, no. 1 (2005): 124-130.
- Rossi, S., F. Chini, G. Straffelini, P. L. Bonora, R. Moschini and A. Stampali. "Corrosion Protection Properties of Electroless Nickel/Ptfe, Phosphate/Mos2 and Bronze/Ptfe Coatings Applied to Improve the Wear Resistance of Carbon Steel." *Surface & Coatings Technology* 173, no. 2-3 (2003): 235-242.
- Rudnik, E., L. Burzynska, L. Dolasinski and M. Misiak. "Electrodeposition of Nickel/Sic Composites in the Presence of Cetyltrimethylammonium Bromide." *Applied Surface Science* 256, no. 24 (2010): 7414-7420.
- Schlesinger, M. and M. Paunovic. *Modern Electroplating*. 5th ed. The electrochemical society series ; 52. Hoboken, NJ: Wiley, 2010.
- Shirtcliffe, N. J., S. Aqil, C. Evans, G. McHale, M. I. Newton, C. C. Perry and P. Roach. "The Use of High Aspect Ratio Photoresist (Su-8) for Super-Hydrophobic Pattern Prototyping." *Journal of Micromechanics and Microengineering* 14, no. 10 (2004): 1384-1389.
- Shrestha, N. K., G. Kobayashi and T. Saji. "Electrodeposition of Hydrophobic Nickel Composite Containing Surface-Modified Sio2 Particles under the Influence of a Surfactant with an Azobenzene Moiety." *Chemistry Letters* 33, no. 8 (2004): 984-985.

- Simunkova, H., P. Pessenda-Garcia, J. Wosik, P. Angerer, H. Kronberger and G.E. Nauer. "The Fundamentals of Nano- and Submicro-Scaled Ceramic Particles Incorporation into Electrodeposited Nickel Layers: Zeta Potential Measurements." *Surface & Coatings Technology* 203, no. 13 (2009): 1806-1814.
- Sun, C., L. Ge and Z. Gu. "Fabrication of Super-Hydrophobic Film with Dual-Size Roughness by Silica Sphere Assembly." *Thin Solid Films* 515, no. 11 (2007): 4686-4690.
- Victor, J.J. "Biology Inspired Nano-materials: Superhydrophobic Surfaces." Ph.D. Thesis. *University of Toronto* (2012)
- Victor, J. J., D. Facchini and U. Erb. "A Low-Cost Method to Produce Superhydrophobic Polymer Surfaces." *Journal of Materials Science* 47, no. 8 (2012): 3690-3697.
- Wang, F., S. Arai and M. Endo. "Electrochemical Preparation and Characterization of Nickel/Ultra-Dispersed Ptfе Composite Films from Aqueous Solution." *Materials Transactions* 45, no. 4 (2004): 1311-1316.
- Wang, J. F., J. T. Tian, X. Z. Liu, Y. S. Yin and X. Wang. "Effect of Polytetrafluoroethylene Content on Electrochemical Anticorrosion Behaviors of Electroless Deposited Ni-P and Ni-P-Polytetrafluoroethylene Coatings in Seawater." *Thin Solid Films* 519, no. 18 (2011): 5905-5911.
- Willson, K.S. and J.A. Rogers *Technical Proceedings American Electroplaters Society* 51, (1964): 92
- Wilson, S. J. and M. C. Hutley. "The Optical-Properties of Moth Eye Antireflection Surfaces." *Optica Acta* 29, no. 7 (1982): 993-1009.
- Wong, T-S., S.H. Kang, S.K.Y. Tang, E.J. Smythe, B.D. Hatton, A. Grinthal and J. Aizenberg. "Bioinspired Self-Repairing Slippery Surfaces with Pressure-Stable Omniphobicity." *Nature* 477, no. 7365 (2011): 443-447.
- Wu, Y. T., C. Zhong, M. F. He, L. Liu and W. B. Hu. "Antifriction and Wear Characteristics of Electrolessly-Deposited Ni-P with Ptfе Composites." *Tribology Letters* 42, no. 2 (2011): 161-168.
- Xiu, Y., L. Zhu, D.W. Hess and C.P. Wong. "Hierarchical Silicon Etched Structures for Controlled Hydrophobicity/Superhydrophobicity." *Nano Letters* 7, no. 11 (2007): 3388-3393.

Xu, X., L. Zhu, W. Li and H. Liu. "A Variable Hydrophobic Surface Improves Corrosion Resistance of Electroplating Copper Coating." *Applied Surface Science* 257, no. 13 (2011): 5524-5528.

Xu, X., L. Zhu, W. Li and H. Liu. "Microstructure and Deposition Mechanism of Electrodeposited Cu/Liquid Microcapsule Composite." *Transactions of Nonferrous Metals Society of China* 21, no. 10 (2011): 2210-2215.

Zimmerman, A. F., G. Palumbo, K. T. Aust and U. Erb. "Mechanical Properties of Nickel Silicon Carbide Nanocomposites." *Materials Science and Engineering: A* 328, no. 1-2 (2002): 137-146.

Appendix 1 – Determining Coating Composition

Figure A1.1 shows an example of how image analysis was performed to determine amount of PTFE particles in a deposit, using ImageJ software. The threshold function was used to separate PTFE from nickel based on the contrast. After thresholding the image, the automatic function ‘Analyze Particles’ was used. The minimum particle size was set to 100 nm, as no particle below this size is seen in any SEM images, to discount any small dark pixels that were not PTFE particles. Since only the surface is being analyzed through this method, an area fraction of the surface is measured. It is assumed a constant distribution throughout the coating which is observed in cross section images. Samples were cleaned in ethanol using a ultrasonic cleaner to ensure particles on the surface are embedded in the coating and not simply loosely attached. The thresholding shown in Figure A1.1 B is done by zooming in on areas with distinct particles and adjusting the threshold so all PTFE is represented by the red colour.

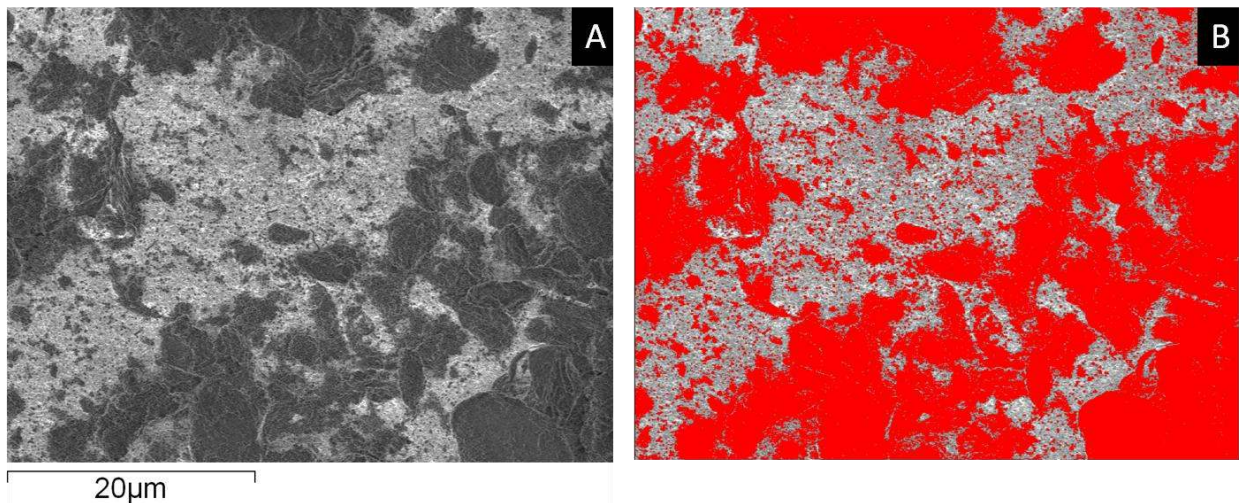


Figure A1.1: Example of Ni-PTFE sample analyzed using image analysis showing an area fraction of 61.2% PTFE.

Figure A1.2 shows backscattered image at X500 magnification of the same sample shown in Figure A1.1 with the results of EDX scan. The weight percentage of nickel and fluorine are listed. A sample calculation for converting wt% F to vol% PTFE is shown.

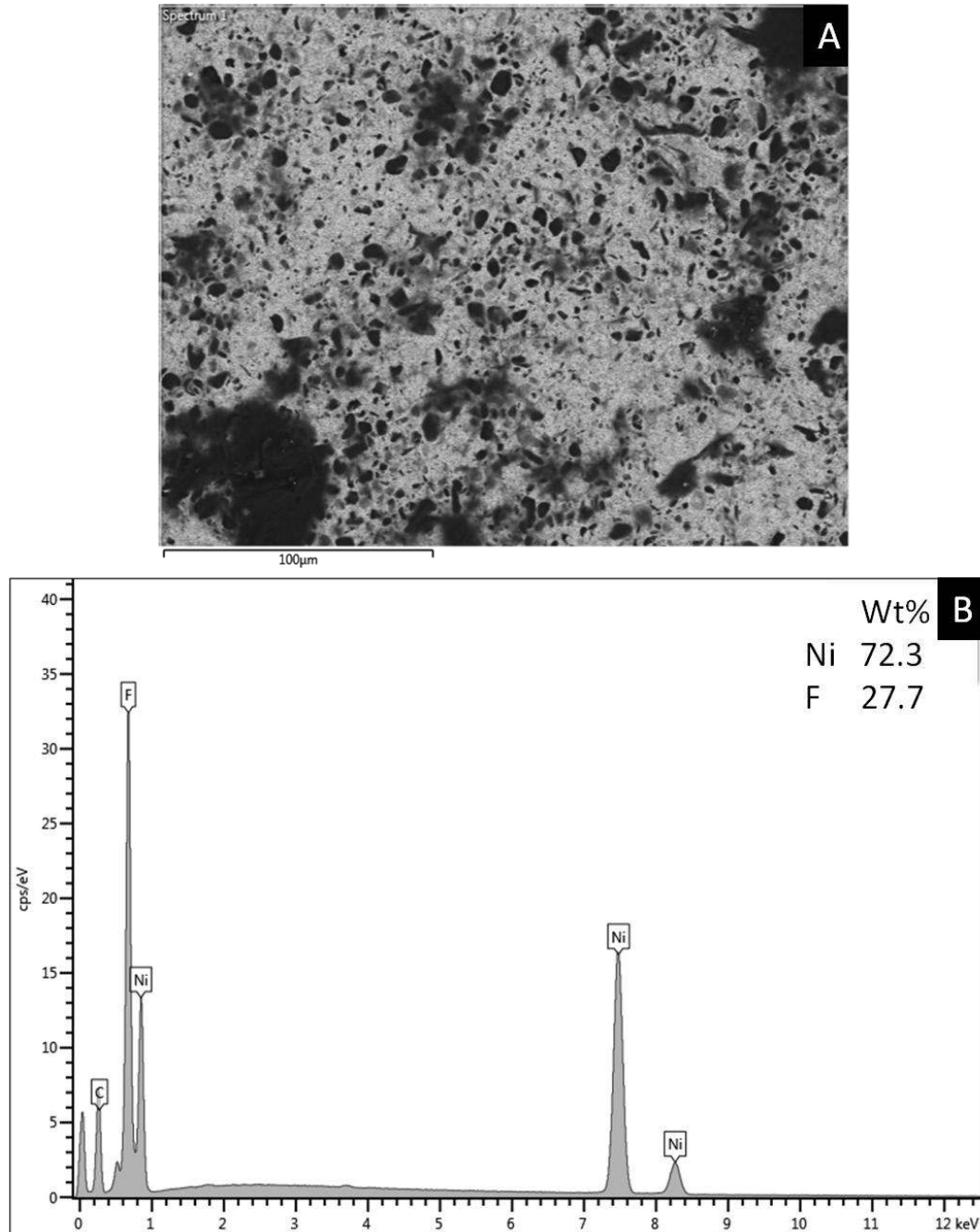


Figure A1.2: EDX spectrum obtained over area shown in image A taken at x500 mag.

To determine vol% PTFE, the first step is to convert wt% F to wt% PTFE, using the chemical formula of PTFE, CF_2 . Since the measured value is for all of the fluorine atoms, the ratio of M_{F_2} to M_{CF_2} can be used as a conversion factor from the detected mass of fluorine to the mass of PTFE this represents.

$$\frac{M_{F_2}}{M_{CF_2}} = \frac{37.996}{50.007} = 0.7598 \quad (A1-1)$$

$$wt\% PTFE = \frac{wt\% F}{0.7598} = \frac{27.7}{0.7598} = 36.46\% \quad (A1-2)$$

The vol% PTFE can now be easily calculated knowing the density of nickel as 8.9 g/cm^3 and the density of PTFE is 2.2 g/cm^3 using equation (A1-3).

$$\begin{aligned} vol\% PTFE &= \frac{\frac{wt\% PTFE}{\rho_{PTFE}}}{\frac{wt\% PTFE}{\rho_{PTFE}} + \frac{(1 - wt\% PTFE)}{\rho_{Ni}}} = \frac{\frac{0.3646}{2.2}}{\frac{0.3646}{2.2} + \frac{0.6354}{8.9}} \quad (A1-3) \\ &= 69.9 \text{ vol}\% PTFE \end{aligned}$$

Appendix 2 – Additional SEM Images

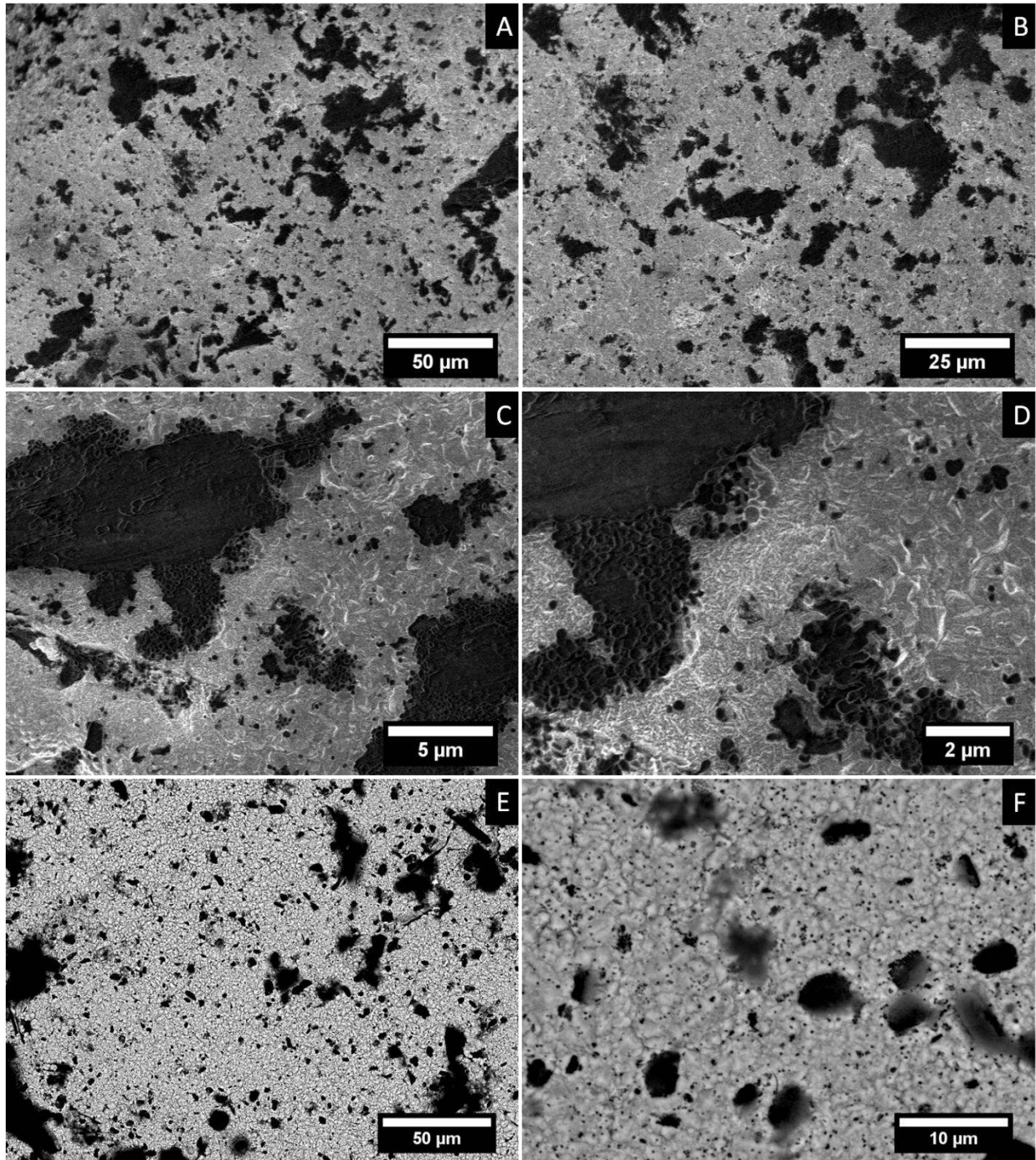


Figure A2.1: SEM images for Ni-PTFE sample with 40 vol% PTFE. A-D are secondary electron images and E-F are backscattered electron images A) x500 B) x1,000 C) x5,000 D) x10,000 E)x500 F)x2,500

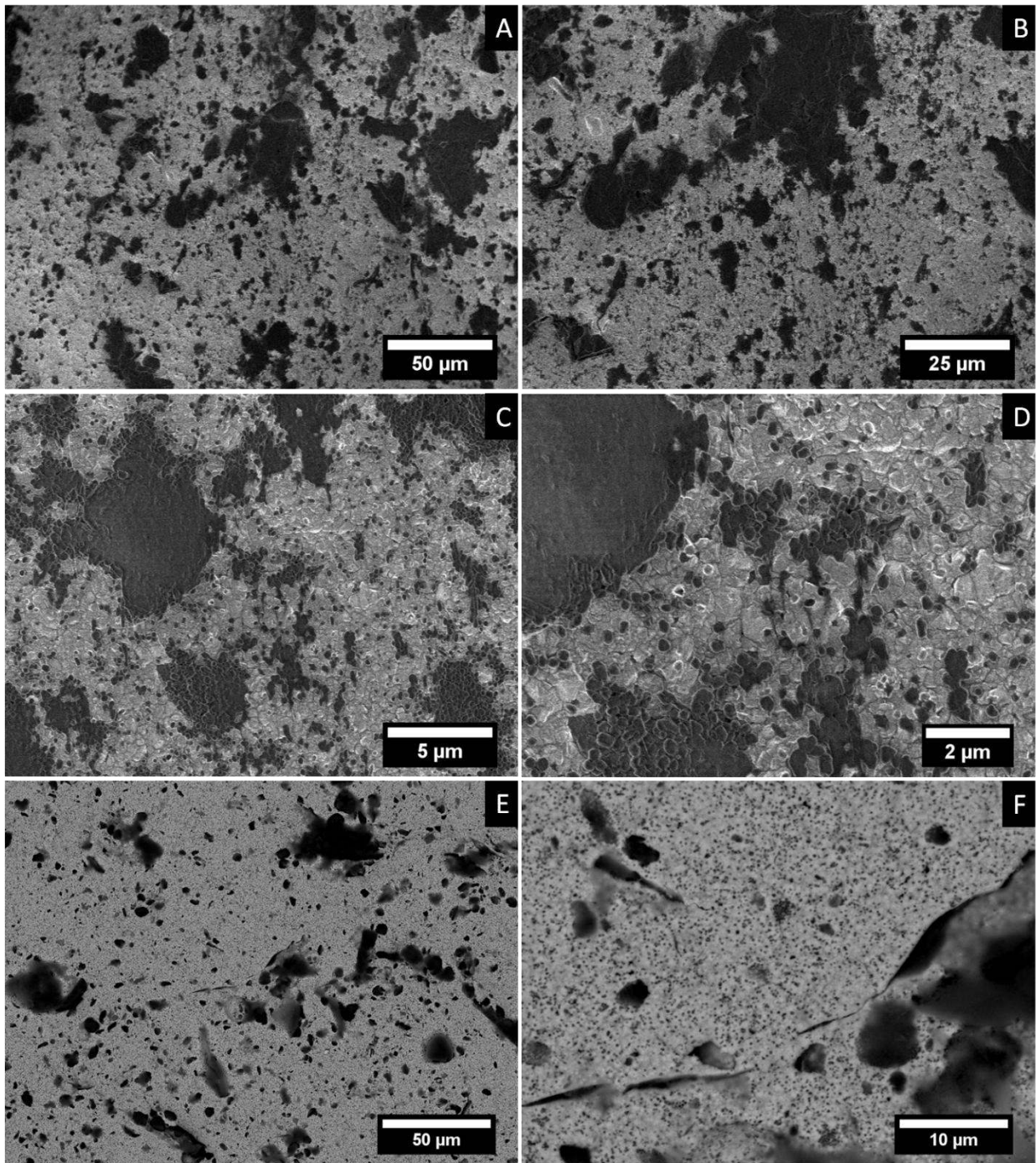


Figure A2.2: SEM images for Ni-PTFE sample with 45 vol% PTFE. A-D are secondary electron images and E-F are backscattered electron images A) x500 B) x1,000 C) x5,000 D) x10,000 E)x500 F)x2,500

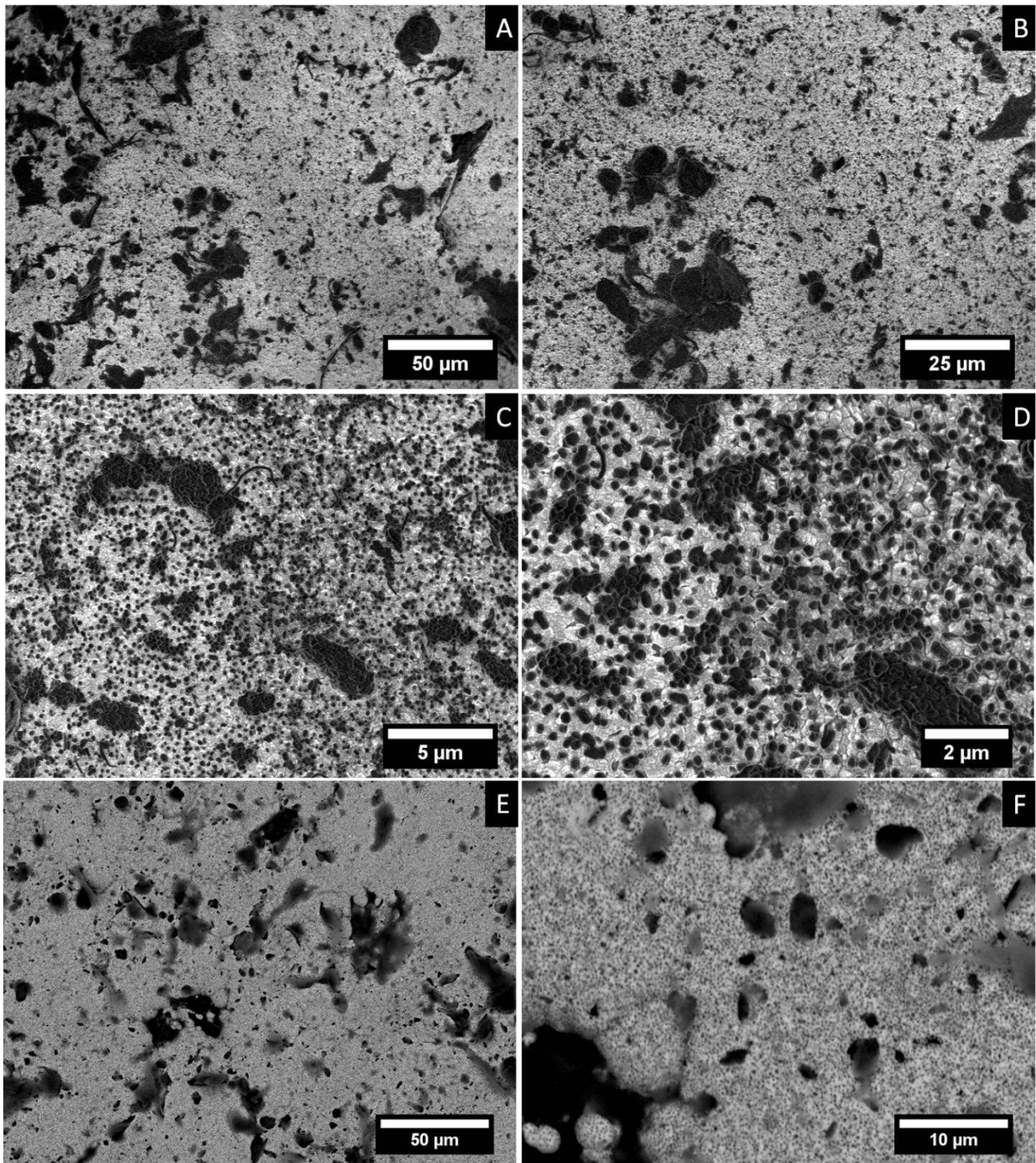


Figure A2.3: SEM images for Ni-PTFE sample with 58 vol% PTFE. A-D are secondary electron images and E-F are backscattered electron images A) x500 B) x1,000 C) x5,000 D) x10,000 E)x500 F)x2,500

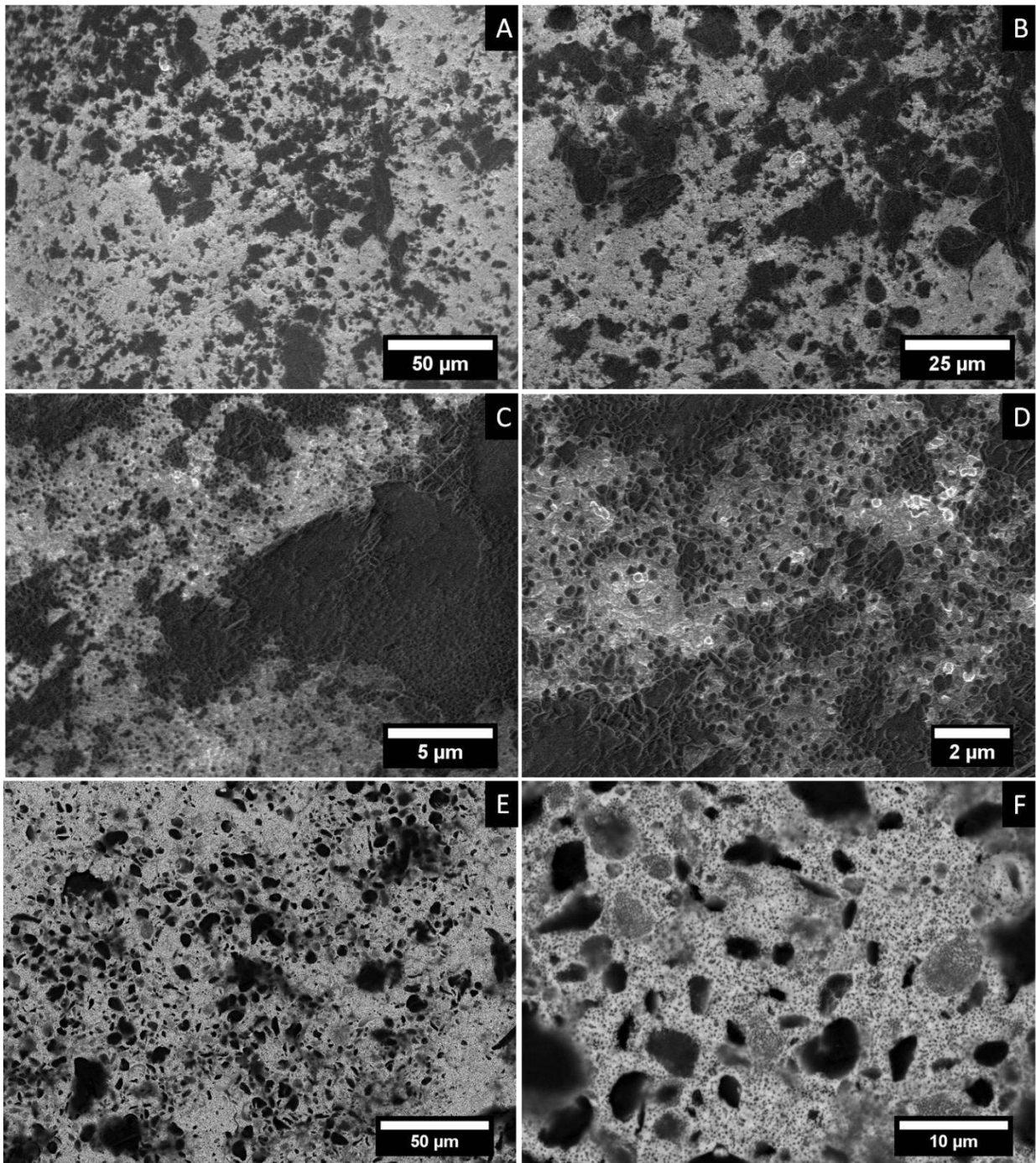


Figure A2.4: SEM images for Ni-PTFE sample with 69 vol% PTFE. A-D are secondary electron images and E-F are backscattered electron images A) x500 B) x1,000 C) x5,000 D) x10,000 E)x500 F)x2,500

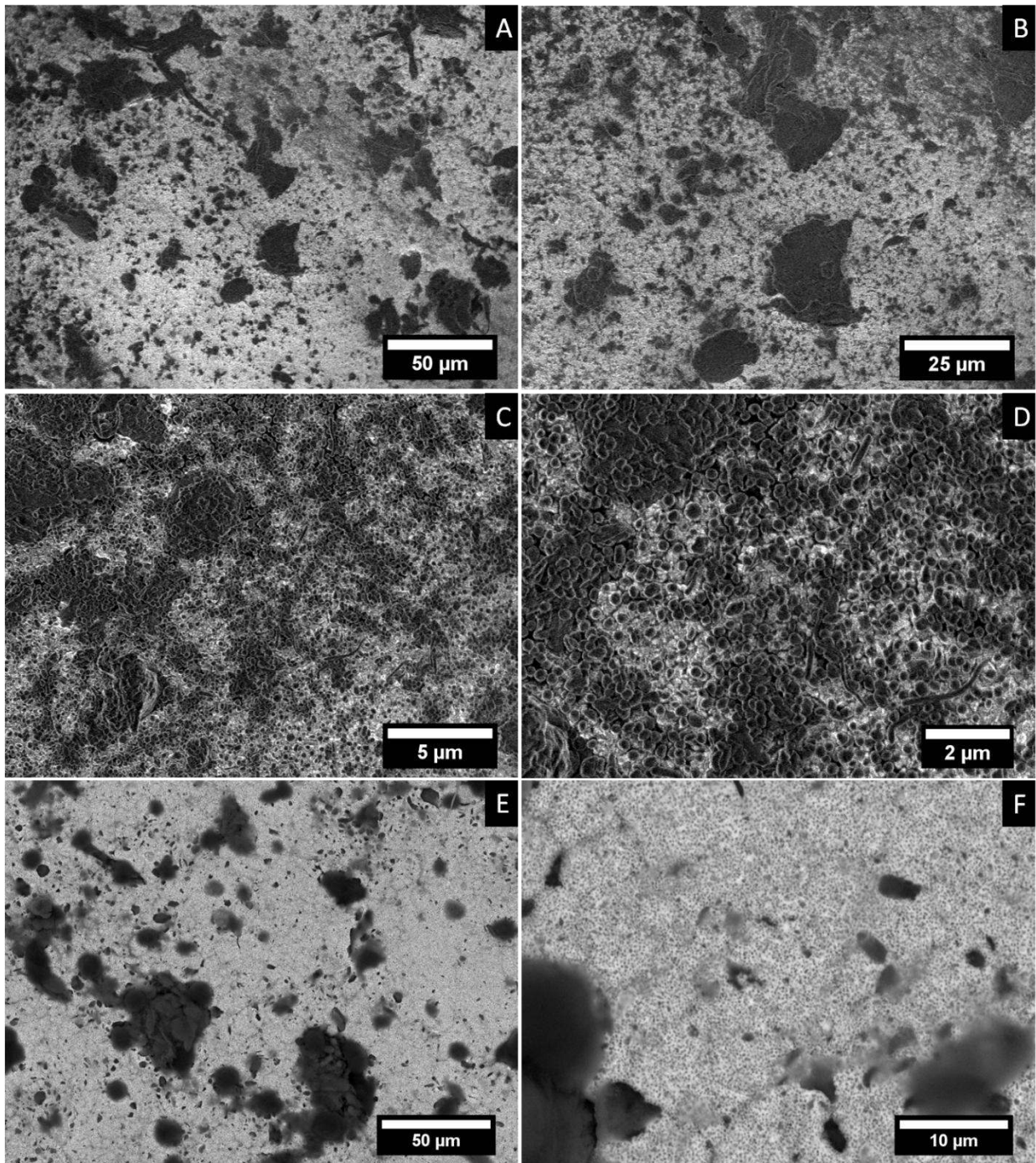


Figure A2.5: SEM images for Ni-PTFE sample with 58 vol% PTFE. A-D are secondary electron images and E-F are backscattered electron images A) x500 B) x1,000 C) x5,000 D) x10,000 E)x500 F)x2,500

The following SEM images show fracture surfaces of Ni-PTFE coatings that have undergone three point bending testing. Bending tests and images were done by Andreas Klingler [Klingler 2014]. Samples shown were produced using electrodeposition under the same conditions described in Table 3.2. Fracture surfaces show even distribution of PTFE particles throughout thickness of coatings.

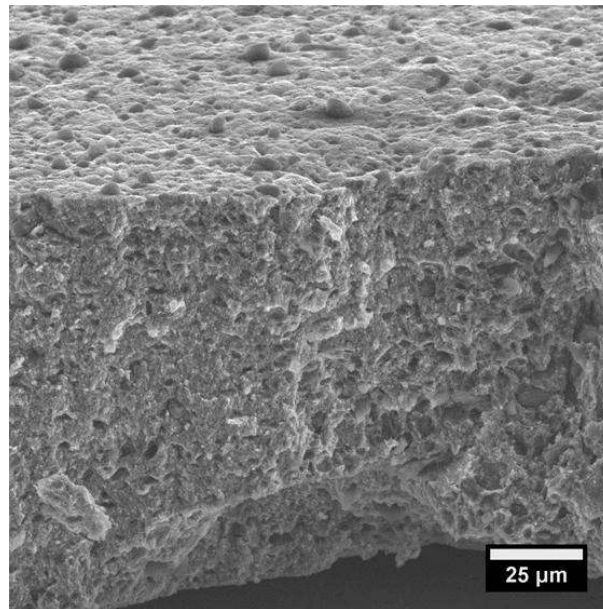


Figure A2.6: x500 magnification image of fracture surface of a Ni-PTFE sample containing approximately 70 vol% PTFE [Klingler 2014].

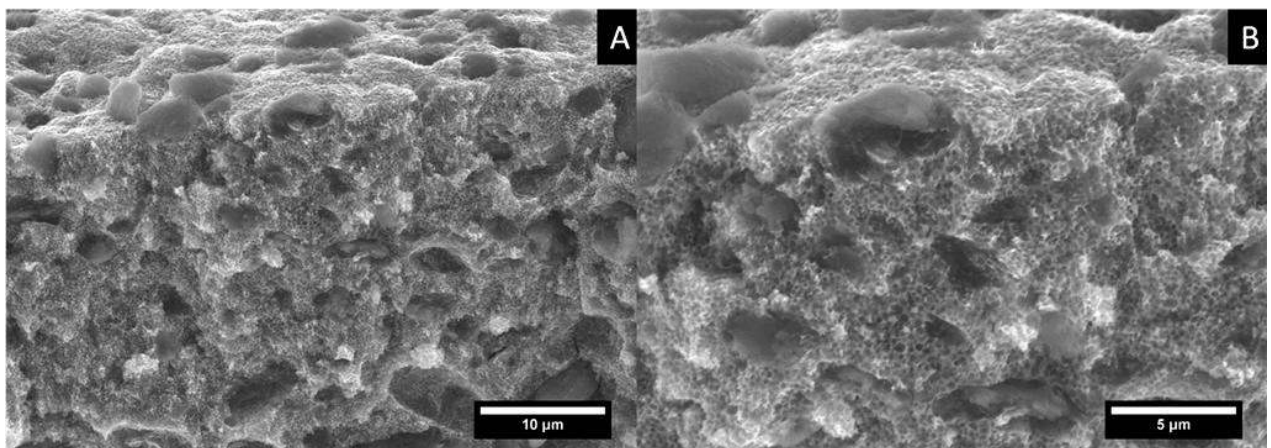


Figure A2.7: Fracture surface of a Ni-PTFE sample containing approximately 70 vol% PTFE A) x2,500 B) x5,000 magnification [Klingler 2014].

Appendix 3 – Additional Information on Acoustic Particle Size Measurements

Figure 3.2 shows the sample chamber for particle size measurements. In this chamber, two transducers are used. At one side ultrasonic waves are emitted at a certain frequency. These waves then travel through the colloidal solution and the intensity of the waves is measured at the other transducer, with the distance between the transducers known. The intensity of the emitted ultrasonic waves will decline exponentially as a function of the distance travelled through the solution. The amount of reduction in intensity as the wave passes through the sample is related to the attenuation coefficient, α , of the solution which is expressed by the following equation [Duhkin et al. 2005],

$$\alpha = \frac{1}{fL} \log \frac{I_{in}}{I_{out}} \quad (\text{A3-1})$$

where I_{in} and I_{out} are the emitted and measured intensities, f is the frequency of sound wave, and L is the gap length (distance between the transducers). To obtain the attenuation coefficient using the DT-1200 system, intensity of the ultrasound is recorded for 18 frequencies, between 1-100 MHz, at 21 different gap lengths between 0.15 and 20 mm.

The attenuation of the ultrasonic wave in a colloidal solution can be expressed as a superposition of several energy loss mechanisms. The five significant mechanisms that are taken into account are viscous losses, thermal losses, structural losses, scattering losses, and intrinsic losses. The total attenuation, α_T , of the system can thus be written as,

$$\alpha_T = \alpha_{vis} + \alpha_{th} + \alpha_{sc} + \alpha_{int} + \alpha_{st} \quad (\text{A3-2})$$

The type and size of particles being measured will determine which of the five attenuation mechanisms most significant in a specific system. A brief description of each mechanism is given below [Duhkin and Goetz 2010].

- 1) Viscous losses, α_{vis} , occur when particles move relative to the liquid media. When ultrasonic waves are emitted into the solution, pressure waves are generated causing motion of both the liquid and solid particles. The motion will not be the same for the two due to differences in the density. The particle motion relative to the liquid generates shear waves, which causes a loss in acoustic energy due to shear friction. Viscous losses are the dominant energy loss mechanism for small, rigid particles with sizes under 3 μm .
- 2) Thermal losses, α_{th} , are related to temperature gradients that can be generated near particle surfaces. Temperature gradients are caused by changes in pressure as a result of the sound wave passing through. This effect is only significant in soft particles such as emulsions or latex droplets.
- 3) Scattering losses, α_{sc} , occur as particles may redirect part of the acoustic sound energy preventing it from ever reaching the receiving transducer. This mechanism only has a significant contribution for larger particles with diameter greater than 3 μm .
- 4) Intrinsic losses, α_{int} , describe the loss of acoustic energy as a sound wave travels through the solution. Acoustic energy is lost during the interaction of liquid media and solid particles.

Intrinsic losses have significant contribution when the other attenuation mechanisms are low, such as small particle size or when the volume fraction is low.

- 5) Structural losses, α_{st} , only occur when particles are joined together in a network. In this situation interparticle bonds may oscillate which will cause a loss of acoustic energy.

For the solution of the PTFE particles used in this study in a water/CTAB solution, the attenuation mechanisms that contribute significantly are viscous losses, scattering losses and intrinsic losses. PTFE particles are considered solid, rigid particles and the bimodal distribution observed suggests viscous losses as well as scattering losses will both contribute to the overall attenuation. This reduces equation (A3-3) to,

$$\alpha_T = \alpha_{vis} + \alpha_{sc} + \alpha_{int} \quad (A3-3)$$

The measured attenuation can be used to determine a particle size distribution by using a coupled-phase model. The emitted ultrasonic waves apply a force to the solution due to the pressure gradient of the sound wave. A coupled wave equation can be used to describe the balance of forces for the particles and the liquid medium based on Newton's Second Law. For a colloidal dispersion containing a distribution of N number of particle sizes, a system of $N+1$ equations (N equations for particles plus 1 for the liquid) can be applied with the volume fraction of each particle size unknown. The wave equations incorporate the attenuation coefficient which is directly related to the particle size based on the different attenuation mechanisms listed above. Each particle size will have a peak attenuation at a different frequency. Iterative calculations are done on the equations to produce the volume fraction of each particle size that will result in the

weighted average of the N attenuations from these equations to closely fit the measured attenuation [Dukhin and Goetz 2010].

Appendix 4 – Additional Information on Zeta Potential Measurements

To determine the zeta potential of a colloidal solution, the DT-1200 by Dispersion Technology, Inc. uses an electroacoustic technique. The main components of the probe are a piezoelectric transducer, gold electrode and a stainless steel shell. The piezoelectric transducer is used to convert a radio frequency pulse into acoustic energy. The acoustic energy transmitted into the colloidal solution will cause an oscillating motion of ions relative to the particles. This causes an induced oscillating dipole moment which will generate an electric field. The electric field will cause a current to flow between the gold electrode and stainless steel shell. This current is known as the colloid vibration current, CVI, and this is what the probe measures which can be used to determine the zeta potential of the particles [Dukhin and Goetz 2010].

To determine the zeta potential from CVI measurements there are several variables needed. These include the particle size, the volume fraction of particles, the dielectric permittivity of the liquid medium, as well as the velocity of the liquid relative to the particle. The particle size of the solution needs to therefore be obtained before zeta potential measurements are made. The volume fractions of particles as well as dielectric permittivity of the solution are inputted by the user. Dielectric permittivity of the solutions was approximated using measured values from literature for nickel sulfate and nickel chloride solutions at various concentrations [Rajarao 2013]. Approximate dielectric permittivity values used are shown in Table A4.1. The velocity of the liquid relative to the particle is a function of the pressure gradient of the sound wave as well as the densities of the particle and solution. Full details of the

equations used to determine zeta potential from CVI measurements are presented in reference [Dukhin and Goetz 2010].

Table A4.1: Dielectric permittivity values used to calculate zeta potential

Bath Composition	Dielectric Permittivity *
0 M (CTAB only)	78.85 (Water)
0.01M (2.1 g/L)	78.85
0.1M (21 g/L)	75.34
1M (210 g/L)	56.15
1.85M (390 g/L) Watt's Bath	47.15

*Increasing ionic concentration decreases the dielectric permittivity. Total decrease in permittivity is estimated as the sum of the decrease caused by NiCl_2 and NiSO_4 . Values taken from experimental curves produced by [Rajarao 2013].

Appendix 5 – Sample Calculations for Intensity of XRD Peaks for Nickel with Random Orientation

To determine the orientation indices for various X-ray diffraction lines of the nickel matrix, the expected intensities of a randomly oriented nickel sample must be determined. The first step in this process is to calculate the Bragg angle for the peaks of interest. For this work the first five peaks for the FCC nickel are examined. The structure factor for FCC materials is $F=4f$ for all even or all odd Miller indices, hkl , and $F=0$ for mixed Miller indices. Based on increasing values of $h^2 + k^2 + l^2$, the first five peaks for FCC metals are {111}, {200}, {220}, {311}, and {222}.

The Bragg angle, θ_B , for each peak is determined by using Bragg's equation,

$$n\lambda = 2d_{hkl}\sin\theta_B \quad (\text{A5-1})$$

where λ is the wavelength of the X-rays, which is 0.179 nm for the Co-K α source that is used in the Rigaku MiniFlex diffractometer used in this study. d_{hkl} is the spacing between planes which is calculated using the following equation,

$$d_{hkl} = \frac{a}{\sqrt{h^2 + k^2 + l^2}} \quad (\text{A5-2})$$

where a is the lattice parameter of nickel, which is 0.35238 nm.

The intensity for the diffraction lines can be calculated using the following equation [Cullity and Stock 2001],

$$I = |F|^2 p \left(\frac{1 + \cos^2 2\theta_B}{\sin^2 \theta_B \cos \theta_B} \right) \quad (\text{A5-3})$$

where I is the relative integrated intensity in arbitrary units, F is the structure factor, p is the multiplicity factor and θ_B is the Bragg angle. The structure factor F is equal to $4f$ for the FCC nickel peaks, where f is the atomic scattering factor. The values for f and p were taken from tables in the text book Elements of X-Ray Diffraction [Cullity and Stock 2001]. Table A.1 summarizes the calculated values of intensity to be used in Equation (3-3).

Table A5.1: Summary of values used to calculate I in Equation (A5-3)

hkl	$h^2+k^2+l^2$	θ	2θ	f	F	p	I	Relative Intensity
{111}	3	26.1	52.2	19.09	76.35	8	369624.1	100
{200}	4	30.5	61.0	17.95	71.79	6	171941.8	46.5
{220}	8	45.9	91.8	14.88	59.54	12	118666.6	32.1
{311}	11	57.3	114.7	13.38	53.51	24	210998.9	57.1
{222}	12	61.6	123.1	12.96	51.85	8	75846.9	20.5

Appendix 6 – Further Surface Roughness Images

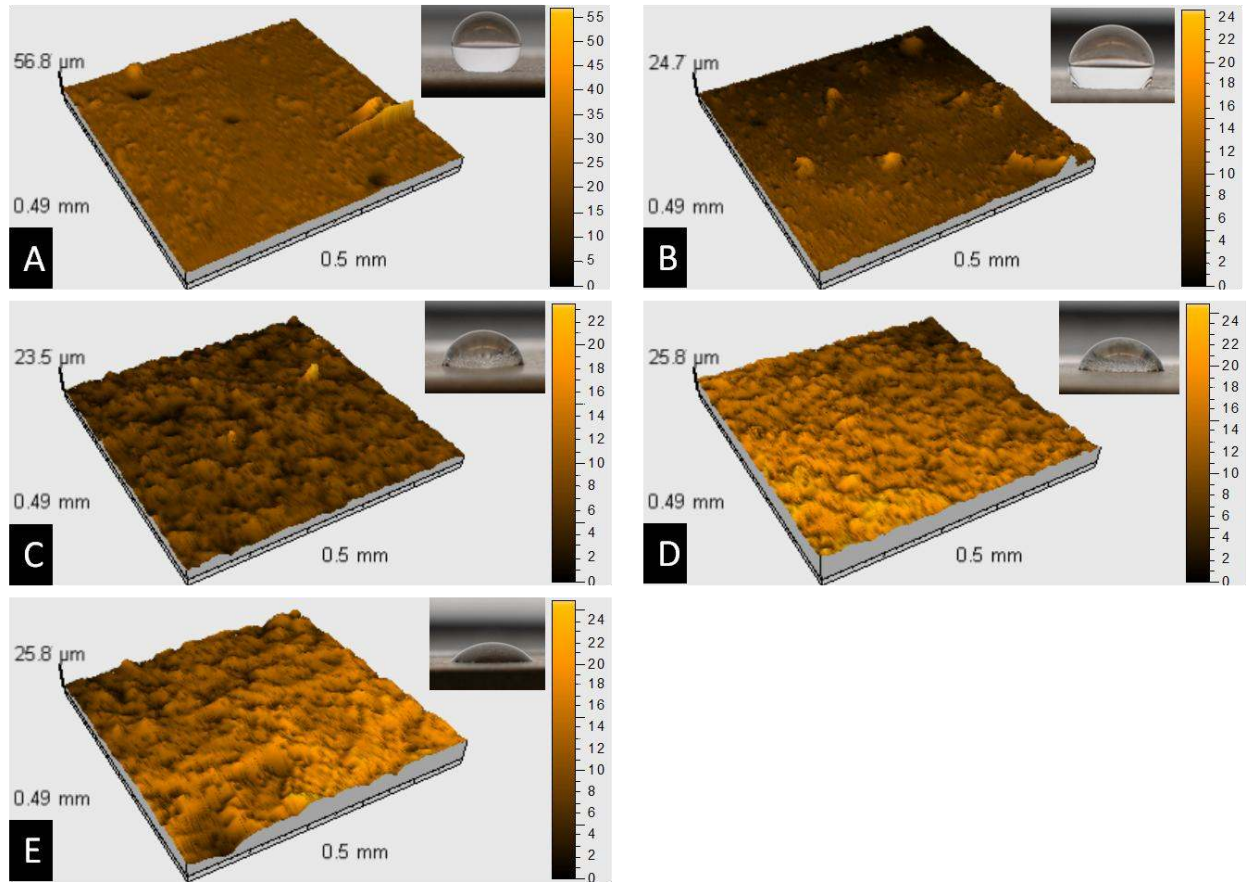


Figure A6.1: Results for 3D surface profilometry with varying saccharin concentration A) 0 g/L B) 0.1 g/L C) 1 g/L D) 3 g/L E) 5 g/L. Heights in micrometers.

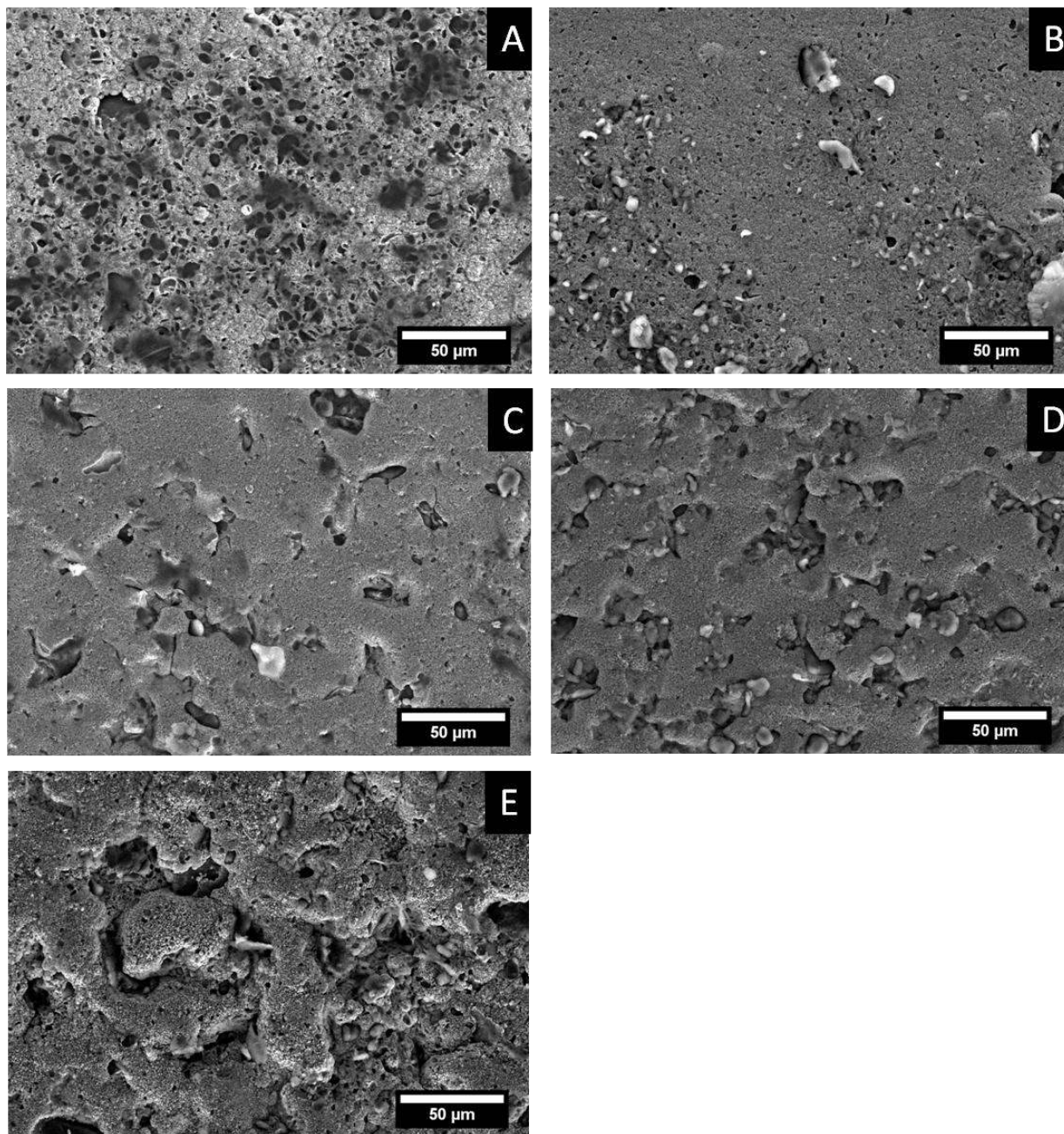


Figure A6.2: Secondary electron SEM images at x500 magnification of Ni-PTFE samples containing varying saccharin concentration A) 0 g/L B) 0.1 g/L C) 1 g/L D) 3 g/L E) 5 g/L.